Drainage of Thin Aqueous Films between Solid Surfaces Measured with the Colloidal Probe Technique

Dissertation

zur Erlangung des Grades “Doktor der Naturwissenschaften”
im Promotionsfach Physikalische Chemie

am Fachbereich Chemie, Pharmazie und Geowissenschaften
der Johannes Gutenberg–Universität in Mainz

vorgelegt von

Tiago dos Santos Rodrigues
geboren in Santos (Brasilien)

Mainz, 2012

Tag der mündlichen Prüfung: 29.05.2012
Dekan:
Erster Berichterstatter:
Zweiter Berichterstatter:

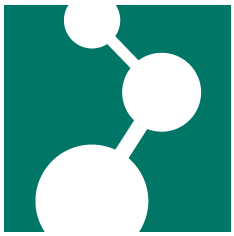

Die vorliegende Arbeit wurde
am Max-Planck-Institut für Polymerforschung in Mainz
unter der Anleitung von

und

im Zeitraum von März 2007 bis Juli 2010 angefertigt.

Dissertation der Universität Mainz (D77)

Contents

List of Figures

List of Tables

Abstract

Objects moving through a fluid experience resistance, or drag. Understanding the flow of liquids at the vicinity of solid surfaces is crucial to the development of technologies to reduce this drag. One way to infer the properties of the flow at the liquid-solid interface is to compare the experimental results to solutions of the Navier-Stokes equations assuming a different boundary condition (BC): Solutions using the slip BC predict lower drag than those assuming the no-slip BC. Flow measurement of Newtonian aqueous solutions over hydrophilic surfaces has gained attention in the last decade because of controversial results, some supporting the no-slip BC, others supporting the slip BC. The results were specially controversial because the slip BC is not expected to be valid for these systems. This work addresses this issue by performing drainage measurements between a sphere and a plane using the colloidal probe technique (CPT) to assess which BC is more suitable to describe flow of aqueous solutions over a hydrophilic SiO_2 surface. Discrepant results also were published within the CPT community. Despite the amount of published data, a systematic investigation to identify the source of contradiction is missing, and the results shown here are aimed to advance knowledge in this field. By the obtained results, the controversy over the applicability of the slip or no-slip BC on the drainage of aqueous solutions over hydrophilic substrates can be narrowed down to experimental parameters, especially the cantilever spring constant k. By using two different parameters based on k and other experimental variables, such as viscosity, the data obtained in this work and data reported in the literature could be separated in two different groups: one needing the no-slip BC to be explained, and another the slip BC. The observed residual slip lengths are function of instrumental parameters, and show a trend that is not compatible with the available physical justifications for slippage, suggesting that a stiffening process on the cantilever may be the cause for the residual slippage observed. It is then concluded that the no-slip BC is the more appropriate BC for the flow Newtonian, aqueous solutions over hydrophilic surfaces. The provided parameters can be used to avoid cases where the no-slip BC is not satisfied.

Introduction and Motivation

Objects moving through a fluid experience resistance [1]. This phenomenon, called drag, has attracted interest since times that date back to Aristotle, with the first reported experiments attributed to Galileo [2]. Investigation of drag forces has been motivated by a practical consequence: drag increases the energy needed for the object displacement if compared to an ideal situation in which dissipation is negligible. In a world with a constantly increasing need for energy, understanding the mechanisms behind drag forces is needed to boost the development of energy-saving technologies [3–5]. For example, the use of drag reducing additives may double the amount of petroleum transferred through pipelines [6].

Drag is related to the fluid properties, to the object shape and surface, and it varies also if the flow being studied is laminar or turbulent [7]. When dealing with viscous liquids, especially at small dimensions of the system, most of the drag comes from friction between the surface of the solid object and the fluid. The friction at a solid-liquid interface is significant for many practical applications, such as tribology [8], colloidal systems [9], or fabrication and operation of microfluidics devices [10].

In addition to practical applications, flows at small dimension bring the question about the length-scale limit of the assumption that a fluid can be approximated as a continuous medium, in spite of being formed by a group of discrete entities, such as atoms or molecules [11]. The theories assuming a fluid as a continuous medium were derived in the nineteenth century, being successfully used since then. Nevertheless, for many situations, the molecular nature of the fluid has to be considered. The continuous medium assumption is not valid, for example, for the flow of water through carbon nanotubes in the order of

few nanometers, in which a small number of molecules is confined inside the tubes [12]. Because of the fast pace of device miniaturization in the last years [10], it has become more important to find the length scale at which a continuous model has to be changed to a molecular one. Experimental evidence is crucial to answer this question.

Flow measurement at the vicinity of a surface has been a source of debate among scientists for a long time [2, 13]. The technological advances in measurement techniques keep changing the concept of vicinity, which is currently considerably closer to the surface than it was possible to reach a century ago. Despite this evolution, the direct observation of a single fluid molecule in contact with a solid surface is not yet possible; All techniques rely on models for interpreting the experimental data. Both experimental and computational studies have been extensively performed on the topic, but a satisfactory modeling has not yet been achieved [14–16]. The limits lie on the dimensions of studied systems: While the difficulty for simulations is that real liquids have a number of molecules too large for current computational capabilities, experimentalists have difficulties assessing flows at length scales with a small number of molecules.

The Navier-Stokes equations are used to describe flows in which the fluid can be considered as a continuous medium. Their solution requires boundary conditions to be set. For the case of a liquid flowing over a solid, usually two conditions are set: the liquid does not permeate the solid, and the relative fluid velocity at the solid-liquid interface is zero. The last one is called the no-slip boundary condition (BC), and there has been a controversy in the literature about its applicability at all scales. One alternative to the no-slip BC is to assume that the liquid in contact to the solid has a non-zero relative velocity, called the slip BC. In the study of liquid flowing over a solid, the BCs can give information about the liquid-solid interaction: If the use of the slip BC better describe the data, the drag is lower than expected for the case with the no-slip BC. The slip BC provides also an arbitrary variable, called the slip length, that is used to quantify how smaller than expected is the drag.

Although the discussion of which BC is more suitable to describe experimental results had

its start in the nineteenth century, a revival has been observed in the last decade arising from the increased research on microfluidics and the development of more precise measurement tools [14, 15]. The question has also a fundamental aspect, because the no-slip boundary condition has only empirical evidence supporting its usage. This motivates the search for validating the existent physical justifications.

It is widely accepted that the slip BC must be applied to explain the results of certain types of experiment, for example the flow of rarefied gases [17], the flow of certain polymer melts [18], and the motion of solid-liquid-gas contact lines [19]. The no-slip BC is well accepted for the flow of Newtonian liquids, in particular polar liquids flowing over hydrophilic surfaces [15], and there are results supporting that it is also valid down to the nanometric scale [14, 15, 20]. Notwithstanding, experiments performed with different experimental techniques were reported in the last years supporting the use of the slip BC for those systems [14].

The main justification for the validity of the no-slip BC is that the last layer of liquid is bonded to the solid because of the attractive surface forces between molecules of the liquid and of the solid surface [1]. Within this hypothesis, the appearance of slippage processes on the flow of polar, Newtonian liquids over hydrophilic surfaces were not expected. For that, the reports of slip on such systems attracted attention on the literature because of its potential consequences. On one side, slippage considerably complicates the flow predictions, since details of a particular solid-liquid interface have to be determined. On the other side, it opens a new perspective for drag reduction technologies, once the underlying mechanism is understood. In both cases, the existence of unexplained controversial results compromises the widespread technological application of the obtained conclusions, as observed in the nineteenth century [2, 13], motivating the search for the source of contradiction.

In this thesis, the question of which BC is more suitable for the drainage of Newtonian aqueous solutions between hydrophilic surfaces is addressed using the colloidal probe technique (CPT). As with other techniques, results obtained with CPT for those systems were

discrepant: some reported the slip BC as the more appropriate [21–24], whereas others supported the use of the no-slip BC [25–27]. Despite the amount of published data, a systematical investigation to identify the source of contradiction is missing, and the results shown here are aimed to solved this discussion. Finding the source of disagreement among CPT measurements has an impact beyond the users of this technique, motivating the search for disagreements among results of other techniques, and consequently leading to a consensus about the right BC to be applied.

In the next chapter (Chapter 1), the models for drainage of liquid between a sphere and a plane, solid surface are described, including the surface forces between the sphere and the plane surface. A review of the articles debating the applicability of the no-slip BC to CPT drainage measurements is also presented. The employed instrumentation, materials, and methods are described on Chapter 2, with a detailed description of the procedure for data analysis.

The results, and the accompanying discussion, are organized in Chapter 3. Two main sections are presented: one describing experiments with a SiO_2 surface, and another with experiments with a graphite surface. In those sections, results show that by using two different parameters based on experimental variables, the data obtained in this work and data reported in the literature could be separated in two different groups: one needing the no-slip BC to be explained, and another the slip BC. The parameters are dependent on the spring constant of the cantilever, suggesting that artifacts may also be the cause for the residual slippage observed. Possible artifacts have been investigated, and their effect on measured slip lengths are reported in Chapter 3. The provided parameters provide a quantitative limit to guide the user to avoid controversial results.

The conclusions are summarized in Chapter 4, followed by a brief outlook with ideas for future studies. Images of the surfaces of the colloidal probes cited throughout the work are shown separately in the first appendix, and the images from patterned substrates are shown in the second appendix. A third appendix shows results gathered from the calibration of cantilevers before and after particle attachment, studying whether particle attachment

alters the results of the calibration process.

1. Fundamentals

1.1. Theory for Flows near the Solid–Liquid Interface

The simplest form to model flows is to assume that fluids do not have internal friction [1]. However, real fluids show resistance to shear when in motion, which is quantified by a property called viscosity [7]. Assuming a small fluid element, the viscosity η is the proportionality constant between the shear stress τ applied at the top in the x direction (Fig. 1.1) and the velocity gradient $\partial u/\partial z$ (Eq. 1.1). Liquids that follow this relationship are called Newtonian liquids. The velocity gradient is also called shear strain rate, or simply shear rate $\dot{\gamma}$ [7].

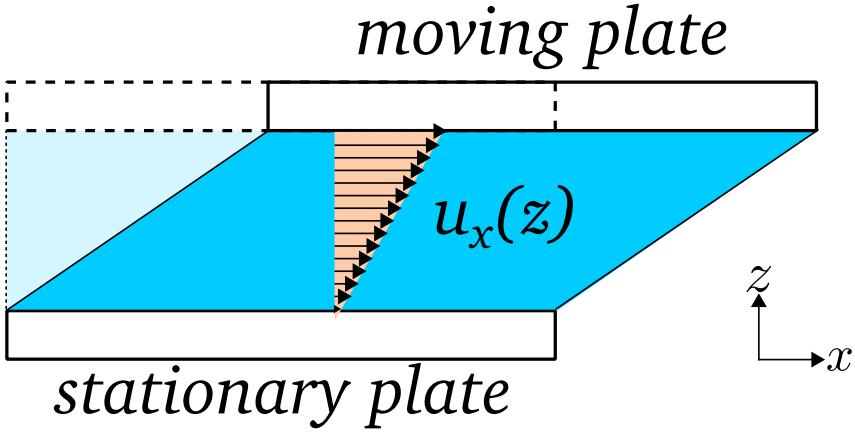

Fig. 1.1.: Diagram of flow of a liquid between plates, caused by the movement of a top plate over a stationary lower plate. The coordinates used are defined. $u_x(z)$ is the velocity of the liquid in the x direction for a point in the z direction.

$$\tau = \eta \frac{\partial u}{\partial z} = \eta \dot{\gamma} \tag{1.1}$$

The equations for flows of non-viscous fluids were derived in the eighteenth century by L. Euler [2]. These equations, though applicable to certain problems of low viscosity fluids, have a drawback: they erroneously predict that objects moves through fluids without resistance [1]. The mathematical model that could explain the experimental results came only in the second half of the nineteenth century, when a viscosity term was included [2]. These equations, developed by G.G. Stokes based on the earlier work of C.-L. Navier, are known as the Navier-Stokes (N-S) equations [28]. The N-S equations for the flow of an incompressible, Newtonian fluid, have the form of Eq. 1.2a and Eq. 1.2b, with $\mathbf{u}$ being the flow velocity, ρ the fluid density, p the pressure, and $\mathbf{F}$ representing additional body forces per unit volume acting on the fluid [28].

$$\rho \left(\frac{\partial \mathbf{u}}{\partial t} + (\mathbf{u} \cdot \nabla) \mathbf{u} \right) = -\nabla p + \eta \nabla^2 \mathbf{u} + \mathbf{F} \tag{1.2a}$$

$$\nabla \cdot \mathbf{u} = 0 \tag{1.2b}$$

The solution of the N-S equations leads to the velocity and the pressure fields, from which the drag force can be calculated [1]. As differential equations, the N-S equations require boundary conditions (BC). In the nineteenth century, when the equations were becoming more accepted, the choice of the appropriate BC was not settled [13]. In Fig. 1.2, a diagram displays the two main alternatives devised at that time, still in current use: the no-slip BC and the slip BC.

The use of the no-slip BC was favored by several early observations suggesting that there is no relative movement of a liquid adjacent to a solid. Fig. 1.2 has an illustration of the no-slip BC, with the solid-liquid interface as the axes origin and z the axis perpendicular to

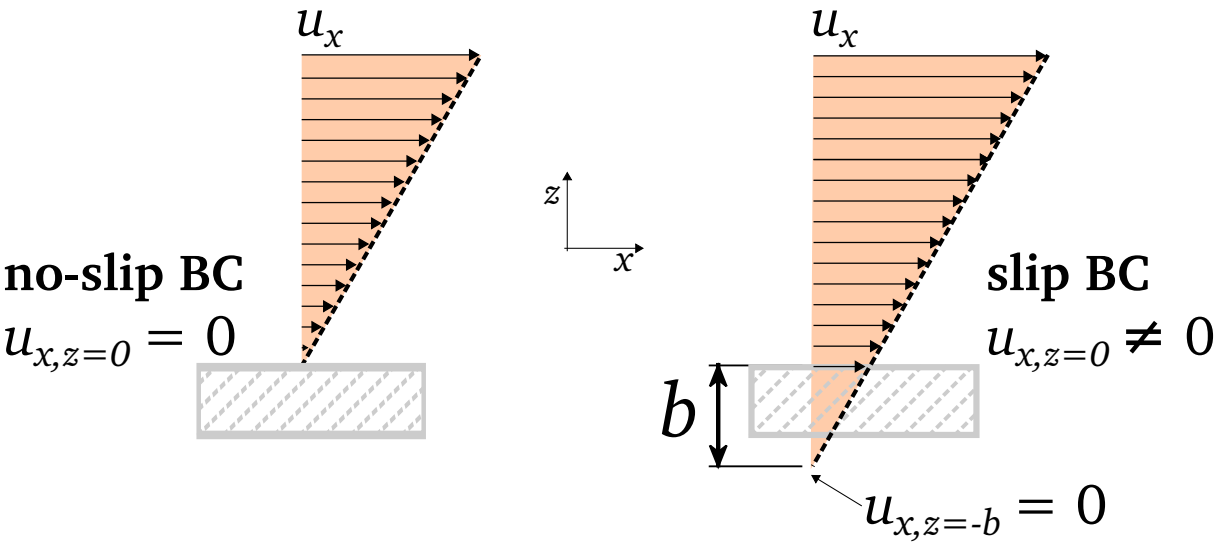

Fig. 1.2.: Diagram of the no-slip (left) and the slip (right) boundary conditions. Arrows represent the magnitude of the fluid velocity u_x as a function of z. The flow profile is approximated as linear, and the solid surface is assumed to be at rest. In the case of slip BC, the slip length b is the extrapolated hypothetical distance inside the solid where the fluid velocity would become zero.

the surface. In the no-slip BC, it is assumed that the velocity u_x of the liquid in contact with a solid surface has the same velocity of the surface. If the velocity of the lower solid surface is zero, it can be stated that the flow velocity at the boundary vanishes ($u_{x,z=0} = 0$).

In contrast, the slip BC assumes that the fluid has a finite velocity at the solid-liquid interface. The most used formulation for the slip BC is the Navier slip BC (Eq. 1.3), where the velocity of the liquid adjacent to the wall is proportional to the bulk velocity. The constant b, independent of the shear rate, is called the slip length. One of the ways to interpret this constant is to represent it as the length inside the solid where the liquid velocity would theoretically vanish (Fig. 1.2).

$$u_{x,z=0} = b \cdot \frac{\partial u_x}{\partial z} \tag{1.3}$$

Neither the no-slip BC, nor the slip BC, has a tested physical justification of its validity and their use is dictated by experimental observations [13]. This lack of justification has generated several discussions in the literature. In the nineteenth century, many scientists

reported that the slip BC would be appropriate for their experiments, whereas others applied successfully the no-slip BC [14]. These discussions were followed by a period of few experimental studies on flows at the solid-liquid interface, and at that time, the experimental results supported the use of the no-slip BC [13]. The consensus was that the no-slip BC was the best choice, and slippage would occur in a scale below the observable limits of the experimental techniques of that period [13]. Slippage was expected to appeat only for cases in which the liquid does not wet the solid, or for flows at higher shear rates than those available at that time [14].

Currently, the no-slip BC is well accepted for many systems, being commonly the only one described in introductory fluid dynamics textbooks [1, 28]. Nevertheless, the slip BC is widely accepted to explain the results for other systems, such as the flow of rarefied gases [17], polymer melts [18], and the motion of solid-liquid-gas contact lines [19]. The hypothesis raised to justify both BCs are described in the next section.

1.2. Physical Justifications of the Boundary Conditions

Many hypotheses have been raised to explain the use of both BCs. Here, after the description of the justifications for the no-slip BC, the discussion about the slip BC is divided in two parts. The term slippage is used for cases in which the liquid has a finite velocity at the boundary (Section 1.2.2), whereas the term apparent slippage is used for cases in which other processes occur (Section 1.2.3).

1.2.1. No-Slip BC

The main hypothesis justifying the use of the no-slip BC is that the last layer of liquid is bonded to the solid because surface forces exists between molecules of the liquid and of the solid surface [1]. One way usually employed is to relate the surface forces to the wettability of the solid by the liquid [29]. The contact angle θ between a drop of liquid and solid surrounded by a gaseous atmosphere is normally employed as a parameter of the

wettability of a solid by a liquid. θ can be described in equilibrium, in its simplest case, by the Young's equation ($\gamma_{LG} \cdot \theta = \gamma_{SG} - \gamma_{SL}$), where γ_{LG} is the interfacial tension on the liquid-gas interface, γ_{SG} is the interfacial tension of the solid-gas interface and γ_{SL} is the interfacial tension on the solid-liquid interface. However, only the solid-liquid interfacial energy is relevant when analyzing the flow boundaries [26]. The picture is complicated for systems exhibiting chemical heterogeneity, in which different adhesions could lead to different boundary conditions to be applied in a small space.

Surface roughness of the solid is also used as a justification [30]. The collision of the liquid molecules to the asperities of the surface provides dissipation of energy, bringing the molecules to rest at the surface. Another justification is derived from the gas theory, and extended to liquids. Modeling liquid molecules as spheres, one may assume that the molecules close to the solid surface collide with it, bouncing back to collide with other molecules. If the mean path of the molecules is too small, as in a liquid, there is a loss of energy that leads to a relative zero velocity of the liquid [31]. In the case of a rarefied gas, the mean free path is large enough to allow the molecules to have a tangential velocity and slip.

1.2.2. Slip BC

A hypothesis for the validity of the slip BC is that, if the no-slip BC is valid because the liquid does not flow for being attached to the surface, if the interaction of the surface with the liquid is weak, there should be a transition between the no-slip BC to the slip BC. Experimental results support the occurrence of slippage on non-wetted surfaces [32–37], with a large acceptance inside the scientific community. Super hydrophobicity has been also shown to lead to slippage [38]. This argument is controversial, existing experimental results showing that the no-slip BC is valid for the flow of a viscous PDMS oil over a hydrophobized glass [25]; It has been suggested that the force per molecule applied in some of the experiments is not high enough to surpass the surfaces forces [25]. The occurrence of slip was also shown for partially or totally wettable surfaces [21, 23, 39–44], in which

the liquid-solid interaction is larger. Moreover, the polarity of the liquid [45] and adsorption of surfactants [14] to the surface have also been shown to influence the value of the slip length.

Another possibility is that upon increasing the shear rate, the liquid attached to the surface could be set in motion. It has been suggested that the Navier slip BC (Eq. 1.3) is just part of a more generalized nonlinear BC that diverges at a critical shear rate [46]. The simulated critical shear rate for causing slippage of water was too large ($\approx 1 \times 10^{11}$ s^{-1}) when compared to those experimentally achievable. Experimental results are divergent: some authors found shear-rate dependent slippage [40, 47, 48], whereas others did not [21, 36, 39, 49]. Shear rate dependence is understood for the flow of polymer melts because of its non-Newtonian behavior, attributed, among other options, to the disentanglement of the polymer chains [18, 47].

1.2.3. Apparent slippage

In some cases, a slip length b has to be applied to explain the results, without meaning that the fluid velocity at the boundary is different from that of the adjacent surface. This effect is called apparent slippage, arising from a lack of resolution of the employed technique, or an oversimplification of the model (Fig. 1.3). The flow profile will be different if, at the boundary a layer exists in which the properties are not the same as in the liquid bulk. Using a technique without resolution to measure the flow at this small layer, one must use extrapolations from the available data, which would yield a slip length, without any liquid slippage happening. This apparent slippage alternative is not modern: in the nineteenth century, it was already discussed that slippage could be caused by a thin, immobile layer of liquid adjacent to the surface [14].

A layer of different viscosity is an alternative to interpret the slip length b (Fig. 1.2). If δ is the thickness of the layer close to the surface, η_W is the viscosity of this layer, and η_B is the viscosity of the liquid in the bulk, then b can be calculated following Eq. 1.4 [29].

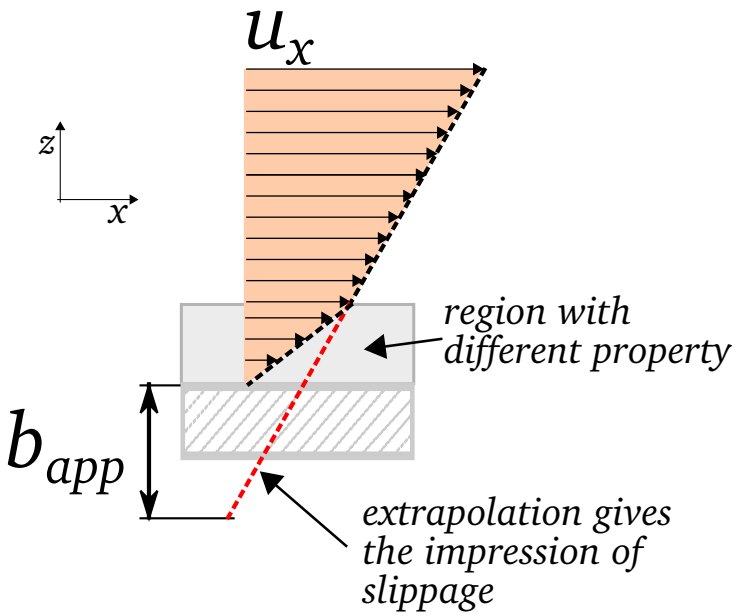

Fig. 1.3.: Illustration of how a layer with a different property may cause the impression of slippage because of extrapolation.

$$b = \delta \left(\frac{\eta_B}{\eta_W} - 1 \right) \tag{1.4}$$

A layer of reduced viscosity will lead to an apparent slippage. The presence of a continuous layer of gas separating the liquid and the surface would reduce the friction between them, allowing a situation close to perfect slippage [50]. For example, the relation between viscosities of air and water is approximately equal to 50, a value that substituted in Eq. 1.4 yields slip lengths as high as 500 nm [51]. Gaseous nanobubbles have been used as an explanation for shear rate dependent results, because they may deform or detach [51]. Nevertheless, their existence is a matter of discordance in the literature, with groups observing nanobubbles [52], whereas others report their absence [53].

The layer may also have a higher viscosity than in bulk, causing not slippage, but an immobilization of the liquid, yielding a negative slip length. There are recent experimental results that have been interpreted as if such a viscous layer adjacent to the surface existed [54–56]. For instance, a study on the interaction between surfaces covered with hydroxy-terminated thiols shows results compatible with a layer of 5 nm which is orders of

magnitude more viscous than in the bulk [55]. In the case of aqueous solutions, the ion type may play a role on the formation and structure of these layers [57]. Notwithstanding, there are results showing that simple liquids have viscosities similar to those in bulk even for small separations [14].

Asperities and roughness may also form a layer where the flow profile is different. Real surfaces with random roughness are difficult to model, and an alternative has been to model them as smooth surfaces, by defining a hypothetical plane somewhere between the valleys and peaks of a rough surface. The results obtained after this approximation had different outcomes, mainly because of the arbitrary positioning of this equivalent surface. Some simulations indicate that a rough surface could increase the slippage effect [58, 59], whereas others have predicted a decrease on slippage [60–62]. The experimental results on roughness are conflicting as well [39, 63–66].

1.3. Measuring Flows near Solid-Liquid Interfaces

There has been a continuous interest to experimentally prove the hypotheses shown in Section 1.2, and to identify factors that could lead to a slip BC case. The limitation has been the resolution of the available techniques. At the nineteenth century, the measurements were done in macroscopic instruments, such as pendulums, rotatory discs, or capillaries [67]. The boundary conditions were inferred indirectly, by the drop in the pressure caused by friction with the surface. The device miniaturization in course since the middle of the twentieth century [68] boosted the development of techniques capable of measuring flows at the solid-liquid interface at smaller distances than previously done.

1.3.1. Direct methods

Direct measurements are those in which the velocity of the fluid near the solid surface is measured, either by determining the full velocity profile or by measuring locally the velocity at a fixed distance from the surface. Modern techniques employing this concept are particle

image velocimetry [69], fluorescence recovery after photobleaching [70], and fluorescence correlation spectroscopy (FCS) [71]. In fluorescence recovery after photobleaching, the lateral movement of the fluorescent-labeled molecules is not monitored individually: part of the probes are photochemically decomposed by a laser with a spot of known size and profile, and the fluorescence intensity of the bleached region is monitored as a function of time. Since the liquid tends to homogenize itself, labeled probes diffuse into the bleached area, and the observed increase in intensity with time can be related to the diffusion coefficient of the probes. If a shear stress is imposed, the flow velocity will be superposed to the diffusion coefficient.

In FCS, a diluted solution of fluorescent-labeled particles is employed, so that only a few molecules are within the focal spot, usually between 1–100 molecules in 1 fL. After exciting the molecules, the fluorescent light is acquired at two spots, and the flow speed can be extracted from the correlation between signals at the spots. One of the setups developed uses total internal reflection optics (Fig. 1.4), allowing measurements at distances as small as 80 nm [72]. In this technique, the excitation beam is the evanescent wave generated by the reflected beam. The fluorescence signal is then divided in two identical beams, and the different observation volume is defining by setting pinholes at each beam that are approximately 1 μm apart from each other. Despite the improvements, these techniques still rely on extrapolations to infer the flow at the surface, which can lead to apparent slippage effects.

The results obtained with these techniques for the flow of aqueous solutions over hydrophilic surfaces are discrepant [14, 15]. For example, particle image velocimetry results were published supporting the [35], but there are also reports of slippage [42, 69]. FCS experiments follow the same trend: There are results supporting the no-slip BC [73], whereas others reported slippage [72, 74].

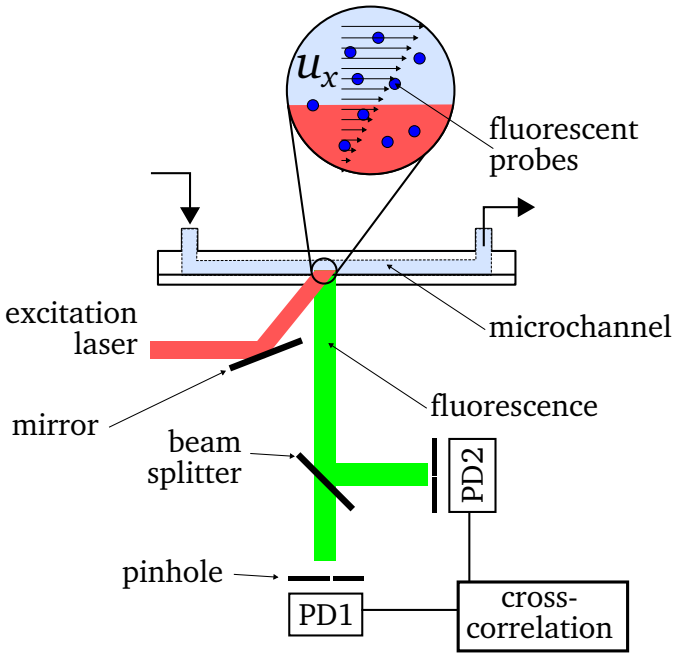

Fig. 1.4.: Example of a direct method for flow measurement: Total internal reflection fluorescence correlation spectroscopy flow measurement. Each of the pinholes define a different observation volume that is approximately 1 µm apart from each other. The cross-correlation of the signals from these two observations volumes is related to the flow velocity of the probe. Illustration based on drawings from Ref. [72].

1.3.2. Indirect methods

In other techniques, the flow at the interface is indirectly inferred by comparing the value of a measured property to the expected one according to the theory. One example is the pressure drop on capillaries of small diameters [32]. If the flow rate of the liquid insides these capillaries is higher than expected when using the no-slip BC, there is less resistance, hence the slip BC would be more suitable. There are many studies using capillaries testing which BC should be used, many of them reporting slippage [14]. There are also results showing an increased resistance to flow inside the capillary [15]. For the flow of water over inside hydrophilic microchannel, there is a report of slip lengths within the error of the measurements [75]. This type of experiments are prone to errors due to difficulties in having smooth, regular, and chemically homogeneous inner surfaces [14]. Measurements have also been performed with quartz crystal resonators [14]. The oscillatory frequency of

the crystal is related to the medium surrounding it, and variations on that can be used to infer the behavior at the interface [76]. Quartz resonators have the advantage of achieving the highest shear rates.

The drainage of thin liquid films between solid surfaces is another type of indirect measurement. When two surfaces are brought together inside a liquid, the liquid has to be squeezed out for the contact between the surfaces to be reached. Drainage experiments are important for understanding colloidal systems, where experiments with drops and solid surfaces have been performed either through image analysis [77] or optical interferometry [78]. For modeling this kind of experiments, the Navier-Stokes equations are solved in the lubrication approximation [79] and inertial terms usually neglected.

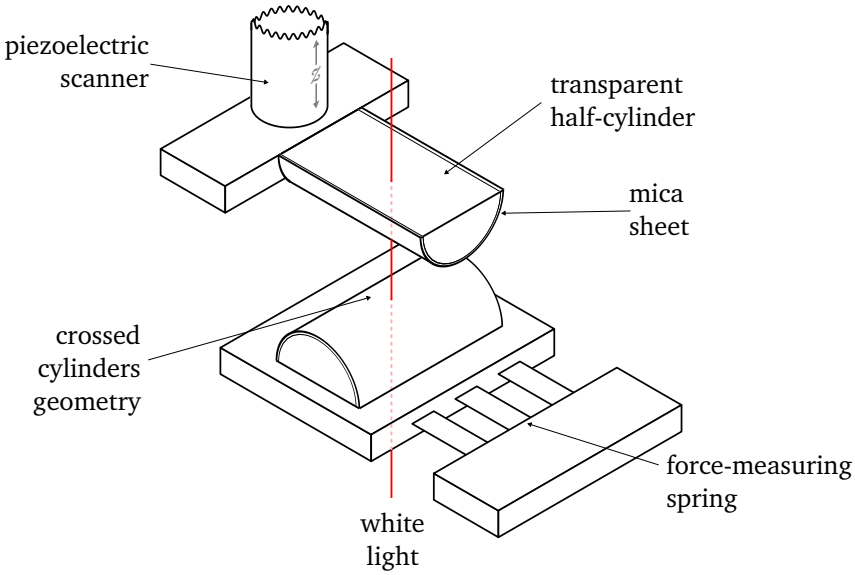

Fig. 1.5.: Example of a direct method for flow measurement: Surface force apparatus. Scheme emphasizing the crossed cylinder geometry.

Drainage measurements may be performed also through force measurement techniques, such as atomic force microscopy (AFM) and the surface force apparatus (SFA). With the development of the SFA for operation in liquids [80], the measurement of surfaces forces was greatly advanced, being possible to measure them down to separations lower than one nanometer. The SFA is based on the interaction of two crossed cylinders covered with a mica sheet, where one is driven by a piezoeletric scanner and the other attached to a

spring (Fig. 1.5). The distance between both surfaces is measured by optical interference and the deflection of the spring is related to force between the cylinders. Several articles have reported drainage experiments using SFA [14, 15]. For the case of drainage of aqueous salt solutions over smooth hydrophilic surfaces, the no-slip BC has been shown to be valid [81–84], with exception of slippage attributed to dissolved gases [30], or surfactants [85].

The measurement of the liquid drainage between two solid surfaces can be alternatively performed using the AFM, reaching a similar resolution to the SFA, but with smaller interacting surfaces. For that, a spherical particle is attached at the free end of a cantilever, and experiments are performed at high speeds. Varying the material of the microparticle, more surfaces can be assessed beyond mica. This technique will be described in more detail in Section 1.4.

1.4. AFM and the Colloidal Probe Technique

Atomic force microscopy (AFM) is a scanning probe technique introduced in 1986, arising from the combination of the principles from the scanning tunneling microscope and profilometry [86]. In AFM, the probe consists of a tip mounted at the free end of a microfabricated cantilever. The sample surface is scanned with this probe, which allows the measurement of topographical features with nanometric resolution. The radius of curvature of an AFM tip is in the order of few nanometers, with commercial ones being currently as low as 2 nm [87]. Not only topography can be measured: Probe modifications have allowed many other properties to be simultaneously quantified, for instance, the measurement of electrical properties with high spatial resolution [88]. An atomic force microscope uses a piezoelectric scanner to translate either the sample or the cantilever along the three axes, depending on its configuration. Fig. 1.6 displays an illustration of an instrument where the sample is moved toward the probe.

AFM imaging can be performed with the tip in mechanical contact with the surface, a

mode normally used for samples not damaged by the interaction with the tip. To image fragile samples, operation modes in which the tip contacts the sample intermittently, or do not contact it, have been developed [89]. In imaging with the tip in contact with the surface, the sample is moved toward the probe while the deflection of the cantilever is monitored. The sample is moved by a piezoelectric scanner along the three axes (Fig. 1.6). The deflection of the cantilever is normally measured by the optical lever method [90], in which a laser focused near the free end of the cantilever, and the reflected beam is monitored by a photodetector (Fig. 1.6). Once the tip contacts the surface, the applied load of the tip on the sample is kept constant through a feedback circuit. The sample is moved laterally along the x and y directions, while the topography is extracted from the displacements of the piezo scanner in the z direction needed to keep the applied force constant. AFM has extensive application in material characterization, especially because it does not require a special environment for the sample. Its operation with the probe immersed in liquids has enabled, for example, the imaging of biologic samples [91].

The interaction between the tip and the surface can also be measured using AFM. The sample position is fixed at one point and the deflection of the cantilever is recorded as a function of the movement of the piezo scanner. The resulting graph of cantilever deflection versus sample displacement has to be converted into one of force versus tip-sample separation, also called force-distance (F-D) curves. This conversion will be thoroughly described in Section 2.2.3. F-D curves are a result of the attractive and repulsive forces acting on a given system [92], and AFM allows their determination with a high resolution. F-D curves also provide information about mechanical properties of the sample, which can be inferred from the data obtained after the tip contacts the surface [92].

The tips normally used for imaging for AFM force measurements limit the possible interaction pairs, since few different materials are avaialble as commercial tips. To circumvent this, a particle can be attached to the cantilever instead of a tip, in a technique called the colloidal probe technique (CPT) [93, 94]. Moreover, a spherical geometry may be chosen to simplify the equations representing the forces; Usually spherical particles with diameters

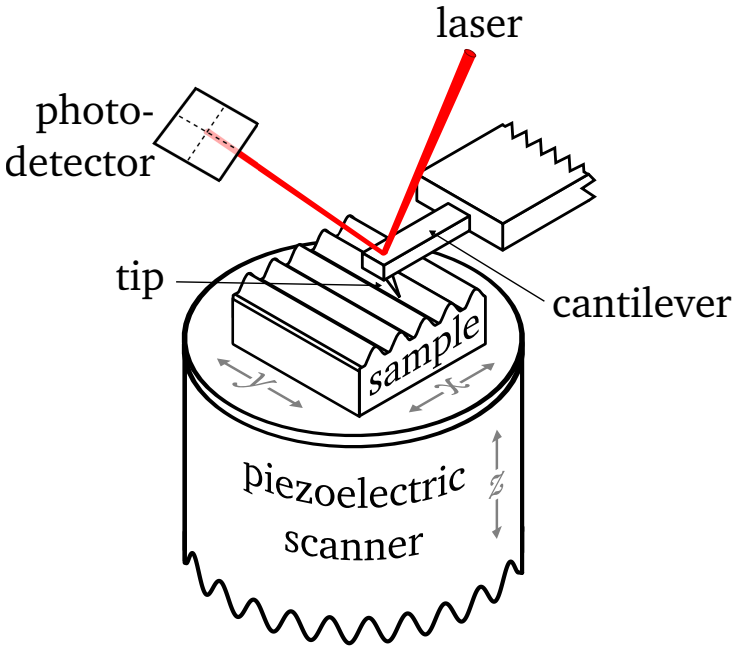

Fig. 1.6.: Diagram of an atomic force microscopy setup using the optical lever method. Here, it is shown a configuration in which a piezoelectric scanner moves the sample. A cantilever with an attached tip is used to probe the surface of the sample. A laser beam is focused near the free end of the cantilever and the reflected beam is monitored by a photodetector. The parts are out of scale.

between $1-20$ μm are used. The surface morphology of the particles is characterized either by scanning electron microscopy, or by scanning the attached probe against a grid of tips using AFM [95].

Fig. 1.7 presents a schematic drawing of a CPT measurement. The forces acting on the probe may be separated in two groups. Forces that act along the entire cantilever (F_{clv}) are treated as a distributed load, and forces on the sphere (F_{sph}) are simplified as a concentrated load on the free end of the cantilever. Additionally, in Fig. 1.7 common parts, such as the piezo scanner and the photodetector, are represented and the symbols used on the next sections are defined. Δz_p is the distance moved by the piezoelectric scanner, Δz is the corresponding deflection of the cantilever, h is the distance between the sphere and the surface, and h_0 stands for the initial separation. The deflection signal ΔV is obtained from the photodetector, and the cantilever is inclined by an angle α.

Hydrodynamic drag forces are present when CPT measurements are performed inside a

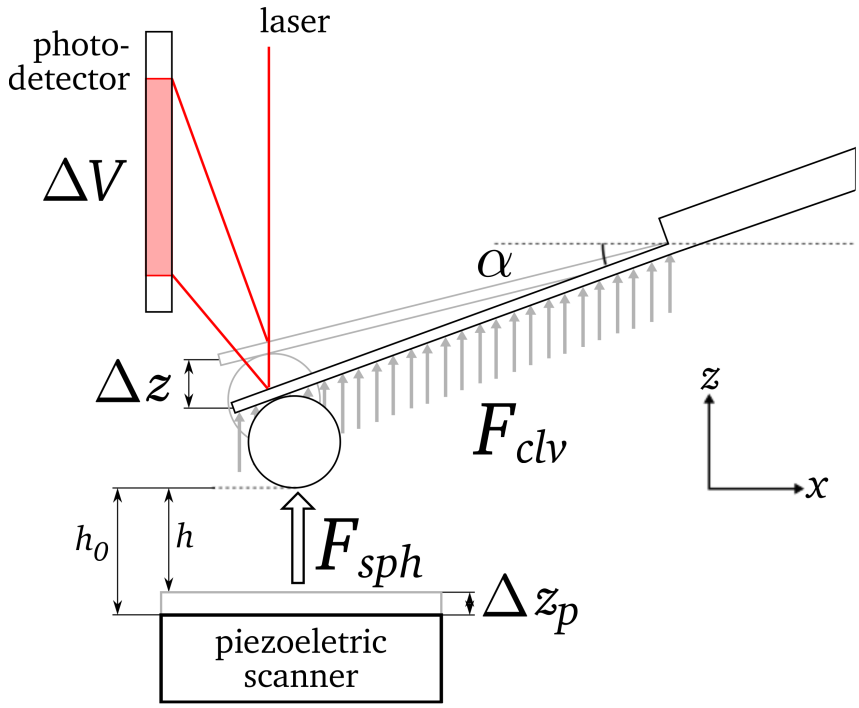

Fig. 1.7.: Schematics of a deflection measurement with the CPT in liquid environment. A sphere attached to the cantilever is pushed against a substrate and two kinds of forces act on the cantilever: a concentrated, end-load force F_{sph}, and a distributed load, F_{clv}. The inclination at the end of the cantilever is detected by an incident laser using the optical lever method. The signal is proportional to the voltage ΔV displayed by the photodetector. Δz is the corresponding deflection of the cantilever, and Δz_p is the displacement of the piezo.

liquid. The particle attached to the cantilever has to overcome these drag forces to contact the sample surface. If the parameters are properly chosen, the technique can be optimized to measure the forces required to drain the liquid between the particle and the sample surface. There has been many published articles employing AFM-CPT to study properties of thin, liquid films [54]. There has been also many articles using it to test the validity of the no-slip BC for the flow of Newtonian, polar liquids over hydrophilic surfaces, resulting in discrepant results that will be reviewed in Section 1.6. Before that review, in the next section, it will be described the forces acting on the probe during a CPT drainage measurement, and the equations used to model the results of this work will be presented.

1.5. Forces Involved in a CPT Drainage Experiment

CPT can be optimized to measure drainage of thin, liquid films, but the hydrodynamic drag is not the only force present when two solid surfaces interact across a liquid medium. Depending on the properties of solid and liquid being studied, solvation, electrokinetic, depletion, van der Waals, and electric double layer repulsion forces may be present [96, 97].

This work is focused on the interaction between polar surfaces across concentrated aqueous monovalent salt solutions, and the prevalent forces for these systems are described in the next subsections. First, the surface forces acting between the sphere and the solid substrate are described, namely the van der Waals force and the electric double layer repulsion, and their interplay in the DLVO theory (Section 1.5.1.3). Afterward, the hydrodynamic forces acting on the attached particle and along the cantilever are described (Section 1.5.2.2). The elastic force of the cantilever acts to balance these forces, and the model used assuming the cantilever as a spring is described (Section 1.5.2.2). Finally, the differential equation used to simulated a CPT drainage experiment is presented.

1.5.1. Surface Forces

1.5.1.1. Electric Double Layer Forces

Solid-liquid interfaces normally have charges in their surfaces, even if disconnected from an electrical source. These surface charges are formed in different processes, such as the ionization of functional groups covalently-attached to the surface, adsorption of ions, or isomorphous substitution of cations in clay materials [98]. The organization of the liquid at the interface is affected by these charges, especially if the ions are present. The ions are free to move inside the solution and will organize themselves near the interface to neutralize the net charge.

The theory of Gouy-Chapmann-Stern describes the ion distribution near a charged inter-

face as if they were two parts: a static layer of counter-ions, called the Stern layer, and a diffuse layer where the excess surface charge vanishes into the bulk (Fig. 1.8). This theory combines earlier concepts from Helmholtz-Perrin parallel-plate model and the Gouy-Chapman diffuse charge model [99]. From the original idea of the parallel-plate model with two layers of charges, the ones in the solid and the counter-ions in solution, stems the name electric double layer EDL. The term is widely used despite the contemporary knowledge that the distribution is often more complex than only two layers [100].

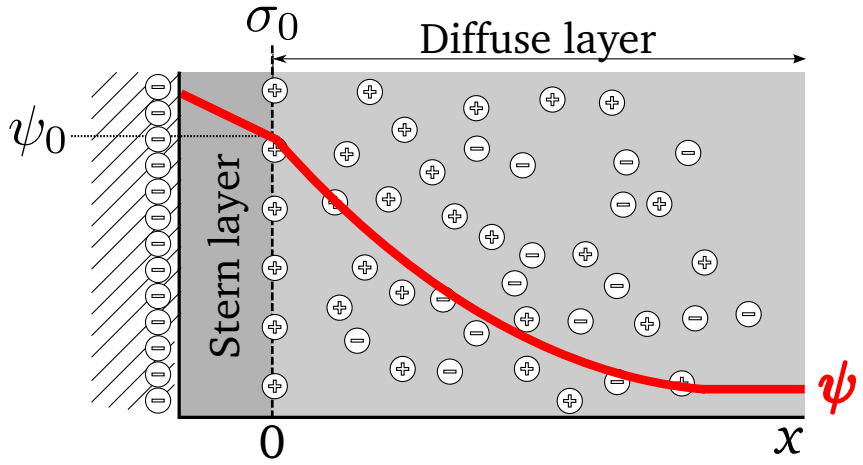

Fig. 1.8.: Schematics of the ion distribution near a charged surface according to Gouy-Chapman-Stern theory. The red line depicts the decay of the potential (ψ) as a function of the distance x from the surface. Based on figures from Refs. [99] and [100].

The interaction between charged surfaces inside a liquid cannot be described simply by Coulomb's law, because the interfacial ion distribution shields the charges from solid surfaces. The potential as a function of distance from the interface must be determined to calculate the force of interaction. Following the theory of Gouy-Chapman, the electric potential ψ can be determined through the Poisson-Boltzmann (P-B) equation. Assuming an infinite planar surface at the limit of low potentials ($e_0|\psi| \ll k_B T$), and a solution of an electrolyte with monovalent ions, the linearized form of the P-B equation is given by Eq. 1.5, where k_B is the Boltzmann constant, T is temperature, ε is the relative permittivity of the surrounding medium, ε_0 is the vacuum permittivity, e_0 is the elementary charge, and c_0 is the electrolyte concentration.

$$\frac{d^2\psi}{dx^2} = \frac{2c_0e_0^2}{\varepsilon\varepsilon_0 k_B T} \cdot \psi \tag{1.5}$$

Assuming that the ψ vanishes at infinity and that $\psi(0) = \psi_0$, the solution to Eq. 1.5 is:

$$\psi = \psi_0 \cdot e^{-\kappa x} \tag{1.6}$$

where

$$\kappa = \sqrt{\frac{2c_0e_0^2}{\varepsilon\varepsilon_0 k_B T}} \tag{1.7}$$

The decay length of the potential κ^{-1}, called the Debye length, is used to estimate the thickness of the ionic cloud [99]. At 25 °C, the Debye length is approximately 1 nm for a 0.1 mol/L aqueous solution of an electrolyte with monovalent cations and anions [97].

The obtained potential ψ (Eq. 1.6) is then used to calculate the force for the interaction between two planar surfaces. However, the geometry used on CPT experiments is that of a sphere interacting with a plane surface. A useful approach is to use the Derjaguin approximation, which states that the energy of interaction between bodies of arbitrary shape can be calculated by integrating the energy per unit area of two planar surfaces [97]. The Derjaguin approximation is valid if the decay length of the forces is much smaller than the curvature of the surfaces, a condition satisfied in CPT measurements with particles usually in the order of few micrometers. After derivation, the force F_{EDL} between the sphere and the plane with identical surfaces arising from the interaction of the electric double layers is given by Eq. 1.8 [97].

$$F_{EDL} = \frac{128\pi R c_0 k_B T}{\kappa} \tanh\left(\frac{\varepsilon\psi_0}{4k_B T}\right) \cdot e^{-\kappa x} \tag{1.8}$$

1.5.1.2. van der Waals Forces

A point charge is attracted to another one with an opposite sign, or repelled if the sign is equal. The force is proportional to the square of the separation between the charges. Ions can be approximated as points charges, and the force of interaction between two ions can be calculated by Coulomb's law.

Many molecules do not have a net charge, but have partial charges distributed inside their structure. They are called polar molecules, and may be described in the simplest case as a dipole. Dipoles may interact with ions or with other dipoles. If the molecules are free to rotate, these interactions are attractive, because the dipoles tends to align themselves with opposite charges facing each other. Other molecules are apolar, having no preferential orientation of their electrons. However, when they come closer to polar molecules, an attraction exists: the dipole induces a polarization on the apolar molecule, termed dipole–induced-dipole interaction. Apolar molecules also interact with other apolar molecules; the attraction between them arises because of high frequency fluctuations on the electronic density of the molecule. This is called an induced-dipole–induced-dipole interaction.

Dipole-dipole, dipole–induced-dipole, and induced-dipole–induced-dipole forces are commonly grouped together and referred as van der Waals forces [97, 101]. To calculate the force for the interaction between two macroscopic solids, the van der Waals forces between all atoms and molecules of both have to be integrated. Neglecting the influence of molecules in the vicinity of any pair of interacting molecules and using the Derjaguin approximation, the force between a sphere and a flat surface can be calculated by Eq. 1.9 [97], where A_H is the Hamaker constant, R is the radius of the sphere, and h is the distance between the sphere and the substrate.

$$F_{vdW} = -\frac{A_H R}{6h^2} \tag{1.9}$$

The A_H is an empirical constant that includes contributions from all three interactions between polar and polarizable atoms and molecules. For example, two SiO_2 surfaces in-

teracting with each other across an aqueous medium have reported values of A_H in the range of $0.16 - 1.15 \times 10^{-20}$ J [97, 102]. The van der Waals interaction between atoms or molecules in vacuum is always attractive. The interaction between two solids is in most cases also attractive, but it can be also repulsive if the solids are of different nature and one of them has a higher interaction with the medium separating them than the other [97].

In Eq. 1.9 it is neglected that atoms have a finite radius, beyond which they are impenetrable at the conditions used here. This leads to a repulsion force that prevent further contact between the surfaces. To include this repulsion, a term derived from a Lennard-Jones potential can be used (Eq. 1.10), introducing a factor S that defines a minimum separation between the solids [103]. For a CPT measurement, a value of 0.5 nm is reasonable, being lower than the observed roughness of particle and substrate.

$$F_{vdW} = -\frac{A_H R}{6h^2}\left(1 - \frac{S^6}{4h^6}\right) \tag{1.10}$$

1.5.1.3. DLVO Theory

Independent calculations by Derjaguin and Landau, and by Verwey and Overbeek on the coagulation of colloids are known as the DLVO theory. In these calculations, they assumed that the interaction between two surfaces could be described by the sum of the van der Waals forces and the EDL repulsion. In the limit of low surface potentials, the total force on the sphere according to the DLVO theory F_{DLVO} is described as a function of the distance h between sphere and surface as:

$$F_{DLVO} = F_{EDL} + F_{vdW} = \frac{128\pi R c_0 k_B T}{\kappa}\tanh\left(\frac{\varepsilon\psi_0}{4k_B T}\right)\cdot e^{-\kappa h} - \frac{A_H R}{6h^2} \tag{1.11}$$

1.5.2. Hydrodynamic Forces

In a CPT drainage measurement, the flow generated by approaching the probe against the substrate can be approximated as a Stokes flow, in which the viscous effects are pre-

dominant and the Navier-Stokes equations can be linearized [1]. For this assumption to be valid, the Reynolds number $Re = \rho u L_c/\eta$ must be smaller than the unit [1], a condition met since the characteristic length L_c is in the micrometer scale for all parts of the probe, and the velocity is also small, in the order of μm/s · The fluid is also assumed to be Newtonian and incompressible.

The probe consists of a spherical particle attached to a cantilever. As a simplification, it is assumed that the total hydrodynamic drag on the probe is the sum of the hydrodynamic drag on the particle and the drag on the cantilever. This assumption is satisfied for the probes used here, which have particles with diameters larger than 10 μm [104]. In the next subsections, the drag on the sphere and on the cantilever are separately described.

1.5.2.1. Drag Force on a Sphere Approaching a Solid Surface

The expression for the drag on a sphere falling through a liquid at $Re < 1$ has been derived by Stokes in the nineteenth century [1]. If dh/dt is the velocity of sphere, the drag force on the sphere is:

$$F = 6\pi\eta R\frac{dh}{dt} \tag{1.12}$$

Eq. 1.12 was derived assuming the no-slip BC. The drag force is then proportional to the viscosity, to the radius of the sphere, and to the velocity of the sphere. If the sphere moves toward a rigid, solid surface, the drag force on the sphere has to account for the extra resistance coming from the drainage of the liquid from the solid surface. Assuming the no-slip BC, the drag force on the sphere when approaching a solid is then represented as [20]:

$$F_{hyd} = -\frac{6\pi\eta R^2}{h}\frac{dh}{dt} \tag{1.13}$$

This expression, usually called the Taylor equation [105], shows that the drag F_{hyd} on a rigid sphere approaching a solid surface is inversely proportional to the separation h

between the two solids. Eq. 1.13 was derived under the lubrication approximation, in which it is assumed that the thickness of the drained liquid film is much smaller than the dimensions of the interacting surfaces [1, 106]. There is also a solution that is not dependent on the lubrication approximation [107], but for CPT measurements it has been shown that the difference from Eq. 1.13 is negligible.

A correction to Eq. 1.13 has been developed assuming the slip BC [108]. The equation is modified by a correction factor f^* that is a function of the slip length b (1.2). The expression commonly used in modeling the experiments for the case of two similar surfaces approaching each other is given by Eq. 1.15. f^* is always smaller than 1 by definition. If f^* is set to 1, Eq. 1.14 is reduced to the Eq. 1.13.

$$F_h = -\frac{6\pi\eta R^2}{h}\frac{dh}{dt}\cdot f^* \tag{1.14}$$

$$f^* = \frac{h}{3b}\left[\left(1+\frac{h}{6b}\right) ln\left(1+\frac{6b}{h}\right) - 1\right] \tag{1.15}$$

An exact analytical solution assuming the no-slip BC is available [107]. The differences between the approximate solution (Eq. 1.13) and the exact solution is negligible for $h < 2\,\mu m$ [14, 27]. A exact solution assuming slip BC does not exist, and comparing experimental data using equations solved for different frameworks can lead to more difference than using the approximated solution.

1.5.2.2. Drag Force on the Cantilever

At the speeds employed in CPT drainage studies, not only the hydrodynamic drag on the sphere is measured; the hydrodynamic drag on the cantilever (F_{clv}, Fig. 1.7) has a large contribution and must be included in the calculations. Many groups have studied the effect of drag arising on dynamic measurements [109–114]. Despite the effort, no exact description of the drag on the cantilever exists, and empirical coefficients are needed to calculate the force. Many of the previous studies assumed that the drag on the cantilever is

proportional to the speed of the piezo scanner, $F_{clv} = -C_D \cdot v_p$. This assumes that the drag force is constant, as v_p is controlled and set constant during the experiment. However, this assumption leads to an overestimation of the drag.

Here, the drag on the cantilever is assumed proportional to the sphere velocity dh/dt through a drag coefficient C_D (Eq. 1.16 [115, 116]). The drag coefficient has to be experimentally determined for each experiment. This equation assumes that the speed of the cantilever is equal to dh/dt, and it accounts that when the cantilever is deflected, the relative velocity of the cantilever is lower than v_p, resulting in a lower drag force value.

$$F_{clv} = -C_D \cdot \frac{dh}{dt} \tag{1.16}$$

Assuming that the speed of the cantilever is equal to dh/dt is not strictly valid, because the cantilever deflection makes the relative speed (and consequently F_{clv}) vary along its length. The base of the cantilever moves with a velocity equal to v_p during the measurement, whereas the free end of the cantilever slows down the closer it gets to the surface. The free-end of the cantilever, and thus the attached particle, suffers a strong deceleration that may lead to inertial effects. It has been shown that this effect has low impact in the final result [116–118]. In Eq. 1.16 it is also neglected that liquid drainage also happens under the cantilever, which may cause an increase in the drag force inversely proportional to its distance to the solid surface. However, for colloidal probe particles with $R > 10$ μm, the interaction of the cantilever with the solid surface can be neglected [104].

1.5.3. Differential Equation Describing a CPT Drainage Measurement

In a CPT measurement, the forces described in the previous subsections are balanced by the restoring force of the cantilever. In the model used here, the cantilever elastic force is assumed to be in quasi-equilibrium with the measured forces at each time step of the experiment, despite being an experiment performed under dynamic conditions [20].

In AFM force measurements the cantilever is usually modeled as an equivalent spring-

mass system. According to the Euler-Bernoulli theory of beam deformation, the deflection z_{clv} of a cantilever beam caused by a force F acting on its free end is related to the Young's modulus E of the material, its moment of inertia I, and its length L (Eq. 1.17).

$$F = \frac{3EI}{L^3} z_{clv} \tag{1.17}$$

Comparing Eq. (1.17) to Hooke's law $F = kx$, the spring constant k of the cantilever can be defined as:

$$k = \frac{3EI}{L^3} \tag{1.18}$$

Assuming a rectangular cantilever and substituting I for this geometry, the equivalent spring constant k can be related to the t_c given by Eq. (1.19) [92], where t_c is the thickness of the cantilever, and w its width.

$$k = \frac{Ewt_c^3}{4L^3} \tag{1.19}$$

The final differential equation is seen in Eq. 1.20. Inertial and acceleration effects were ignored, considered too small to play a role in the measured forces [20]. The right side of Eq. 1.20 represents the elastic force of the cantilever, acting to restore the cantilever to its initial rest position. The speed of the piezo scanner (v_p) is assumed to be constant throughout the experiment. $h_{0,app}$ and $h_{0,ret}$ are the initial separation between microsphere and substrate on approach and on retract, respectively. F_{clv} stands for distributed forces on the cantilever, here representing the hydrodynamic drag described in Section 1.5.2.2 and F_{surf} the surface forces sensed by the sphere, as summarized in Sections 1.5.1.2 and 1.5.1.1. The solution of Eq. 1.20 is $h(t)$, the deflection of the cantilever as a function of time, that after further calculations yields a simulated F-D curve. Details of this conversion procedure will be described in Section 2.2.

$$-\frac{6\pi\eta R^2}{h}\frac{dh}{dt}\cdot f^* + F_{clv} + F_{surf} = \begin{cases} k(h - h_{0,app} + v_p t) & \text{on approach} \\ k(h - h_{0,ret} - v_p t) & \text{on retract} \end{cases} \tag{1.20}$$

CPT measurements can be optimized in such a manner that hydrodynamic forces are predominant in the final result, as can be inspected in Eq. 1.20. The measurements are performed at high v_p or high η, as the surface forces are not dependent on speed nor on viscosity. Additionaly, v_p may be kept constant during approach and retract to simplify the calculations. The radius of the particles are also large, because the hydrodynamic equations show a square dependence on the particle radius, whereas the van der Waals and EDL forces show a linear dependence on it.

1.6. Controversy on CPT Flow Measurements of Water on Hydrophilic Substrates

The right BC to be applied on modeling the flow of Newtonian fluids is a debate in the literature, with many techniques involved, as summarized in Section 1.3. In the case of CPT drainage measurements of polar, Newtonian liquids over hydrophilic surfaces, there has been a clear disagreement on the magnitude of the measured forces on these drainage measurements: although some authors report experimental data consistent with the no-slip BC, others measured forces that are considerably lower than predicted by the equations in which the no-slip BC is assumed. Attempts have been made to reconcile the two types of measured force curves, but a satisfactory explanation for the observed differences has not yet been found.

Table 1.1 shows results published in the last years studying the validity of the no-slip BC on polar, Newtonian liquids flowing over hydrophilic substrates. In the cases in which slippage was reported, the Navier slip BC (Eq. 1.3) was used. Inspecting Table 1.1, it is seen that more results were published supporting slippage than those that showed the

validity of the no-slip BC. While some suggest that this amount of evidence supports the existence of slippage [14], others have pointed that publication bias may be responsible by the low amount of data supporting the no-slip BC. This implies that because the no-slip BC is widely accepted, few researchers have interest in submitting articles confirming an already accepted hypothesis [119], an effect known, for example, in pharmaceutical clinical trials [120]. It is then important to find the cause of the discrepancy between the results, since pure statistical evidence does not solve the discussion.

The experiments so far reported use experimental parameters considerably different between articles (Table 1.1). It stands out the variable range of viscosities employed, as well as the range of cantilever spring constants. It has been suggested that the force applied by soft cantilevers might not be high enough to ensure real contact of the microsphere to the surface [116]. To independently measure the separation between the particle and the surface, a combination of an atomic force microscope and an optical monitoring the intensity of the evanescent field reflected by the microsphere. In that work [116], only cantilevers stiffer than those used in previous articles ($k > 0.6\,\mathrm{N/m}$) were used, and although it was shown that a real contact happen for stiff cantilevers, no data were presented showing that soft cantilevers fail to contact the surface. If rough surfaces are used, along with the described doubt about its effect on slippage, the contact point of the tip with the substrate is also difficult to define. The argument that only stiff cantilevers ensure that a no-slip BC will be satisfied [25] is contrasted to a result of a 0.1 N/m-cantilever that validates the same condition [121].

Some of the published articles [24, 40, 122] report slip lengths values dependent on the driving speed, which has been attributed to artifacts [26, 116], such as non-linearities on the detector or on the failure of attaining contact between the microsphere and the substrate. These results have never been reproduced, and the cause behind them has not been experimentally identified. In the last column, it is included a parameter $\eta v_p/k$, which can be related to the appearance of slippage on the published results. This parameter, along with another one, will be discussed in detail and compared to newly performed results to

check whether the trend observed in the literature is sustained.

There has been many other hypothesis about causes for the observed disagreement, including the shape of the cantilever [123], an incorrect treatment of the drag on the cantilever [115], or contamination by nanoparticles [115]. Though these hypotheses could explain why slippage was observed in a small subset of experiments, none of them explained all of the results obtained previously. For example, in the case where the shape of the cantilever has been pointed as the cause of apparent slippage [123], the conclusions were drawn for a small subset of the results shown in Table 1.1. It was argued that triangular cantilevers lead to lower forces and consequently to an apparent slip length. The reason for this discrepancy was not explained, and observing Table 1.1, slip BC had to be applied to explain results taken with rectangular cantilever.

The discussion on the literature poses questions whether the results are reproducible or were just a result of the contamination or artifacts. It remains the question of which BC should be applied for CPT drainage measurements of polar, Newtonian liquids over hydrophilic surfaces. The results presented in next sections show a series of factors that may be causing this discrepancy.

Table 1.1.: Measured slip lengths previously published in the literature, compared by their experimental parameters, for studies of the validity of the no-slip BC for the flow of Newtonian, polar liquids over hydrophilic substrates using the CPT. b, slip length; k, spring constant; v_p, speed of the piezo scanner; R, radius of the sphere ; η, viscosity; L, cantilever's length and w, width of the cantilever.

	Article	b / nm	k / N/m	v_p / μm	R / μm	η / mPa·s	L	w / μm	Medium	Shape	$\eta v_p/k/1\times10^{-6}$
A	Honig and Ducker [26]	1±1	4.5	10	9.3	69	130	35	Rectangular	Sucrose(aqueous, HCl, pH 3)	0.15
B	Honig and Ducker [26]	-5±2	4.5	100	9.3	88	130	35	Rectangular	Sucrose(aqueous, HCl, pH 3)	1.96
C	Honig and Ducker [116]	-3±2	8	50	10	58	130	35	Rectangular	Sucrose(aqueous, HCl, pH 3)	0.36
D	Vinogradova and Yakubov [121]	0	0.1	20	5.2	0.89	450	52	Rectangular	NaCl(aqueous, 10^{-3} mol/L)	0.18
E	Sun et al. [23]	14	0.2-1.6	84	9	2	100	40	V-shaped	Propanol	0.84
F	Bonaccurso et al. [64]	43	0.15	16.2	12.55	6.15	196*	41*	V-shaped	Sucrose(aqueous)	0.66
G	Bonaccurso et al. [64]	44	0.15	16.2	12.55	19.2	196*	41*	V-shaped	Sucrose(aqueous)	2.07
H	Bonaccurso et al. [64]	42	0.15	43.2	12.55	6.15	196*	41*	V-shaped	Sucrose(aqueous)	1.77
I	Bonaccurso et al. [21]	9	0.012	4	10	0.89	210	52.5	Rectangular	KCl(aqueous, 0.2 mol/L)	0.3
J	Bonaccurso et al. [21]	9	0.012	40	10	0.89	210	52.5	Rectangular	KCl(aqueous, 0.2 mol/L)	2.97
K	Craig et al. [22]	0	0.11	2.4	10.4	27	196*	41*	V-shaped	Sucrose(aqueous)	0.59
L	Craig et al. [22]	5	0.11	21.6	10.4	19.2	196*	41*	V-shaped	Sucrose(aqueous)	3.77
M	Craig et al. [22]	12	0.11	21.6	10.4	38.9	196*	41*	V-shaped	Sucrose(aqueous)	7.64
N	Neto et al. [24]	Slip	0.10	20	10.4	80	196*	41*	V-shaped	Sucrose(aqueous)	16

2. Materials and Methods

2.1. Substrates and Solutions

2.1.1. Solutions

Aqueous solutions were prepared with ultra-pure water (Arium 611, Sartorius, Germany, Resistivity = 18.2 MΩ · cm). The pH of water varied between 5.5 and 6.0. At this pH range, the Debye length may reach more than 100 nm, meaning that F_{EDL} has a large contribution to the final measured force. To lower this contribution, potassium chloride (KCl) (99+% for analysis, Acros Organics, Belgium) was added to the solutions to yield concentrations higher than 0.1 mol/L, keeping the Debye length under 1 nm. Sucrose (98%, Aldrich, UK) was added to KCl aqueous solutions to increase their viscosity in experiments showed in Section 3.1.4. Alkaline chlorides (RbCl, NaCl, KCl, and LiCl, 99.99+%, Aldrich, UK) were used in experiments showed in Section 3.2.

2.1.2. Substrates

Silicon wafers were chosen as substrates for most of the experiments because of its hydrophilicity. The surface of a silicon wafer is covered by a native layer of amorphous silicon dioxide (SiO_2) [124], composition similar to the particles attached to the cantilevers. The SiO_2 surface is terminated by –SiOH groups that dissociate in water, with $pKa \approx 4$ [125]. The wafer was cut in square pieces (edge ≈ 1 cm), that were rinsed extensively with ethanol and ultra-pure water, then blown dry with filtered compressed air. After this wet cleaning,

the samples were cleaned in an argon plasma (PDC-002, Harrick Scientific Inc., USA) for 5 minutes. This cleaning procedure was performed immediately before each measurement, using always a new piece of silicon for each measurement.

HOPG (NT-MDT Co., Moscow, Russia) was employed in experiments from Section 3.2. The HOPG surface is composed of graphitic carbon, and is known to be smooth in tens of nanometers scale, presenting steps in macroscopic range. HOPG has a layered structure, allowing samples to be cleaved just before use, with no further cleaning, by using the tape method. This method consists in pressing an adhesive tape on top of the surface and then removing it, leaving the old layer glued on the tape. The procedure was repeated until the layer attached to the tape became uniform, thus avoiding residues of glue on the new surface.

2.2. Force-Distance Measurements

All force-distance (F-D) measurements were carried out with a commercial atomic force microscope (MultiMode with PicoForce module, Veeco, USA). The Picoforce module has a piezoelectric scanner with a low-noise capacitive sensor, which independently measures the displacement of the piezo scanner in the z-axis. The signal of this sensor is integrated into a feedback loop, keeping linear the displacement of the piezo scanner. The module provides also a low-noise head with a low-coherence length laser diode to lower the noise caused by interference between the reflected beams from the cantilever and from the sample.

The graphs showed here contain 25 different F-D curves measured in different positions of the surface. Each position was 5 μm apart from each other in both x and y directions, yielding a square of 5 × 5 raster points. Measurements in different positions ensure that contaminations and imperfections of a single part of the substrate do not have a large contribution in the final curve. Piezo speeds v_p were calculated from the displacement curves recorded by the integrated position sensor of the vertical movement of the piezo scanner.

2.2.1. Cantilevers

Table 2.1 lists the nominal specifications and suppliers of different tipless cantilevers used here. Rectangular cantilevers were preferred, but V-shaped cantilevers were used to check if the shape of the cantilever could affect the results. Cantilevers were cleaned before measurements, following the same procedure used for cleaning the substrates. They were assembled first assembled on the probe holder of the instrument, and then rinsed with ethanol and water before plasma cleaning for 5 minutes (Argon plasma, PDC-002, Harrick Scientific Inc, USA).

Table 2.1.: Cantilevers used here: Nominal specifications and suppliers. k is the spring constant, w the width, L the length, and t_c is the thickness of the cantilever. NP stands for non-provided specifications.

	shape	w / μm	t_c / μm	L / μm	k / N/m	Provider
1	Rectangular	35	1	350	0.03	MikroMasch (Estonia)
2				300	0.05	
3				250	0.08	
4	Rectangular	35	1	130	0.6	
5				110	0.95	
6				90	1.75	
7	Rectangular	35	2	350	0.3	
8				300	0.35	
9				250	0.65	
10	Rectangular	35	2	130	4.5	
11				110	7.5	
12				90	14.5	
13	Rectangular	52	3	200	NP	Micromotive (Germany)
14	V-shaped	23	NP	196	0.06	Veeco (USA)
15		13	NP	100	0.32	

2.2.1.1. Particle Attachment

The colloidal probes were made by attaching particles to the tipless cantilevers described above (Table 2.1). Borosilicate-glass spherical particles with nominal diameters of 10 μm and 20 μm (Duke Scientific Corporation, USA) were used throughout all experiments de-

scribed here. Borosilicate-glass spheres were chosen for having the smallest roughness among the particles commercially available with this size [126]. Nevertheless, all particles were imaged before use (Section 2.3). Particles with peaks around the contact region were discarded, and only particles with a spherical shape and root mean square (RMS) roughness lower than 3 nm were used.

Spherical particles were attached to cantilevers using a thermoplastic glue (Epikote 1004, Shell, Germany), using an already established procedure [93, 94, 127]. A glass slide with particles on its top side was placed on a heater plate under the objective of an optical microscope. On the same slide, a small amount of glue was placed farther from the area with the particles. The slide was then heated up to the softening point of the glue (80 °C). Using a micro-manipulator (three dimensional oil-hydraulic manipulator MNO-203, Narushige Group, Japan). The cantilever was moved to pick up a small drop of glue on its tip. A particle without any visible irregular shape surface was searched among those lying atop the slide. The cantilever with the glue drop was then gently pressed against the particle and withdrawn from the hot region to allow the glue to solidify.

2.2.2. Cantilever Calibration

The spring constant of the cantilever is needed to convert the deflection data into a F-D curves. From the definition of spring constant for a rectangular cantilever (Eq. 1.19), the knowledge of E, t_c, w, and L would be sufficient to calculate it. In practice, the cantilevers normally used in AFM measurements have micrometric sizes, requiring techniques such scanning electron microscopy for measuring its dimensions [128], both expensive and time consuming. Besides, a non-uniform t_c causes an error propagated in a cubic relationship, and inhomogeneities can cause error on the value of E [92]. Experimental techniques have been devised to circumvent those problems, such as the measurement of resonance frequency and quality factor of a vibrating cantilever and relating it its dimensions [129], the frequency change due to the addition of a known mass [130], pushing the cantilever against a pendulum [128], a reference cantilever [131], or nanoindentors [132].

Here, the thermal noise method [133] was used to calibrate all cantilevers. The thermal noise method is present nowadays in most AFM instruments, widely use for being fast and easy to perform; Currently, none of the other methods present a better compromise between usability, reliability, agility, and precision as the thermal noise method does.

In the thermal noise method, k is estimated based on the analysis of the random vibration of the cantilever caused by thermal fluctuations, normally called thermal noise [133]. The cantilever beam is assumed as a spring-mass harmonic oscillator in equilibrium with its surroundings. After applying the equipartition theorem [134], the k is calculated to be inversely proportional to the power $< z^2 >$ of the thermal noise spectrum, and can be determined by Eq. 2.1, with k_B being the Boltzmann constant, and T being the medium temperature.

$$k = \frac{k_B T}{< z^2 >} \tag{2.1}$$

The initial assumptions of the thermal noise method have been discussed thoroughly in the literature, and many correction factors have been published to deal with unaccounted factors. For example, the cantilever is not described perfectly by a spring-mass system, and all the vibration modes of the cantilever have to be consider [135]. Walters et al. [136] provided the correction factor for using only the first mode of vibration to calculate the spring constant k. Following these corrections, k is related to the area P under the resonance peak by Eq. 2.2. The factor 0.8174 is the correction the proposed by Walters et al. [136] for a rectangular cantilever, and InvOLS is the inverse optical lever sensitivity, the factor needed to convert the power from volts to nanometers.

$$k = \frac{0.8174}{InvOLS^2 P} \cdot k_B T \tag{2.2}$$

Eq. 2.2 and the numerical methods needed for the calculation were already implemented on Veeco Multimode software. The InvOLS was determined by acquiring a force curve and fitting the contact portion. Cantilevers were calibrated using the same instrument (Multi-

mode Picoforce) used for force measurements. Those with higher resonance frequencies ($f > 30$ kHz) were calibrated on a Dimension CL3000 (Veeco, USA).

2.2.3. Analysis of Force-Distance Curves

2.2.3.1. General Conversion Procedure

A typical raw curve obtained in drainage experiments (Fig. 2.1a) have the readings from the photodetector in the ordinate, and the displacement of the piezo scanner in the abscissa. The displacement of the piezo scanner was measured by the integrated capacitive sensor of the instrument. Here, data obtained on the approach of the cantilever is used to describe the general procedure for converting such raw curve into a F-D curve, but it also applies to retract curves. The conversion procedure was performed through an in-house programmed software.

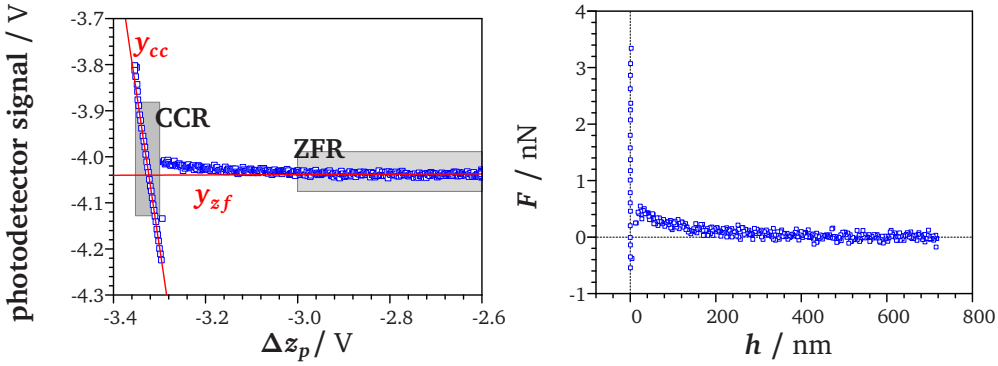

(a) Raw data **(b)** Final curve

Fig. 2.1.: Example of conversion from raw data into a F-D curve. (a) Raw data from an approach curve of a AFM force measurement (blue squares). The red lines represent linear fits ($y = ax + b$) for two different regions of the curve, highlighted by the gray box: the zero-force region (ZFR) and the constant compliance region (CCR). The ordinate shows the output from the photodetector in volts and the abscissa the displacement of the substrate driven by the piezo scanner, already converted to micrometers. (b) Final curve of deflection versus distance. The same procedure is applied for converting the retract curve (not shown here).

Before describing the procedure, two important regions of the raw curve must be defined (Fig. 2.1a, gray rectangles): The zero-force region (ZFR) and the constant-compliance re-

gion (CCR). The ZFR is the region distant from the surface, where the cantilever is not yet sensing any force. The CCR is the region where the cantilever contacts mechanically the substrate. Assuming that the substrate is not deformable, the deflection in this region is equal to the displacement of the piezo scanner, and can be used to convert the photodetector signal, originally in volts, to deflection in nanometers. The raw curve is fitted separately with linear equations (y_{ZF} and y_{CC}, continuous lines in Fig. 2.1a) and the obtained parameters are used to converting the raw curve (Fig. 2.1a) on the final F-D curve (Fig. 2.1b), following five steps [92, 137]:

1st step The raw curve is fitted with a linear equation $y_{ZF} = a_{ZF}x + b_{ZF}$ inside the ZFR region. The obtained fit curve y_{ZF} (Fig. 2.1a) is then subtracted from the raw data ordinate.

2nd step The raw curve is fitted with a second linear equation $y_{CC} = a_{CC}x + b_{CC}$ inside the CCR region. The units for the photodetector signal must be converted from the raw readings in volts to deflection units, in nanometers. The conversion factor comes from the angular coefficient of the equation y_{CC}. The raw data are then divided by a_{CC}. This step assumes that, inside the region CCR, the cantilever deflects only because of the displacement of the piezo scanner. This assumption is valid as long as cantilever response is linear and the substrate does not deform in the interval chosen for the fit.

3rd step The point x_0 (Eq. 2.3) is subtracted from the abscissa of the deflection data to bring d_{zp} to zero. x_0 is obtained from the intersection between y_{ZF} and y_{CC}.

$$x_0 = \frac{b_{CC} - b_{ZF}}{a_{ZF} - a_{CC}} \tag{2.3}$$

4th step The graph until now is still in terms of displacement of the substrate. The separation h is calculated using Eq. 2.4, with z_p being the substrate displacement, z_{clv} the cantilever deflection, and z_{def} the deformation on the substrate caused by the tip. For a rigid tip and substrate similar to those used for the experiments shown here, z_{def} can be ignored.

$$h = z_p - z_{clv} - z_{def} \tag{2.4}$$

5th step After these 4 steps, the curve should look as the one in Fig. 2.1b, but with the ordinate still given in cantilever deflection. The ordinate must be multiplied by the spring constant k to be converted to units of force,

2.2.3.2. Drainage Curves

The conversion of curves from drainage experiments follows procedure similar to the one described in the previous subsection, but requires additional steps. In AFM liquid drainage measurements, the piezo scanner is driven at speeds considered high for normal F-D measurements ($v_p > 20\,\mu$m/s). This leads to a hysteresis of the curve in the CCR, present because of the inertia of the piezo scanner moving after the set time for one of the curves. This hysteresis is compensated by fitting the CCR separately for each curve.

The hydrodynamic drag on the cantilever is also present in a drainage experiment (Section 1.5.2.2). Because of this drag, the initial deflection of the cantilever is not zero, and a hysteresis is observed between the approach (blue squares) and the retract curve (red circles) of a high speed curve (Fig. 2.2). To define the contact position, the deflection caused by the drag on the cantilever is assumed to be equal on both approach and retract. Both curves are then fitted together, being the zero-deflection line the average between the ZFR for approach and for retract.

After conversion, F-D curves were compared to the expected theoretical curves to evaluate which of the boundary conditions was more adequate. The theoretical curves were obtained by solving Eq. 1.20 numerically in Maple (Maplesoft Inc., Waterloo, Canada) using a built-in seventh–eighth order continuous Runge–Kutta method. The no-slip BC curves were solved by setting the factor f^* to 1, which means that no adjusting parameters were used. In cases when the experimental curves did not agree with the curves assuming the no-slip BC, Eq. 1.20 was solved for different values of b, and the best fitting curve was visually chosen.

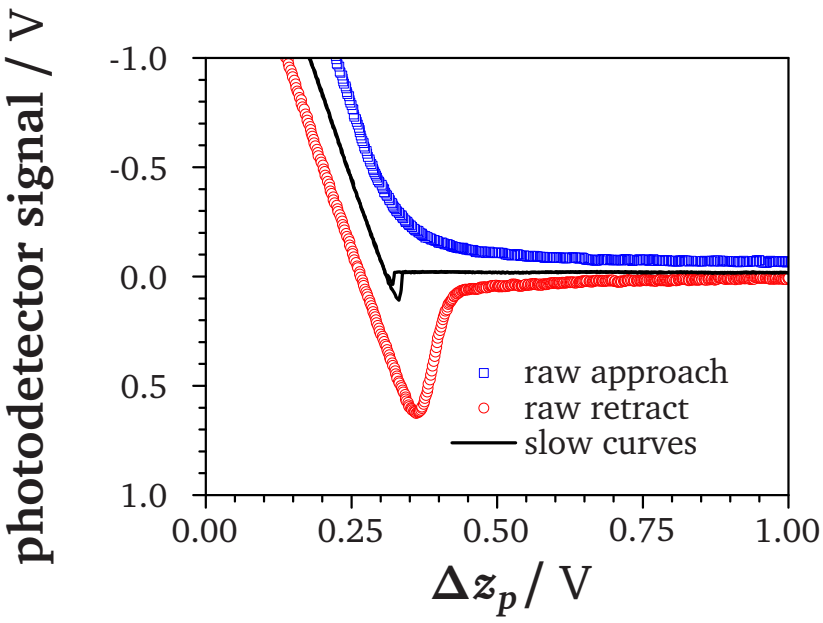

Fig. 2.2.: Comparison between raw F-D curves in water when driven at different speeds. Continuous lines are the curves obtained at 0.2 μm/s and the points for a curve driven at 55 μm/s. Both curves have not been converted, so the comparison between them can be solely made relating their shapes.

The choice for assuming the slip BC was done to allow a quantify the difference between the results and the no-slip model, and the terms “slip length” or “apparent slip length” are used as synonyms. F_{clv} was calculated using Eq. 1.16, and the drag coefficient C_D was chosen to make the calculated curves and the measured ones agree at $h > 3$ μm. F_{surf} was included in the simulation by using the DLVO theory (Eq. 1.11). According to Eq. 1.20, $h_{0,ret}$ cannot be set to 0 because it appears in the denominator. The value of $h_{0,ret}$ for each calculation was chosen to fit the retract peak best, never exceeding 0.1 nm otherwise explicitly cited.

Eq. 1.20 was solved numerically because it is not possible to solve it analytically. There are alternative methods to analyze the F-D curves [26, 40], where the experimental data are divided by the sphere velocity dh/dt. However, the sphere velocity (dh/dt) is not constant during the experiment, and its independent measurement is not currently commercially available. The procedure is to differentiate the deflection data and to subtract it from the known piezo-scanner speed v_p. This introduces error due to the differentiation, where normally the data has to be interpolated to allow the computation to be done. In addition, the velocity data are calculated from the same set of data, what amplifies the existent

noise. This alternative method also introduces errors when adding surface forces, that are not speed-dependent.

2.3. Microsphere Imaging

The surface of the microspheres glued to the cantilevers was imaged by inverse atomic force microscopy [95]. This method consists of imaging a grid with an array of sharp tips micromachined on its surface (Fig. 2.3a). Here, a TGT1 calibration grid (NT-MDT, Moscow, Russia) was used. An example of the obtained image is shown on Fig. 2.3b. The images were acquired on the Multimode or on the Dimension microscopes in contact mode.

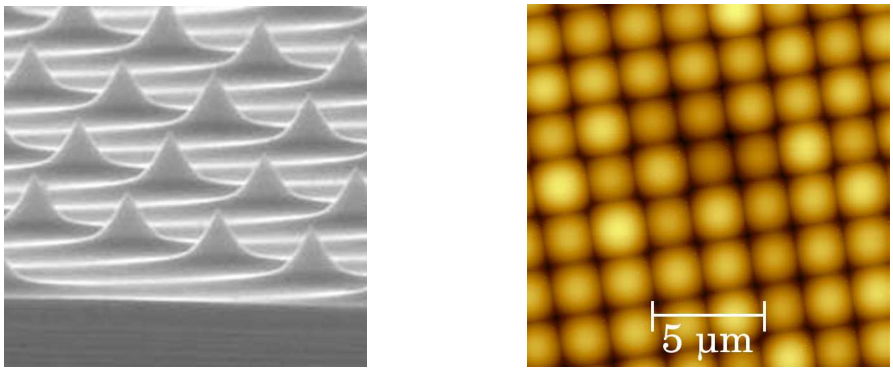

(a) (b)

Fig. 2.3.: (a) Scanning Electron Microscopy of a TGT1 calibration grid from NT-MDT. Image used under permission. ⓒ NT-MDT, Russia; (b) Example of an inverse atomic force image obtained cantilever when scanning a cantilever with an attached sphere against pattern (a)

The radius of the sphere and its roughness were determined from the obtained images. The radius of the particle was calculated by running a least-squares fit of a circle in an area of 0.5 µm × 0.5 µm around the apex of the sphere. The root mean square (Z_{RMS}) and peak-to-valley (Z_{PV}) roughness values were obtained after the spherical fit of the sphere image. The data on the apex area had the spherical background subtracted, then a polynomial background subtracted and the resultant image used for roughness determination. All image manipulation, sphere fit and roughness determination were performed using the image manipulation software Gwyddion [138].

3. Results and Discussion

The results of the experiments performed to evaluate the appropriate boundary condition (BC) to be applied for drainage measurements with the colloidal probe technique (CPT) are shown in this chapter. As discussed, a consensus over the appropriate hydrodynamic boundary condition to be applied on drainage measurements over hydrophilic surfaces using the CPT has not yet been achieved (Section 1.6).

Results of drainage experiments for SiO_2 particles interacting with SiO_2 solid surface inside a concentrated aqueous KCl solution are presented in Section 3.1. The focus of those experiments was to analyze factors causing the discrepancies observed on CPT measurements. In Section 3.1.10 the obtained data are compared to those already published, and a parameter is set to guide future experiments. Another question that can be raised whether any of the observed cases can be attributed to artifacts, for example whether soft cantilevers yield data agreeing with the slip BC are a real slippage phenomenon or an instrumental limitation. Since instruments of different brands and models have been used in the past, one more concern appears regarding the reproducibility of the previously published results, since artifacts might have been related to a specific device. Section 3.2 extends the measurements to a HOPG surface, to investigate how the hydrodynamic curves change with a surface of different surface energy.

3.1. Drainage Measurements on Silicon Substrates

3.1.1. Stiff Cantilevers

A typical graph with the representations to be used for plotting F-D curves are shown in Fig. 3.1. The initial position of the probe was typically at $h = 3$ μm, but here the attention is focused in the interval between h=0 and h=200 nm. In this interval, possible disagreements between experimental data and theory are more pronounced. In the ordinate axis it is shown the force divided by the sphere radius (F/R), a presentation commonly used in force measurements and kept here for comparison with earlier works. Dashed lines are simulated curves assuming the no-slip BC (Eq. 1.20, $f^* = 1$). As an aid, a gray rectangular box is drawn at $h = 0$, depicting the expected position of the solid surface.

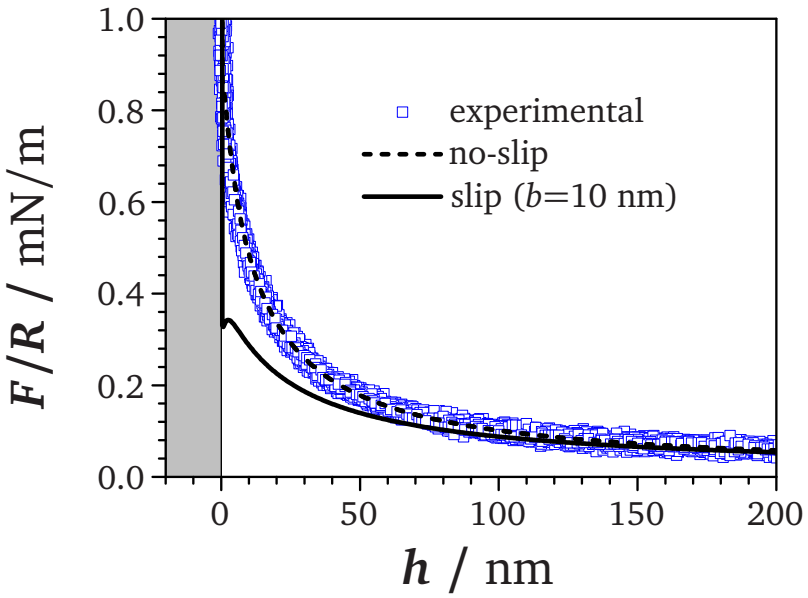

Fig. 3.1.: Approach F-D curves (blue squares) for a stiff ($k = 0.26$ N/m) rectangular cantilever against a SiO_2 surface in a 0.2 mol/L KCl solution. The experimental data are in accordance with the simulated curve using the no-slip BC (dashed line). A simulated curve ($b = 10$ nm) is assumed (continuous line) is plotted for comparison. $v_p = 55$ μm/s and $R = 10$ μm.

The F-D curves in Fig. 3.1 were acquired for the approach of a stiff rectangular cantilever ($k = 0.26$ N/m, type 2, Table 2.1, $R = 8$ μm) run at $v_p = 55.5$ μm/s. This is a representative case in which curves acquired with a stiff cantilever are in accordance with the curves

using no-slip BC. As a guide, an extra curve is included showing the force values obtained if the slip BC with a slip length $b = 10$ nm is assumed. This value of b was chosen as reference because the slip lengths reported in the literature are of this magnitude or bigger (Table 1.1). The difference between curves solved using the no-slip BC and the slip BC are clear, starting already at $h = 120$ nm.

Another feature is that for the slip BC curve, there is a small jump-in event close to the surface observed in the simulation curve is not predicted by the no-slip BC curve. The no-slip BC curve has a distinct trend: in the limit of zero separation, the force tends to go to infinity, surpassing the attraction to the surface. The curve assuming the slip BC tends to zero when in the limit of zero separation, as seen in Eq. 1.15. The vanishing hydrodynamic force described by the model allow the surfaces forces to surpass it and cause a jump-in process. This jump-in is not observed in experimental data, what emphasizes that the no-slip BC is more adequate to describe the data.

Similar results can be found in the literature [26, 116, 121], where the no-slip BC sufficed to explain the results. It has been speculated that previous slip results were caused by the lower stiffnesses of the employed cantilevers, and rather stiff cantilevers ($k > 4.5$ N/m) were used [26, 116]. The argument was that a soft cantilever does not ensure that the probe is actually contacting the substrate surface, although this hypothesis was has not been tested. Using a commercial AFM as the one used in this work, it is not possible to measure independently the particle-surface separation, and therefore if a true contact was attained. An alternative is the use of hybrid devices, for example the detection of evanescent wave scattering with the approach of the probe [139]. This technique has the drawback of needing a suitable substrate, normally transparent, what limits its applicability.

Fig. 3.2 shows data using an even stiffer rectangular cantilever ($k = 3.7$ N/m, type 3), in the same order of magnitude previously reported [116]. The experimental F-D curves agree with the no-slip BC, as in Fig. 3.1, but the signal-to-noise ratio decreased compared to when 0.26 N/m-cantilever was employed. The main source of noise is interference from the detection laser beam with reflected beam from the surface. A reflective layer on the top of

the cantilever can reduce this noise, for this ensures that the intensity of the reflected beam coming from the cantilever is higher than the reflection from the surface. The deposition of a metal layer leads to cantilever deflection due to small temperature changes, due to different expansion coefficients of the metal and silicon. To avoid that, the cantilevers used here were not coated with any layer.

The slip BC curve predicts here also a jump-in that is not observed in experimental data. The jump-in distance is different from the predicted value, and the force drops more than in the simulated curve of Fig. 3.1. The comparison between curves is not straightforward, because for each simulation the surface forces were determined experimentally during a slow run, and different particles have different roughness that interfere in the magnitude of the van der Waals forces. Also, jump-in effects are known to depend not only on the Hamaker constant, but also on the spring constant of the cantilever [140].

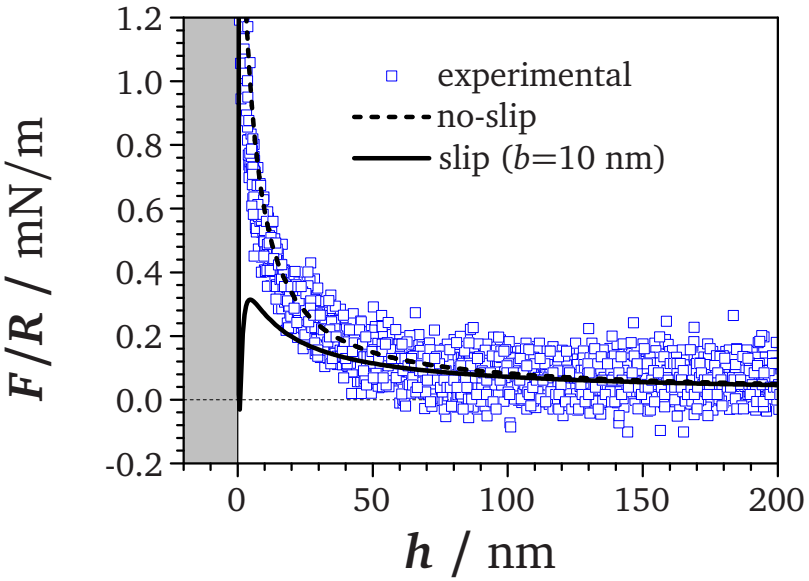

Fig. 3.2.: Approach F-D curves curves for a stiff ($k = 3.7$ N/m) rectangular cantilever against a SiO_2 surface in a 0.2 mol/L KCl solution. As in Fig. 3.1, the experimental data are also in accordance with the no-slip BC (dashed line), but the signal-to-noise ratio is much smaller. A simulated curve where $b = 10$ nm is assumed (continuous line) is plotted for comparison. $v_p = 40$ μm/s and $R = 10$ μm.

The use of the stiffest possible cantilever is not always an option to obtain data in agreement with the no-slip BC, as the use of stiff cantilevers may damage, for example, de-

formable substrates. The magnitude of the signal has to be also considered. In some of published articles, a sucrose solution was used to increase the viscosity of the medium (Table 1.1), and therefore increase the cantilever deflection. This has allowed the acquisition of reasonable signals even for a 10 N/m-cantilever [26]. In the results presented in this section, a salt solution with a viscosity close to that of water was employed, making a 3.7 N/m-cantilever not the best choice for measuring the forces. The results obtained with stiff cantilevers shows that the no-slip BC is sufficient to describe the drainage experiments performed with CPT. This is in agreement with some of the previous results with that technique, and also with experiments performed with the SFA [20]. Still, it remains unanswered the question why many works have reported previously that the no-slip BC could not be used to explain the CPT measurements, and a slip length had to be introduced instead. Another point is how to quantitatively classify a cantilever as stiff or soft enough to use the no-slip BC. In the next sections, it will be shown experiments with softer cantilevers dealing with these questions.

3.1.2. Soft Cantilevers

F-D curves for a soft ($k = 0.04$ N/m), rectangular cantilever (type 1, Table 2.1) driven at $v_p = 40$ μm/s are shown in Fig. 3.3. The graph is similar to those presented in the last section (Fig. 3.1 and Fig. 3.2), but the measured values of F/R are smaller than those calculated using the no-slip BC. Measured data only agreed with the simulation when $b = 15$ nm was used. The jump-in effect seen in the slip BC, is still present, but the jump-in distance is much smaller, for the reasons described previously.

In the previous subsection the curves simulated with the slip BC were plotted only for reference, whereas here they are plotted because they were really needed to explain the results. Another feature is that the curve shows a kink at the expected contact point ($h = 0$), while the curves obtained with stiffer cantilevers did not. This could arise because the attractive van der Waals forces start to be larger than the hydrodynamic repulsion, leading to a small jump-in event. This can be observed in the simulated curve, although the magni-

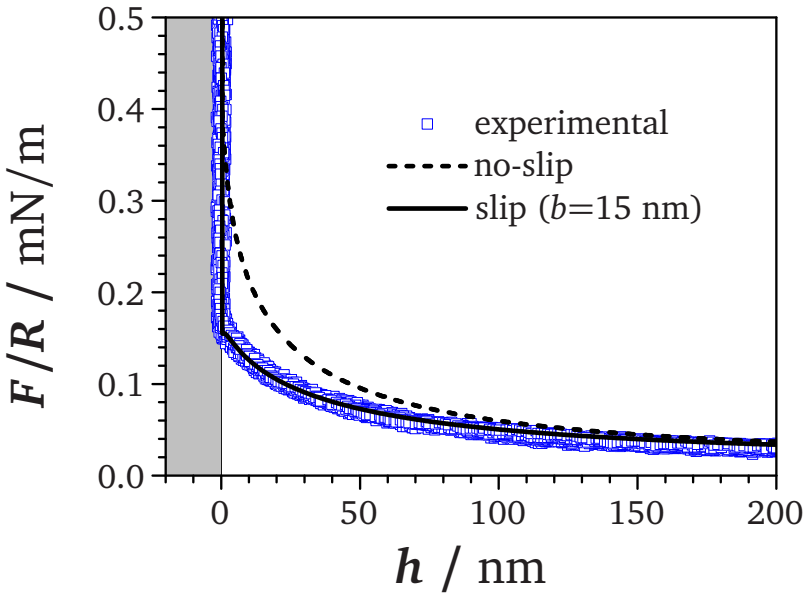

Fig. 3.3.: Approach F-D curves for a soft ($k = 0.04$ N/m), rectangular cantilever against a SiO_2 surface in a 0.2 mol/L KCl solution. The experimental data are not in agreement with the simulated curve using the no-slip BC (dashed line), and a slip length $b = 15$ nm was needed for fitting the curves (continuous line). $v_p = 40$ μm/s and $R = 8$ μm.

tude is smaller than the noise. The simulated curve assumes that a slippage process lowers the value of the hydrodynamic force, although any other process slowing the cantilever, for example the distributed drag on it, could yield an apparent slippage.

These results (Fig. 3.3) are similar to some published experiments (Table 1.1) that found that the slip BC was needed to explain the results for softer cantilevers. For instance, $b = 8.6$ nm was found in an experiment with similar parameters as those used here ($R = 10$ μm, and $v_p = 40$ μm/s) [21]. The difference between their value of b and the one found here can be a result of the roughness of the sphere, which presented a maximum peak-to-valley distance (Z_{PV}) of 5 nm over a surface of area 0.25 μm^2 centered on the apex of the sphere (Fig. A.1, Appendix). For comparison, the reported root-mean-square roughness (Z_{RMS}) of the microsphere for that experiment [21] was near 1 nm, while here the roughness was $Z_{RMS} = 0.6$ nm. The Z_{RMS} value is not a good measure of roughness, being used here for comparison with previous works. In CPT measurements, the existence of only one peak on the apex can prevent real contact, and such peak is averaged when performing RMS

calculations. Conversely, a peak far from the contact point can contribute to the Z_{RMS} and still not interfere on the contact distance.

Another possibility for the observed difference is that the particle is positioned away from the free end of the cantilever. The particle positioning was not controlled on these experiments, but an estimation assuming that the particle is positioned at a distance equal to its radius R from the free end, which would lead to $b = 11$ nm instead.

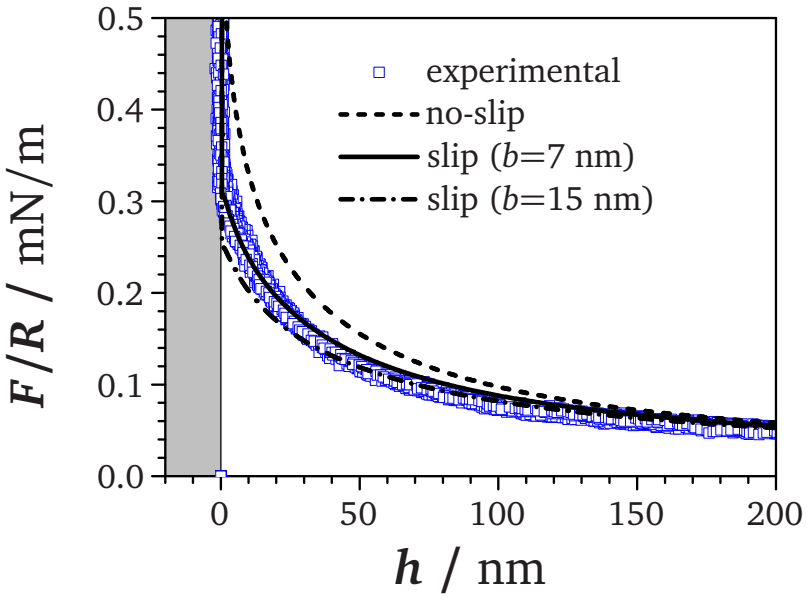

Fig. 3.4.: Approach F-D curves for a soft ($k = 0.06$ N/m), rectangular cantilever against a SiO_2 surface in a 0.2 mol/L KCl solution. The experimental data are not in accordance with the simulated curve using the no-slip BC (dashed line) and a slip length $b = 7$ nm was needed for fitting the curves (continuous line). An extra slip curve (dash-dot-dash line) with slip length $b = 15$ nm was plotted to show that in this case a single slip length was not enough for fitting the whole curve. $v_p = 55.5$ μm/s and $R = 10.6$ μm.

This trend could be observed in all experiments performed with soft cantilevers run at speeds between 40 μm/s and 50 μm/s. A further example can be seen on Fig. 3.4, where a similar cantilever (type 1, Table 2.1) with k of 0.06 N/m has been used. The results are not in accordance with the curves calculated using the no-slip BC, but two curves with different b values are displayed, showing that a single slip length cannot be used to fit the whole F-D curve. This is a tendency that was observed in experiments in which slip BC was assumed, and can be related to particle positioning, both away from the free end or away from the

central axis of the cantilever, causing twisting. In both cases the cantilever would be stiffer than it should, leading to lower deflections than expected.

The results obtained with soft cantilevers show that the previous results that needed the slip BC to be explained are reproducible. This is important because of the level of speculation around them, in which even contamination has been appointed as possible cause of an apparent slippage [141]. Though it is not possible to discard contamination in previous results, the sample preparation employed here was identical for experiments performed with stiff and soft cantilevers, and yet slippage appeared for soft cantilevers. In the next subsections, experiments focusing on some parameters will be presented as an attempt to assert whether the apparent slip length measured for soft cantilevers was caused by an artifact.

3.1.3. Retract Curves

In this section two examples of retract curves are presented. The results for the retract curves are similar to those observed for the approach ones, requiring the no-slip BC for stiff cantilevers and the slip BC for the soft ones. The retract curves for a stiff (k=0.26 N/m) cantilever is shown in Fig. 3.5. The correspondent approach curves were shown in Fig. 3.1. The curves have a different shape from those presented for approach. The direction of the movement is inverse now: the particle is in contact with the substrate in the beginning, and the piezo scanner is driven to separate both. First the adhesive forces must be overcome, and afterward the cantilever keeps deflecting downward due to the hydrodynamic drag on the sphere. At a certain point, the restoring force of the cantilever is larger than hydrodynamic drag on the sphere, causing the cantilever to jump away from the surface, in a movement attenuated by the drag both on the cantilever and on the sphere. These two regions are separated by the minimum of the curve. Here, the no-slip BC sufficed to describe the explained results, as in the approach curves. The values present a larger scattering, a variation that has been already observed [25], and can be attributed to the different adhesion in each of the points the curve was acquired.

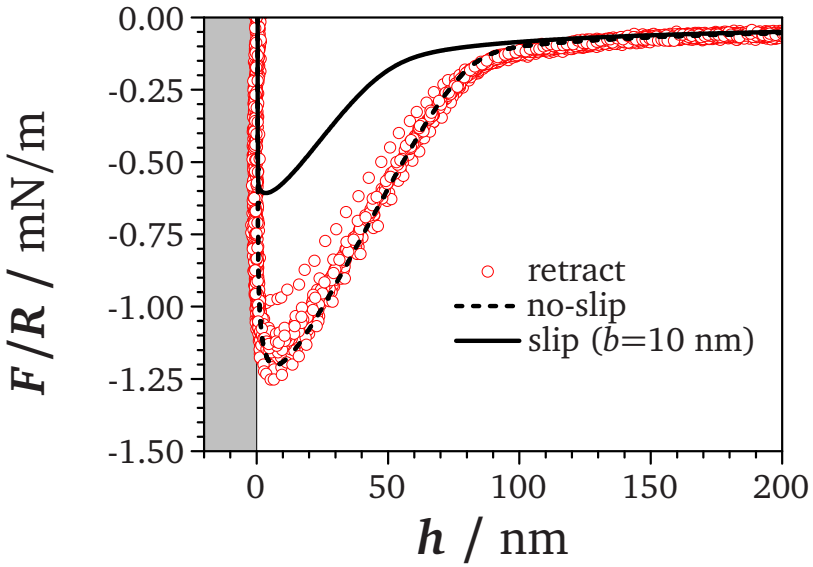

Fig. 3.5.: Retract F-D curves for a stiff ($k = 0.26$ N/m), rectangular cantilever against a SiO_2 surface in a 0.2 mol/L KCl solution. The experimental data are in accordance with the simulated curve using no-slip BC (dashed line). A simulated curve where b=10 nm is assumed (continuous line) is plotted for comparison. The approach curves were presented in Fig. 3.1.$v_p = 55$ μm/s and $R = 10$ μm.

Fig. 3.6 shows the retract curves for the same experiment with a soft (k=0.04 N/m) cantilever from Fig. 3.3. As in the approach, the obtained experimental F-D curves are not in accordance with the curves calculated using the no-slip BC and a slip BC had to be used to fit the data. Nevertheless, $b = 17$ nm was needed to adjust the data, 2 nm more than it was needed for the correspondent approach curves (Fig. 3.3). One explanation for this small difference of b between approach and retract curves is that the adhesion force between the surface and the particle, sensitive to the roughness of the sphere and to the applied load. Another possibility is related to the piezo-scanner speed and it will be discussed on Section 3.1.4.2.

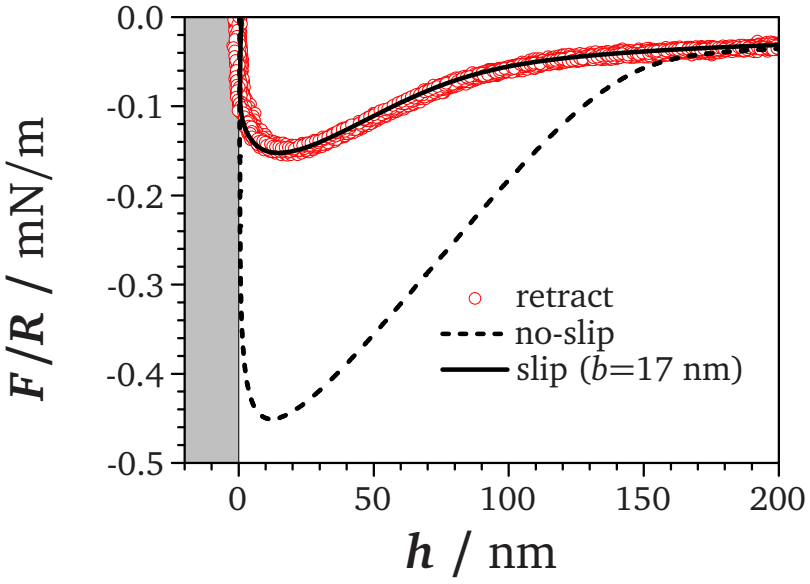

Fig. 3.6.: Retract F-D curves for a soft ($k = 0.04$ N/m), rectangular cantilever against a SiO_2 surface. The experimental data are not in agreement with the simulated curve using the no-slip BC (dashed line), and a slip length $b = 17$ nm was needed for fitting the curves (continuous line, $v_p = 40$ μm/s, $R = 8$ μm). The approach curves from this experiment were presented in Fig. 3.3.

3.1.3.1. Simulations Varying the Initial Position on Retract

An alternative way of comparing the retract data with the simulations has been suggested in the literature [25]. Instead of assuming slippage on the surface, the no-slip BC is assumed valid and the initial separation on retract ($h_{0,ret}$) is varied, later subtracting the used $h_{0,ret}$ value from the h data. The minimum separation established between the colloidal probe and the surface on approach part of the curve affects the minimum value of a retract F-D curve [142]. When solving Eq. 1.20, a separation equal to zero would lead to an infinite force because of the $1/h$ term.

Fig. 3.7 presents retract F-D curves (red circles) with F-D curves simulated using the no-slip BC for different values of the closest contact and ignoring all other terms in the Eq. 1.20. The best fit was obtained with $h_{0,ret} = 17$ nm (the same value obtained using slip BC). This value is larger than the Z_{PV} on the same area ($Z_{PV} = 5$ nm). One can observe that simulating the curves starting at $h_{0,ret} = 1$ nm instead of $h_{0,ret} = 0.1$ nm, the magnitude of the minimum of the curve is reduced in 20%. An offset in the closest contact is one of

the know drawbacks of force measurements with AFM, but a gap of 17 nm is not expected to happen.

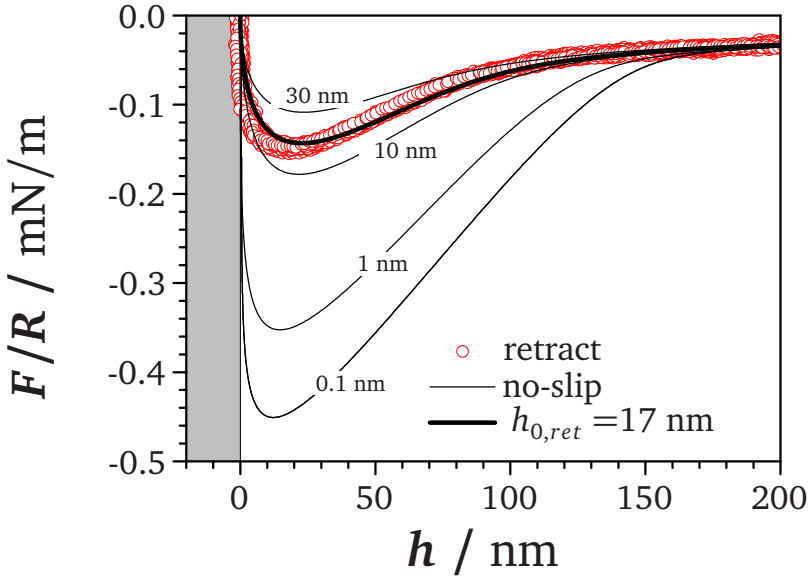

Fig. 3.7.: Retract F-D curves from Fig. 3.4, showing simulated curves (continuous lines) for different retract starting distances $h_{0,ret}$. Note that an agreement to the whole F-D curves cannot be obtained.

Qualitatively, the agreement of the 17 nm-displaced curve to the data are not as good as the curve simulated using $b = 17$ nm, especially in the part of the curve where the cantilever is jumping away from the surface. An agreement to the whole F-D curves is not obtained and either that part of the curve or its minimum can be fitted. The trend can be seen from the other fitted curves. When $h_{0,ret}$ is increased, the agreement with the jump-away part gets better, but the minimum is dislocated to the higher h values.

3.1.4. Driving Speeds and Viscosity

3.1.4.1. Piezo Scanner Linearity

In Fig. 3.2 results were presented showing that the no-slip BC was obeyed when using a stiff cantilever ($k = 3.7$ N/m). Using the same cantilever and keeping the same experimental conditions, but displacing the substrate at the maximum possible speed of the Veeco

Multimode Picoforce module ($v_p = 600$ μm/s), an apparent slippage ($b = 10$ nm) was observed. After a thorough inspection, it was discovered that the measured v_p from the raw data of the piezo-scanner displacement sensor was in fact equal to 340 nm. Employing this corrected v_p instead, the no-slip BC was enough to fit the data, removing the false impression of a slippage process.

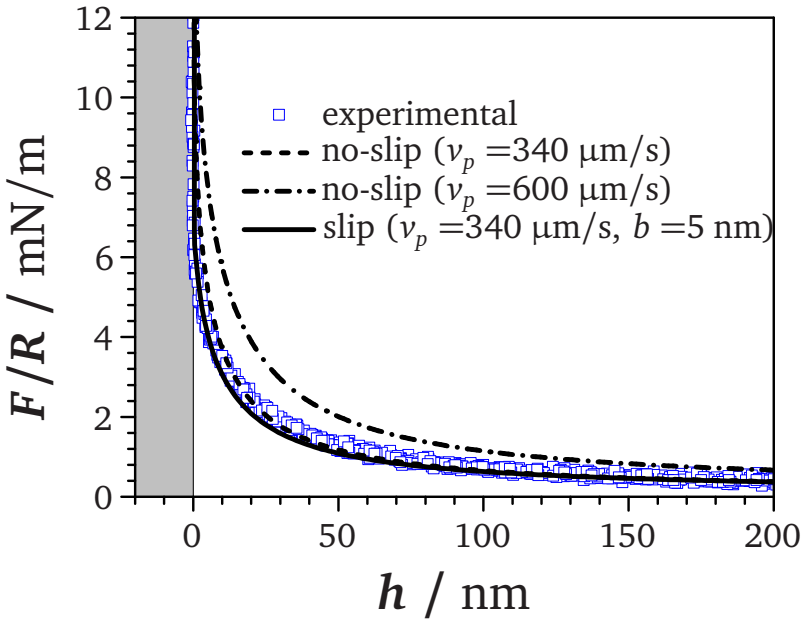

Fig. 3.8.: Approach F-D curves for a stiff ($k = 3.7$ N/m), rectangular cantilever against a SiO_2 surface driven at the maximum speed of the instrument ($v_p = 340$ μm/s). If the v_p is set to be the nominal value of 600 μm/s, slippage is obtained. A curve showing how a curve with $b = 5$ nm at a speed of 340 μm/s is shown for comparison.

Errors coming from nonlinearities of the piezo scanner are not always trivial to access. In the case of data shown in Fig. 3.8, the procedure to prevent errors associated with piezo scanner was followed: checking the raw data of the sensor measuring the piezo scanner displacement over time. According to the Veeco software (Nanoscope version 7.2), the measured speed was close to the set value, around 596 μm/s, value obtained as well if the data was exported, and the calculations performed in a third-part software. Using an alternative way for exporting the data, it was observed that the software itself was using the wrong dataset for the time series, leading to errors in speeds above 300 μm/s. However, the

effect on other experiments was different, showing sometimes the same error, sometimes a smaller one. This issue is apparently a bug in the software, related to real-time data acquisition. To use more reliable time measurements, extra independent processors are needed to ensure that processing time requirements are met, avoiding errors [143].

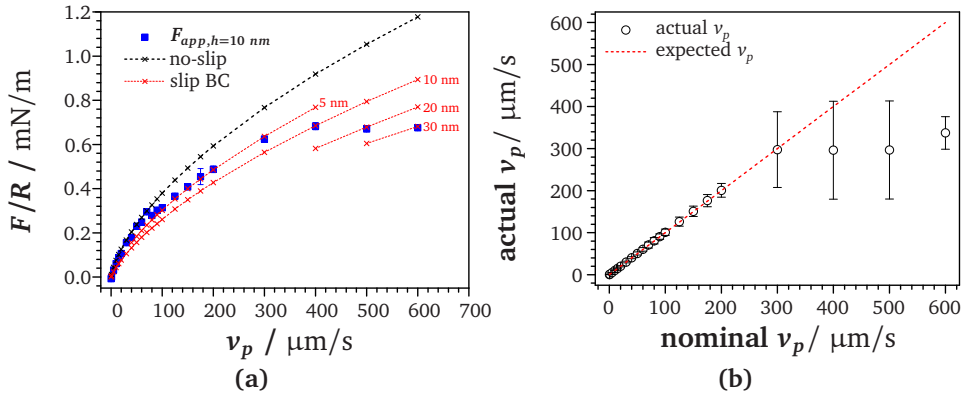

Fig. 3.9.: F/R at $h = 10$ nm for a soft ($k = 0.04$ N/m), rectangular cantilever against a SiO_2 surface driven at different v_p.

Data at $h = 10$ nm for a soft cantilever ($k = 0.04$ N/m) driven at piezo-scanner speeds v_p in a range of nominal values between 0.2 μm/s and 600 μm/s are shown in Fig. 3.9a. For $v_p > 80$ μm/s, the data needs a larger slip length to be fitted. The value of $b = 5$ nm is constant until $v_p > 300$ μm/s, after which the slip length increases as a function of v_p. Because only data at a single distance are presented, care should be taken in relating the slip lengths to results shown before, because a single slip length was frequently not sufficient to fit a F-D curve. This simplification was employed only for visualization, but the effect is present when analyzing the full F-D curve.

Fig. 3.9b shows the actual v_p from the piezo scanner compared to the nominal set value. The results obtained at $v_p = 300$ μm/s can be attributed to the error on v_p determination. The graph shows that at this run the maximum speed that the instrument could handle was around 300 μm/s, which gave the impression of an apparent slippage as in Fig. 3.8. However, for $v_p < 200$ μm/s, the instrument behaved without flaws, moving the piezo scanner at the set speeds. Nevertheless, Fig. 3.9a shows that in this range, slip lengths are

different for higher v_p, indicating that an additional process is causing a discrepancy in the results as a function of v_p.

Previously reported studies could have suffered similar issues related not only to non-linearities in the displacement of the piezo scanner [144], but also to time related issues, giving rise to a slip-dependent artifact [24, 40], similar to the results shown here. This apparent speed dependent slip corroborates with experiments done earlier [24, 40]. In those publications, a stiffer cantilever ($k = 0.1$ N/m) was used, but the viscosities were as high as 90 mPa$\cdot$s. These experiments were performed using computers with less processing power, which could have led to artifacts similar to these just described.

3.1.4.2. Piezo Scanner Effects on Retract Curves

Here, v_p is assumed constant(Eq. 1.20) and deviations from the absolute value of the piezo-scanner speed limit its application. In the previous subsection it was discussed the effects of artifacts of the piezo scanner on approach curves. Despite problems at speeds higher than 200 μm/s, on the range of values usually employed in CPT measurements ($v_p < 100$ μm/s), the piezo scanner has been displaced at constant v_p. For the retract curves the same behavior has been observed.

The retract process presents a small difference. On approach, the piezo scanner is resting, and is accelerated to reach the set v_p. When the piezo scanner retracts, it has to change the direction in a shorter period, experiencing a larger acceleration than during approach (Fig. 3.10). In this figure, the piezo-scanner speed (v_p, black curves) as a function of time is shown for two different cantilevers driven at 55 μm/s. Fig. 3.10a contains the data for a stiff cantilever (k=0.26 N/m), whereas Fig. 3.10b shows the data for a soft (k=0.06 N/m) cantilever. The v_p is constant for the approach part of both curves (left side) but not in the retract part (right side). Superposed to both graphs are the correspondent raw deflection Δz data (red curves), in arbitrary units, to illustrate which v_p matches part of the F-D curve.

The observed difference in the retract curve might cause discordance in its analysis, be-

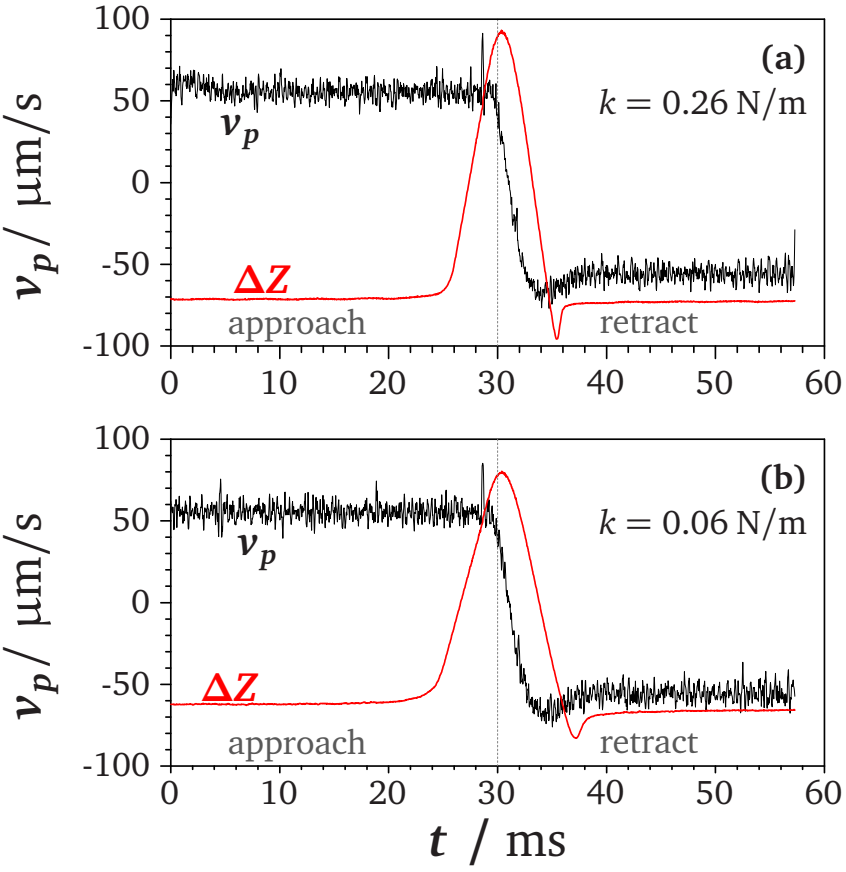

Fig. 3.10.: Piezo scanner driving speed v_p (black curves) as a function of time for a stiff cantilever ($k = 0.26$ N/m, (a)) and a soft cantilever ($k = 0.06$ N/m, (b)). As a reference, the raw deflection Δz is superposed to the speed data (red curves). In both cases the speed is constant for approach but it is not for retract.

cause it occurs near the range where the contribution due to surface and hydrodynamic forces is important. The mathematical modeling used in the literature and in this work (Eq. 1.20) assumes a constant piezo-scanner speed v_p. The variations shown here for the PicoForce module are among the smallest of the instruments available, and the effect of varying v_p has been studied before and known to affect force-measurement results[144]. Most of the difference occurs while the colloidal probe and the substrate are still in contact, and it does not affect the final result. In some cases (Fig. 3.10a), speed is still not constant during the minimum of the curve, showing a v_p 15% larger at that point. Analyzing a curve assuming that its speed is lower than the actual one may lead to an underestimation of an apparent slip length. This can be an alternative explanation for the variation seen in retract

curves and not in approach curves [25]. The magnitude should be small, causing errors in b estimation around 1 nm.

3.1.4.3. Effect of Piezo Scanner Driving Speed

The range of speeds of the piezo scanner v_p reported in the literature (Table 1.1) was between 4 to 100 μm/s, and the viscosities also varied considerably, from 0.89 mPa·s to 88 mPa·s. Inspecting Eq. (1.20), one observes that increasing v_p, or η, the force on the particle is increased, hence increasing the deflection of the cantilever. Large deflections may lead to artifacts caused by photodetector being used outside its linear range [26, 116]. Following the same trend, the drag on the cantilever is also affected by these two variables.

Averaged F/R values at $h = 10$ nm are shown in Fig. 3.11 for two cantilevers driven at different speeds of the piezo scanner v_p. Each of the points corresponds to the average of the 25 F-D curves acquired for a certain speed. The range of speeds spans until 300 μm/s, after which the artifacts described in Section 3.1.4 affect the result. The speeds reported in the abscissa have been measured from the raw displacement data, as describe in Section 3.1.4.1. There is no analytical expression for the relationship between force and v_p, therefore curves were simulated using the same parameters as the experimental curves for each speed and the value at $h = 10$ nm was plotted for comparison. The simulation curves are not comparable between different cantilevers; for each experimental point, a no-slip BC and a slip BC curve is provided for reference.

For the stiff cantilever ($k = 0.33$ N/m), the no-slip BC is valid to explain the experimental results for the whole range, with little deviation. This is not the case for the soft ($k = 0.04$ N/m) cantilever, in which even after the corrections, such as cantilever drag, and the care taken with artifacts deriving from the equipment, still presents small variance in slip length, increasing after around 80 μm/s. The change is small, and close to the deviation of the measurements.

Fig. 3.12 shows the results similar to those in Fig. 3.11 for speeds up to 100 μm/s, but the experiments were performed in a viscous sucrose solution (40% sucrose in wa-

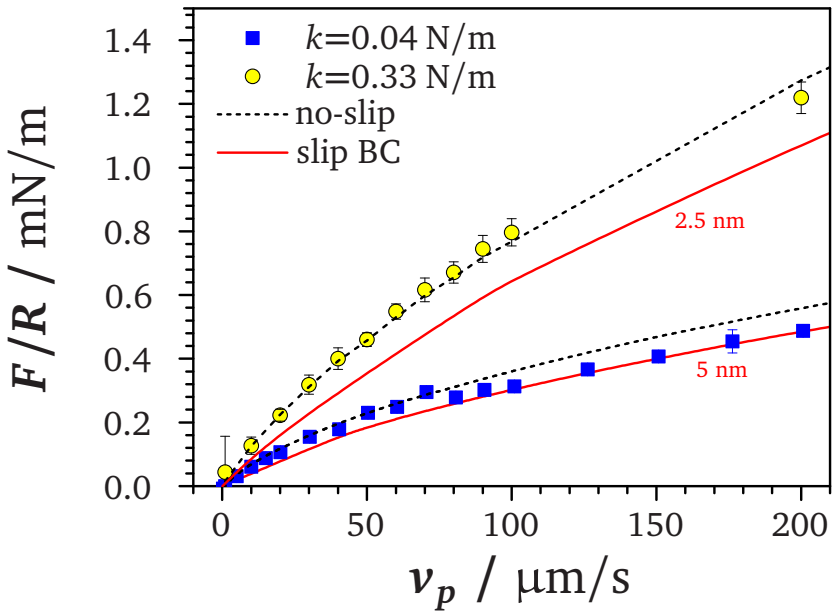

Fig. 3.11.: F/R at $h = 10\,\text{nm}$ for two rectangular cantilevers at different v_p: a stiff ($k = 0.33\,\text{N/m}$, blue squares) and a soft cantilever ($k = 0.04\,\text{N/m}$, yellow circles). For each of the cantilevers, simulations using the no-slip BC (black, dashed line) and slip BC (red, continuous line) were performed. The value of the simulated curves at $h = 10\,\text{nm}$ is plotted for comparison with the experimental data. While for the stiff cantilever the no-slip BC is valid for all speeds, for the soft cantilever there is a deviation leading to an apparent slippage.

ter, $\eta = 6\,\text{mPa}\cdot\text{s}$) for the same soft cantilever ($k = 0.04\,\text{N/m}$) as above. The slip length needed to explain the results here was higher, around 10 nm, and despite correction, it is possible that there is still some residual value coming from a speed-dependent artifact. An alternative explanation for a higher slip length on a sucrose solution is that a depletion layer may form on the surface, which leads to a zone where the viscosity is lower, giving an apparent slip [116].

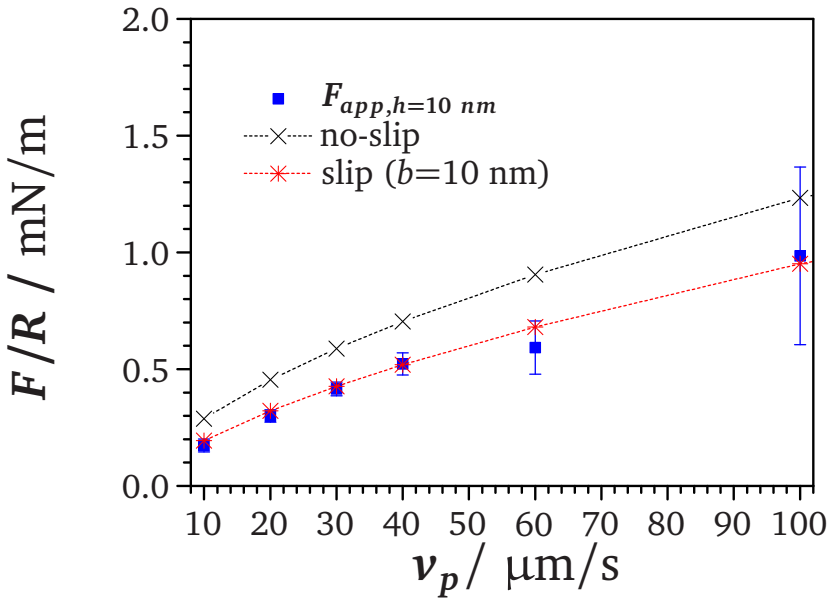

Fig. 3.12.: F/R at $h = 10$ nm for a soft ($k = 0.04$ N/m), rectangular cantilever against a SiO_2 surface driven at different v_p on a sucrose solution ($\eta = 6$ mPa·s).

3.1.4.4. Relative Speeds of the Particle for Different k

Comparing force curves acquired using cantilevers with different spring constants is difficult because of the different sphere velocity dh/dt approaching the substrate. Fig. 3.13 shows a plot of the relative velocity $(v_p - v_{sph})/v_{sph}$ of the free end of the cantilever (where the microsphere is attached) with respect to the cantilever base versus the distance of the microsphere from the surface. The curves were calculated with $\eta = 0.89$ mPa·s, $v_p = 40$ µm/s, $R = 10$ µm, and assuming a no-slip BC. If $k = 5$ N/m, the velocity of the colloidal probe is nearly constant over the entire approach distance, dropping to $0.9v_p$ at a distance of 10 nm from the surface (curve a). At the same distance from the surface, the v_p drops considerably proportionally to k (Fig. 3.13), reaching only $0.36v_p$ for $k = 0.05$ N/m (curve c).

The velocity of the microsphere is thus far from being constant over the entire approach distance and is different for different cantilevers. If viscosity or v_p are increased, as in the extreme cases presented in literature, the velocity of the colloidal probe is even lower. For instance, using $\eta = 6$ mPa·s and $v_p = 600$ µm/s for a cantilever with $k = 0.05$ N/m leads

the relative velocity to drop to approximately 0.5 already at $h = 200$ nm (Fig. 3.13). A reduced velocity causes also a reduced drag on the cantilever, consequently reducing the drainage force considerably.

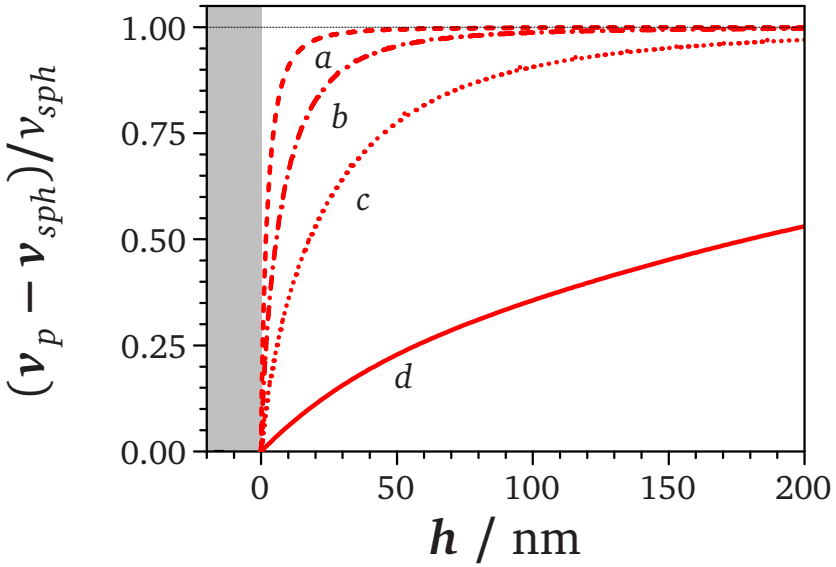

Fig. 3.13.: Relative velocity of the colloidal probe versus distance calculated using the no-slip BC. The dash-dotted curves simulate experiments done with $\eta = 0.89$ mPa·s, $v_p = 40$ µm/s and $R = 10$ µm for different k: (a) $k = 5$ N/m; (b) $k = 0.5$ N/m; and (c) $k = 0.05$ N/m. The solid line (d) is calculated for $\eta = 6$ mPa·s, $v_p = 600$ µm/s, $R = 10$ µm and $k = 0.05$ N/m.

The change in relative speed means also that the shear rate in those experiments are not the same. The shear rate for the geometry used in CPT measurements is proportional to the velocity of the sphere [20], leading it to be also dependent on the stiffness of the cantilever. Shear rate also changes in z (distance from the surface), and in xy positions (distance from the contact point of the sphere) [117], which complicates the interpretation of the results. To illustrate this effect, it is easier to calculate the maximum shear rate at the plane surface, given by Eq. 3.1 [20]:

$$\dot{\gamma}_{MAX} = \left|\frac{\partial v_T}{\partial z}\right|_{MAX} = \frac{1}{2}\left(\frac{3}{2}\right)^{5/2} \frac{R^{1/2}}{h^{3/2}} \frac{dh}{dt} \tag{3.1}$$

The result of the calculations using the simulations from Fig. 3.13 shows that the difference starts to be relevant for distances smaller than 100 nm (Fig. 3.14) when working with

a fluid of $\eta = 0.89$ mPa·s. The difference in the maximum applied shear rate between one cantilever with $k = 0.05$ N/m and other with $k = 5$ N/m spans one order of magnitude. The differences are even more pronounced for the case with $v_p = 600$ µm/s and $\eta = 6$ mPa·s, where before $h = 100$ nm they are considerable. The aqueous solutions used here, as Newtonian liquids, are not supposed to present shear-rate dependent behavior. However, in liquids where a shear rate-dependent process is expected, it would complicate even more the data interpretation and comparison. For that, this k-dependence should be considered in future high-speed force measurements. Results dependent on shear rate measured by CPT are also not expected to be explained by a simple model of a shear rate-independent slip such as the Navier slip BC [108].

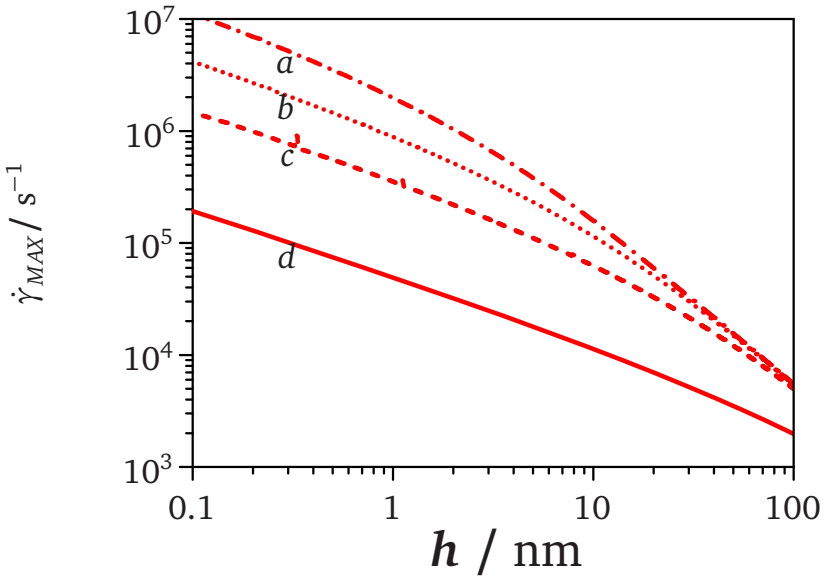

Fig. 3.14.: Maximum shear rate at the surface (Eq. 3.1) calculated from the simulated curves of Fig. 3.13. Curves (a), (b), (c), and (d) correspond to the same values already described in Fig. 3.13.

3.1.5. Drag on the Cantilever

The drag force on the cantilever F_{clv} is a large part of the total cantilever deflection for high speeds or high viscosities. Since an increase of both these variables can lead to differences in measure slip length, F_{clv} is a potential source of the discrepancy discussed before.

In some of the previous studies, although F_{clv} varies as a function of separation because of cantilever deflection, it was simplified as a constant force, independent of particle-surface separation [21–24, 64]. In this work the drag on the cantilever is considered a variable force, according to Eq. 1.16 (Section 1.5.2.2).

Previous studies have shown that a small error occurs when the drag is assumed as constant [26, 104, 117, 145]. Nevertheless, it has been recently suggested that the discrepant results between soft and stiff cantilevers could stem from the variable drag being ignored [115, 141]. In this work, the difference between the slip lengths obtained when simulating them with a constant drag and the ones calculated using Eq. 1.16 was small, as reported by other groups.

To give a general overview on the effect caused by the variable drag, in Fig. 3.15 are compared simulated curves in two different situations. The first calculates which is the relative difference between a curve simulated assuming the no-slip BC and other assuming a slip length of 5 nm; The second plots the relative difference between curves assuming the no-slip BC, but one using a constant F_{clv} and the other a variable F_{clv} according Eq. 1.16. These two cases are compared for different k, v_p, and η.

Assuming that the experimental F-D curves need $b = 5$ nm to be explained, it would mean that the forces are between 10% to 60% lower than expected, dependent on k and the distance from the surface (Fig. 3.15a). If the drag on the cantilever is assumed to be variable and described by Eq. 1.16, the maximum observed difference is around 7% (Fig. 3.15b). This means that the error of assuming the cantilever drag as constant is indeed small and could account for only a small part of the measured slip length. Comparing both graphs it is also seen that the effect of neglecting the variable drag is relatively more pronounced in stiffer cantilevers than in the soft ones, an inverse trend that the one observed when slippage is taking place. The small difference caused by taking the variable drag into account is already reflected on previous results [115, 141], in which the measured b was smaller when using the variable drag term, but it was still needed to employ a slip BC to explain the results.

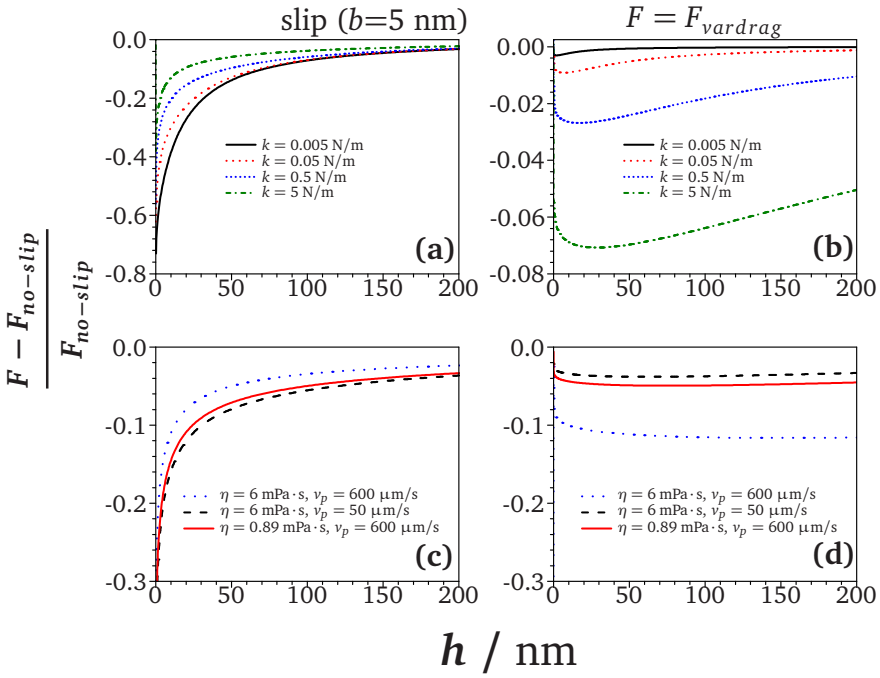

Fig. 3.15.: Differences caused by neglecting that F_{clv} is variable (right column), and by assuming an apparent slippage (left column) for different k, v_p, and η: (a) Relative difference between assuming b=5 nm and a no-slip BC curve for four values of k; (b) Relative differences for the same cantilevers as in case (a), but now assuming that instead of slippage, there is a variable drag force: the range of the graph is equivalent to 10% of graph (a); (c) Keeping $k = 0.05$ N/m, observing the deviations caused by v_p and η when slippage is compared to the no-slip BC curve; (d) Graph equivalent to (c), but now inspecting the effect of variable drag.

A similar comparison for different viscosities and driving speeds is shown in Fig. 3.15 for the same $k = 0.05$ N/m (graphs c and d) showing the same trend. By the data from these graphs is possible to infer that a F-D curve exhibiting slippage with b=5 nm cannot be explained solely by a variable drag as described in Eq. 1.16. Nevertheless, ignoring that it varies as a function of separation does increase the value of the apparent slip length obtained as reported previously [115, 141].

3.1.5.1. Drag Coefficient for Rectangular Cantilevers

The works published dealing with cantilever drag always rely on the experimental determination of the cantilever drag coefficient to perform the calculations [104, 109, 110, 112–

114, 116–118, 121]. Here also the drag on the cantilever was matched by a constant for each experiment. If a drag coefficient for the cantilever had been known, it would have allowed the simulation of a F-D curve without an extra experimental parameter to be determined for a specific cantilever.

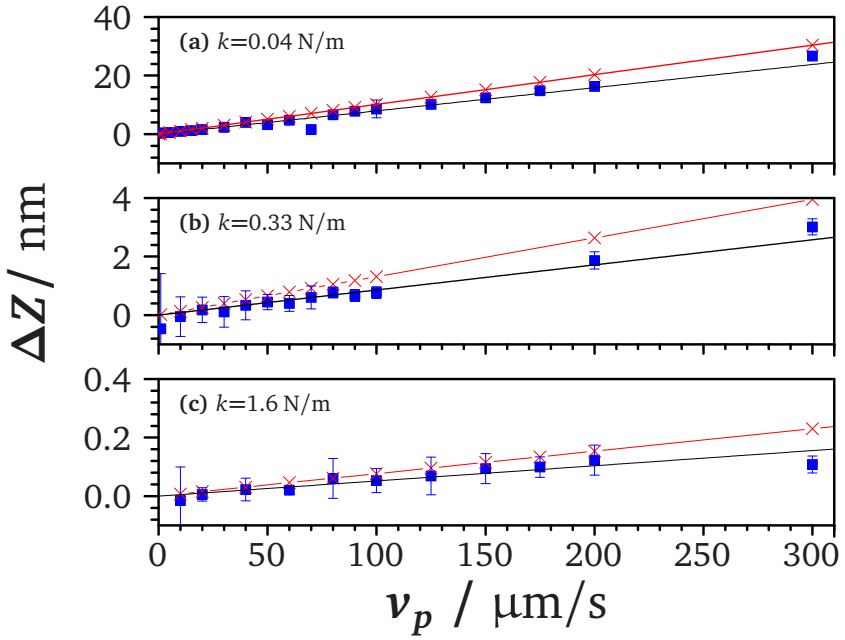

Fig. 3.16.: Deflection on approach curves for $h = 3$ µm (blue squares) as a function of v_p, for three cantilevers of different stiffness in water. The continuous black line is a linear fit $\Delta z = C_d \cdot v_p$ crossing the origin. The red line with crosses represent calculated values using Eq. 3.3.

The deflection of the cantilever caused by hydrodynamic drag on the cantilever was linear as a function of v_p (Fig. 3.16). The deflection Δz_{away} was recorded at $h = 3$ µm. At this distance the drag on the sphere is considered small and negligible, and the differences between z_{app} and z_{ret} are related solely to F_{clv}. Soft and stiff cantilevers were used, and v_p was varied from 0.1 µm/s to 300 µm/s. The deflection curves can be fitted by linear equation of the form $\Delta z = C_d \cdot v_p$, showing that the cantilever drag can be treated as a force with a drag coefficient independent of speed.

The cantilever can be approximated as a cylinder [111], as it is commonly used in cantilever vibrations studies ([129]). The hydrodynamic drag force cause by a laminar flow past a cylinder can be represented as [146]:

$$F_{cylinder} = \frac{4\pi\eta L v_p}{\ln\left(\frac{L}{w} + 0.5\right)} \tag{3.2}$$

Far away from the surface, the van der Waals and electrostatic forces acting on the sphere can be ignored. The hydrodynamic force acting on the sphere is not affected by the surface, and can be neglected. In addition, the calibration of the cantilever is performed assuming a concentrated end-load on the cantilever, while the hydrodynamic drag on the cantilever is a distributed load. Taking that into account, and that the optical lever method used in most commercial AFM instruments measures the inclination of the cantilever rather than its deflection, the force measured is in fact overestimated by a factor of 3 [147]. The deflection of the cantilever far away from the surface can then be approximated as:

$$\Delta Z = 3\frac{4\pi\eta L v_p}{k\ln\left(\frac{L}{w} + 0.5\right)} \tag{3.3}$$

In Fig. 3.16 is also shown the force calculated according to Eq. 3.3, where the cantilever is treated as a cylinder. For lower speeds the agreement is better, but in general the model is valid only as a rough approximation. It can be seen on Table 3.1 that the fit coefficients corrected by the respective k are in the same order of magnitude, with the values for the 0.04 N/m-cantilever being close to that obtained for the cantilever with $k = 0.33$ N/m. The value was considerably lower for the stiffer ($k = 1.6$ N/m) cantilever, which can be attributed to the higher error caused by the smaller deflections of the stiffer cantilever. The cantilever can be approximated as a cylinder for low deflections, diverging from the data for higher deflections.

	k / Nm^{-1}	$k \cdot C_d$/μNm^{-1}s^{-1}
1	0.04	31.7 ± 0.2
2	0.33	28.3 ± 1.2
3	1.6	8.3 ± 0.7

Table 3.1.: Coefficients C_d from the equation $\Delta z = C_d \cdot v_p$ used to fit the data shown in Fig. 3.16

3.1.6. Linearity of Cantilever Deflection

3.1.6.1. Linearity of the Optical Position Detector

The linearity of the photodetector from the Multimode Picoforce AFM was tested before proceeding with the F-D measurements. It has been shown that, during a drainage measurement, the laser reflected from the cantilever might hit an area of the photodetector where the response is not linearly related with the deflection of the cantilever [116]. This could cause an error in the magnitude of measured deflections because all data transformation assumes a linear behavior (Section 2.2.3.1). A more sensitive test of the detector linearity can be made using a cantilever, as shown in the next subsection. However, a separate measured was performed, to ensure that the photodetector had a linear response independently of the behavior of the cantilever.

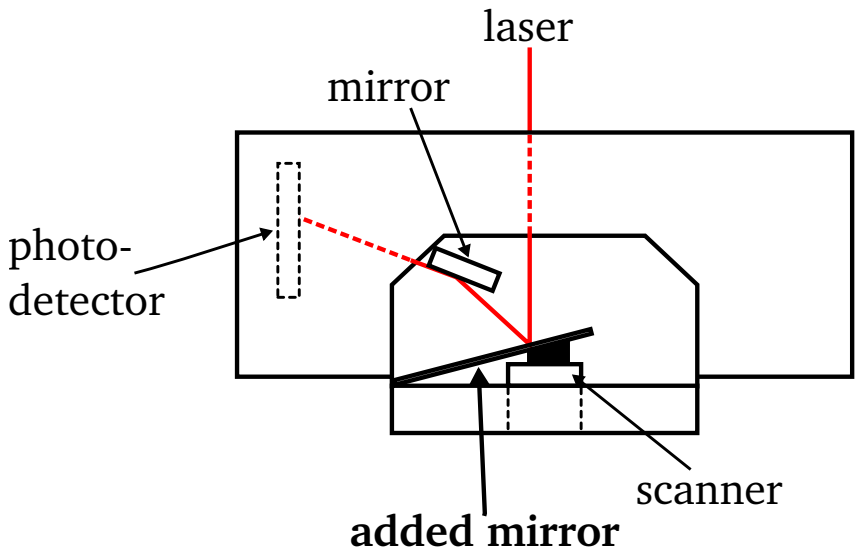

Fig. 3.17.: Schematics of the measurement of the photodetector linearity. A mirror was placed inside the measurement head of the Multimode Picoforce, supported on the scanner.

A mirror was placed in the microscope head so that one end was placed at one inferior, inside corner of the head and the other end was positioned on top of the piezo scanner (Fig. 3.17). The piezo scanner was moved in a series of intervals, measuring the signal of the detector as function of change in the inclination of the mirror. The obtained curves

are shown in Fig. 3.18, with curves for all detector range. Each curve spans for 3 V and apart from the curves on the extremes, they are reasonably linear and independent of the starting position of the laser on the photodetector. Averaging the curves from Fig. 3.18 excluding the extremes and fitting the average with a linear function on the center part of the curve lead to a good agreement with the linear equation. The residuals of this fit are shown in Fig. 3.19, and the disagreement with a linear curve is not bigger than 60 mV. In a range of 1 V the residuals remained within a limit of ± 5 mV. This region is where the fit procedure for curve conversion is normally performed. All deflections measured on this work are within this limit.

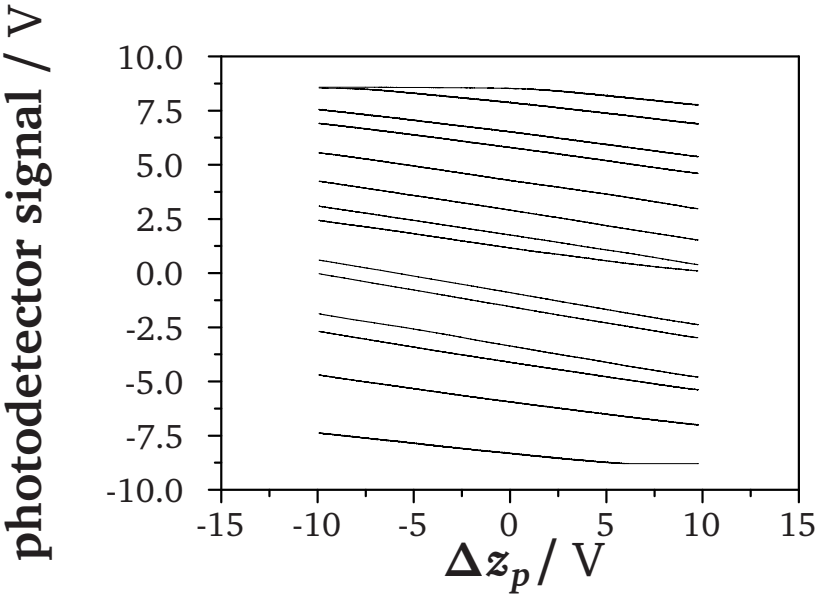

Fig. 3.18.: Linearity of the photodetector from the Veeco Multimode AFM in the range between −7.5 V and 7.5 V.

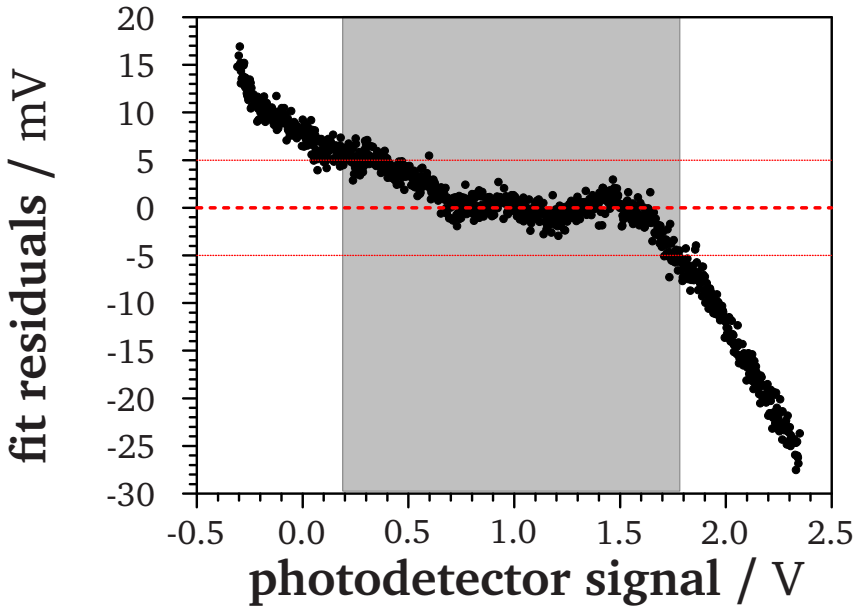

Fig. 3.19.: Residuals from a linear fitting over the marked gray area for an average of the curves from Fig. 3.18 in the range between −7.5 V and 7.5 V.

3.1.6.2. Linearity of Constant Compliance Region as a Function of Piezo Speed

Fitting residuals after a linear fit over the constant compliance region (CCR) were calculated for four different curves driven at $v_p = 0.2$ µm/s, $v_p = 50$ µm/s, $v_p = 100$ µm/s, and $v_p = 200$ µm/s (Fig. 3.20). All four graphs show a set of points obtained from the fit of 25 raw F-D curves, represented with gray symbols, and a single, arbitrary curve is highlighted from the set, in red circles. The abscissa shows the photodetector signal, in volts, and the ordinate axis represents the displacement of the piezo scanner, which can be assumed as the cantilever deflection because the substrate is not deformable.

The graph of residuals shows no trends in the first three cases and with a random noise with magnitude of ±2 nm. The higher the speed, the lower the range of the detector that could be probed, for example at $v_p = 50$ µm/s the curve goes only until close to 0 V. This difference of size to the previous curve is due to the magnitude of the hydrodynamic repulsion on the sphere, producing a larger signal for higher speeds. The cantilever used here is the same shown in Fig. 3.9.

The curve is linear between −5 V and 10 V for the experiment at $v_p = 0.2$ µm/s. These

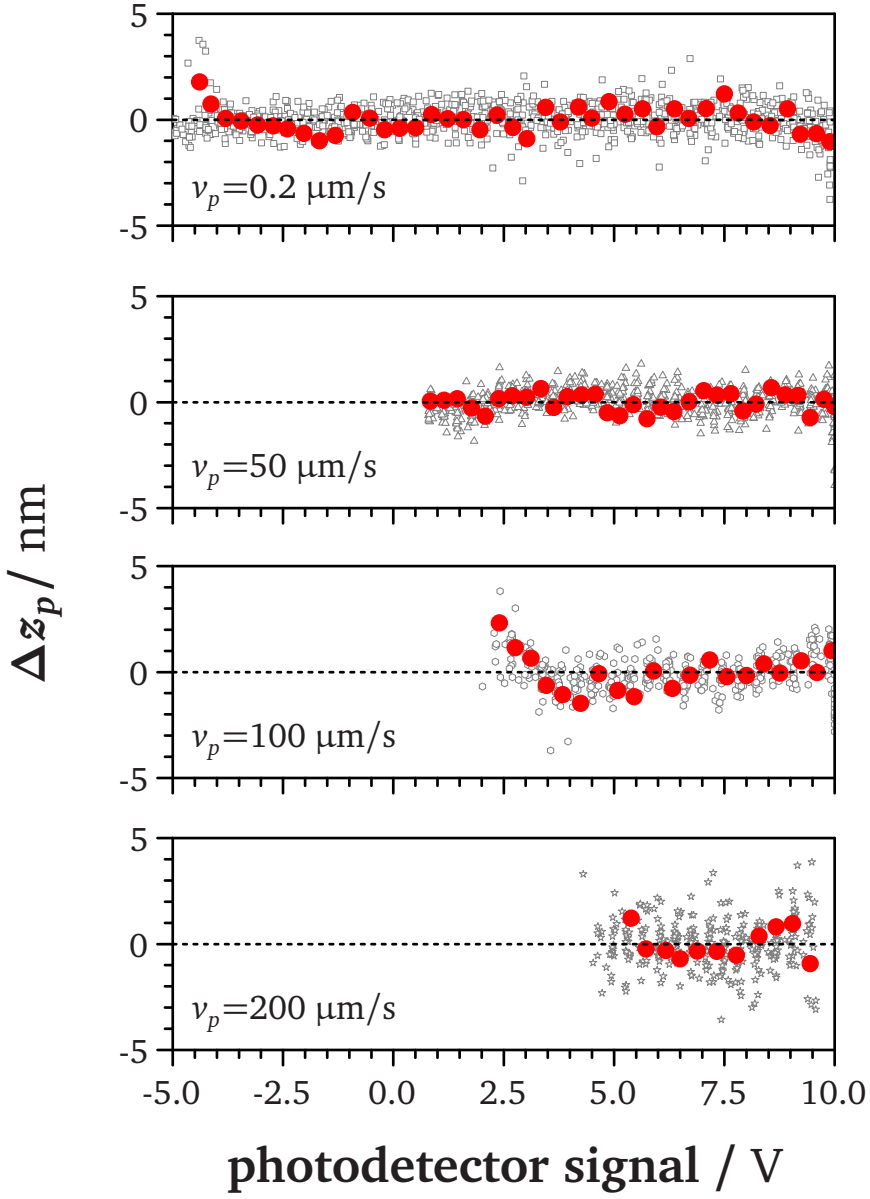

Fig. 3.20.: Comparison between the residuals of a linear fit of the constant compliance region from approach curves for a soft cantilever ($k = 0.04$ N/m) at four different v_p. One of the curves was chosen arbitrarily and highlighted as red dots.

data corroborates with the test described in Section 3.1.6.1, showing that both detector and cantilever are used within their linear regions on these experiments. When driven at $v_p = 50$ μm/s (Fig. 3.20) the cantilever deflected linearly on the range of the CCR. This speed is close to the values employed for experiments shown in Section 3.1.2, and shows that the slip observed there cannot be attributed to a non-linear detector. It shows also that

a soft cantilever can deflect linearly in the ranges used in this work, and despite that, can still result on lower forces than expected and show an apparent slippage.

At $v_p = 100\ \mu m/s$ a non-linearity is present around 3 V, arising from a residue of the part of the curve before contact is achieved. Besides that, the curve is similar to the other previous two curves. A drawback that arises is that the range of curve that is linear is considerably smaller, with fewer points than on the other cases. At $v_p = 200\ \mu m/s$ this effect is even more pronounced, where only 11 points are left for fitting the curve. At this speed it is also possible to see that the cantilever deflection is not linear, though the pattern can arise only because of the small number of points.

A point made against the use of softer cantilever is that the measured deflection would lie outside the linear range of the detector because of its higher sensitivity [116]. The argument presented there was based on a graph of fitting residuals where the constant compliance region (CCR) is not linear. In the same article, an extreme case is presented, where the signal is large enough to saturate the photodetector output. The data in Fig. 3.20 refutes the universality of this argument. Their experiments were performed on a more than 100 times more viscous liquid than here ($\eta = 100$ mPas), leading to a much higher force and deflection even for a stiffer cantilever. Another factor is that they have used a different instrument, which could have a sensor with a lower range of linearity. It is more feasible that speed-dependent slip lengths presented on the literature were originated in artifacts of the piezo scanner than because of a non-linear signal. However, it cannot be completely discarded that the cantilevers might be deflecting non-linearly, because off-axis placement of the particle leads to twisting of the cantilever, an effect which has not been studied and may have a contribution to the smaller forces observed.

3.1.7. Cantilever Shape

In Sections 3.1.1 and 3.1.2 the results for rectangular cantilevers were discussed. It was shown, that depending on the magnitude of k, an apparent slippage has been observed

in CPT measurements. Rectangular cantilevers were chosen for their higher mechanical stability and less difficult hydrodynamic modeling. However, several experiments on hydrodynamics drainage were performed with V-shaped cantilevers. This type of cantilevers was preferred in the past because they were supposed to be more stable with respect to lateral and torsional twists [148], which later has been shown to be wrong [149, 150].

In order to check whether the cantilever shape had any relation with the observed slip lengths, two drainage experiments were performed using two different V-shaped cantilevers, one with $k = 0.06\,\mathrm{N/m}$ (Fig. 3.21a) and other with $k = 0.36\,\mathrm{N/m}$ (Fig. 3.21b). Force curves obtained with the softer, V-shaped cantilever (type 14, Table 2.1, $R = 8\,\mu\mathrm{m}$) could only be fitted assuming a slip length $b = 5$ nm. The curves obtained with the stiffer cantilever (type 15, Table 2.1, $R = 10\,\mu\mathrm{m}$) show a good agreement with the no-slip BC. The trend for V-shaped cantilevers is similar to that observed for rectangular cantilevers of equivalent stiffnesses (Fig. 3.4 and Fig. 3.1): softer cantilevers show lower deflections than expected for the no-slip case, and stiffer cantilevers are explained by assuming the no-slip BC.

V-shaped cantilevers have been suggested as the reason for the appearance of slippage in some CPT experiments [123]. An inspection on Table 1.1 show that before the publication of the article with that argument, data using rectangular cantilevers and presenting an apparent slippage were already available. The authors have restricted, however, their analysis to a subset of the results present on Table 1.1, a reasonable measure because of the number of experimental differences between groups. Observing the results shown here, this argument is not valid to explain the discrepancies observed in the literature. Although the shape may affect the value of slip length used, it is not the factor leading to the discrepancies observed in the literature.

Indeed, a slightly larger slip length of 15 nm to F-D curve acquired with rectangular cantilevers of similar stiffness had to be used (Fig. 3.4), showing that in this case the rectangular cantilever yield a bigger slip length, not the V-shaped. This small discrepancy between the force measured with the V-shaped and the rectangular cantilevers, although having

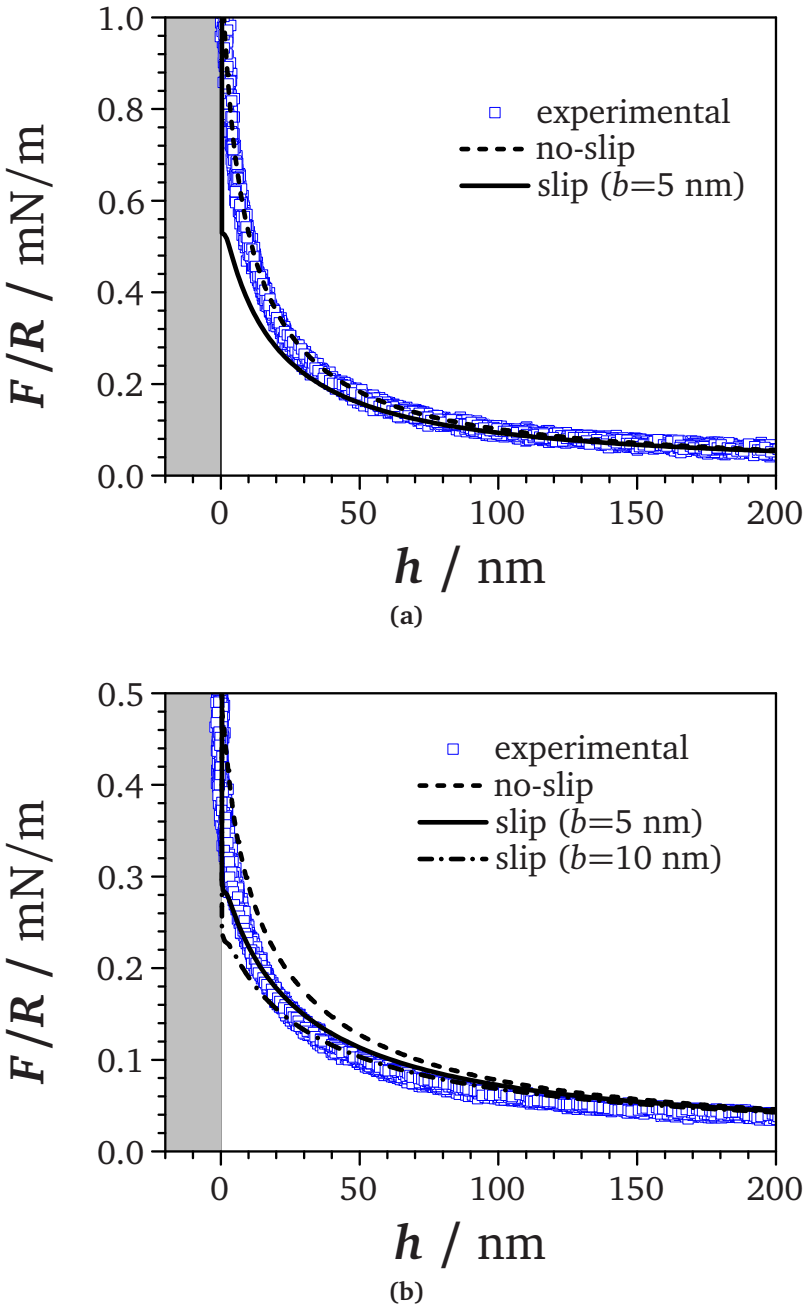

Fig. 3.21.: F-D curves for V-shaped cantilevers with different spring constants at the same speed: (a) $k = 0.32$ N/m and (b) $k = 0.056$ N/m.

similar k, could be attributed to their different lengths (Table 2.1), because the rectangular cantilever is 1.5 times longer than the V-shaped one. The difference is still too small to confirm this, because of other factors contributing for an apparent slip, such as roughness. Also the drag on the cantilever can differ, because of the empty void between the V arms

of the cantilever. The drag may cause also twisting of the cantilevers if the arms are not totally symmetrical. Cantilever stiffening by twisting has been proposed as the cause for the difference between rectangular and V-shaped cantilevers [123], as rectangular cantilevers are less prone to twisting than V-shaped ones [149]. This hypothesis will be discussed later, when comparing all the results 3.1.10.

It could be speculated that by shortening the cantilever beyond a certain threshold one could obtain force curves that are fitted by a no-slip BC, helping to explain the contradiction between the results in this section and published results [123], because the threshold stiffness and length vary between rectangular and V-shaped cantilevers. It is possible that the shape of the cantilever affects the recorded hydrodynamic forces to some extent, but this can only be confirmed by further studies on the different drag coefficient.

3.1.8. Roughness Effects

3.1.8.1. Roughness on the Substrate

In this section the issue of roughness as a possible factor leading to the difference observed in F-D curve curves is discussed. A stiff rectangular cantilever ($k = 0.15$ N/m) was chosen to perform the experiments. Here it was decided to avoid the differences seen because of different spring constants by using the same probe to compare three different surfaces. Since no specific effect has been identified as the cause, it is safer to compare two different substrates with the same probe.

In Fig. 3.22 are shown F-D curves for the approach against a smooth SiO_2 surface and against a SiO_2 patterned surface with height of 4 nm (Fig. B.1, Appendix) at 50 μm/s. In this figure, the choice was to present the data with the abscissa in a logarithmic scale to emphasize the differences between the smooth and rough surface, otherwise they would appear superposed. Both experimental F-D curves have a small deviation from the curve simulated using the no-slip BC (dashed line). The slip length b needed for the smooth surface is smaller than 1 nm, what can be correlated to the sphere roughness (Fig. A.4a,

Appendix). The value of b needed for fitting the curve of the rough substrate was around 3.5 nm. This value lies in the same order of the Z_{PV} of the pattern.

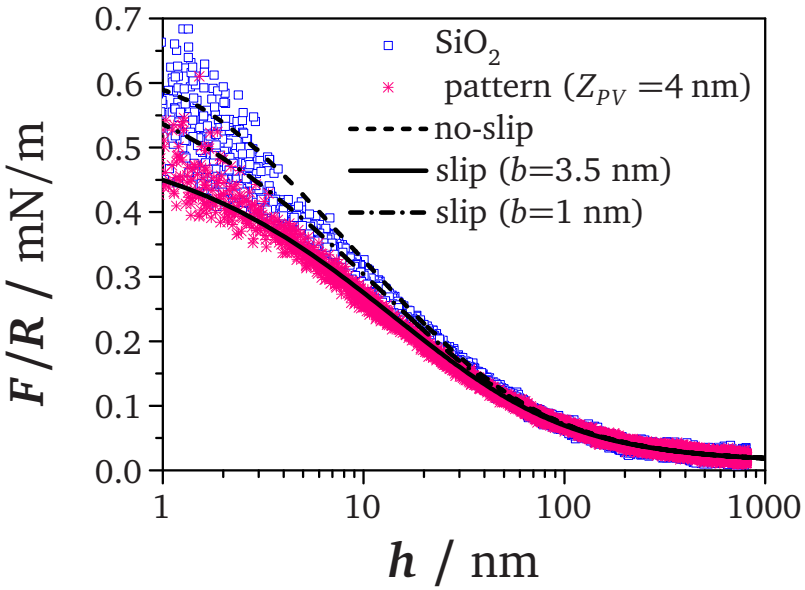

Fig. 3.22.: Comparison between F-D curves obtained against a patterned ($Z_{PV} = 4$ nm) substrate (pink crosses) and against a smooth SiO_2 surface (blue squares) using the same colloidal probe. The dashed line is a simulated curve assuming no-slip BC. Continuous line represent the curve assuming slip BC ($b = 3.5$ nm) and the dashed-dotted line assuming $b = 1$ nm. $v_p = 50$ μm/s, and $R = 9$ μm.

The results are consistent with the others shown so far, where F-D curves for a stiff cantilever run at v_p around 50 μm/s are in agreement with the no-slip BC. The roughness of the surface plays a role shifting the contact point of the tip, but no significant additional slip is observed. This makes valid the assumption made before of subtracting the roughness value from the measured slip length. This substrate is, though, a patterned surface where the surface profile is known; for a real random surface this subtraction is more difficult, because the pressure relief for every protuberance should be calculated [27]. The effect has been calculated for a single asperity, and for a surface with random roughness each protuberance is expected to influence the behavior of its closest neighbors. Previous results have also shown that a small random roughness may affect more the liquid flow than a pattern [118].

The effect of roughness on slippage of liquids is a matter of debate. Some researchers

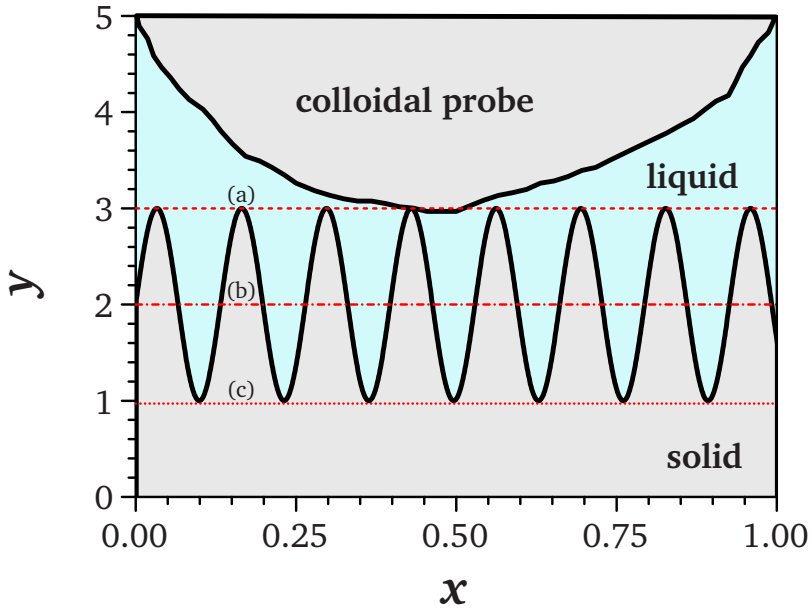

Fig. 3.23.: Illustration of the three possible theoretical positions for setting an equivalent surface for experiments with rough surfaces.

found that slippage increases with surface roughness, whereas others found that it decreases. This discrepancy may arise from the use of the equations meant for smooth surfaces, what is not strictly correct. As an approximation, it has been postulated that the no-slip BC can be assumed if the equivalent surface is set at an arbitrary intermediary position inside the channels [27, 60–62]. Fig. 3.23 shows a sketch illustrating the possibilities for the location of the arbitrary equivalent surface used before in the literature. In a recent work [151], the values for a random roughness surface agreed with a value of $h_{avg}/2$ (line (b) on Fig. 3.23). Prior work used different convention, some using equivalent surface at the valleys [39] (line (c) on Fig. 3.23) and others defining it at the top of the patterns [64] (line (a) on Fig. 3.23). The choice for the position of the equivalent surface is influenced by the technique used for performing the experiments: The former case [39] corresponds to a flow measurement, while the later [64] was performed with the CPT, where the equivalent surface is normally defined as the contact position of the sphere, as sketched as a circle in Fig. 3.23.

In Fig. 3.24 are presented results performed on patterned silicon surface (Fig. 3.24) with

higher peaks (45 nm) in Fig. 3.22. The patterns were positioned side by side in the same substrate, therefore the experimental conditions are the same as in previous graph, including the same colloidal probe. Increasing the height of the peaks the effect of roughness is emphasized, allowing the discussion of the theoretical position of the equivalent surface. Two graphs are presented in Fig. 3.24, one applying the slip BC (3.24a) and other assuming no-slip BC (3.24b) for different positions of the equivalent surface. In the first case (3.24a), a $b = 30$ nm is needed to explain the curve, although this simulation does not fit well the curves for h<20 nm. A better accordance can be obtained when a smaller slip length ($b = 10$ nm) is assumed and setting the equivalent surface to be at half of the height of the peaks (22.5 nm). In the second case (3.24b), it is observed that the assumption of the no-slip BC requires the equivalent surface to be set at 40 nm, value close to the height of the peaks.

These results are comparable to data published previously [118], where the same instrument and equivalent conditions as this work were used, but with a soft, V-shaped cantilever. There, a residual slip still persisted in the results even after the subtraction of the roughness. The trend is the same as observed for smooth surfaces, where soft cantilevers tend to present an additional slippage not seen when employing stiff cantilevers. The observed effect of roughness is not in accordance with the previous results where a slip $b = 10$ nm was needed for a final separation of $Z_{PV}/2$ [151]. They are, however, in accordance with previous data [27] were an arbitrary value of $0.89Z_{PV}$ had to be set. This difference can be attributed to the use of a random pattern [151], while here a pattern composed of channels was employed. The flow field as well can be complicated because of the spherical geometry of the partcle. This geometry directs the moving liquid in all directions, both aligned with the channels and against them, what adds complexity on how to describe the influence of patterns with channels investigated with CPT [152].

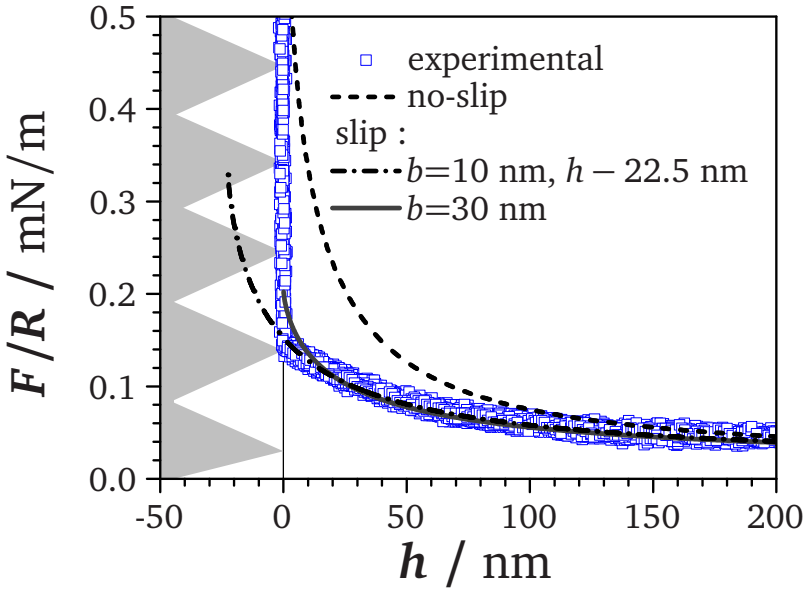

(a)

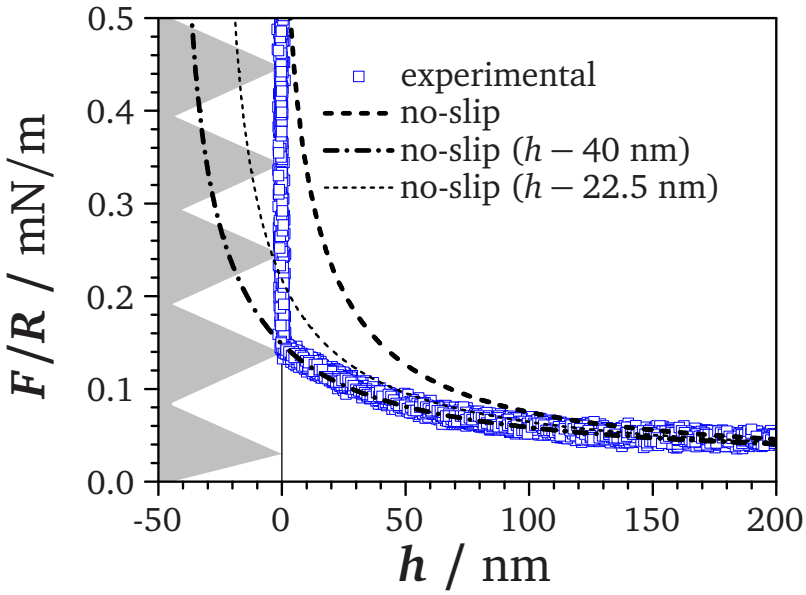

(b)

Fig. 3.24.: F-D curves obtained on patterned (Z_{PV} = 45 nm) substrate using the same cantilever as in Fig. 3.22. The dashed lines are the same calculated curves assuming no-slip BC shown in Fig. 3.22. (a) Continuous line represent the curves assuming b = 30 nm and dash-dotted line corresponding to a decreased b value of 10 nm and a shift of 22.5 nm in the distance axis. (b) No-slip BC curve shifted for two difference distances.

3.1.8.2. Roughness of the Sphere and Soft Cantilevers

A question that arises after the results of the previous section is whether the slip length seen in section 3.1.2 could be explained by the roughness of the particle. The surface of the particle used in the experiment shown in Fig. 3.4 presents a Z_{PV} value of 5.3 nm, smaller than the slip length needed to fit the curves (between 7 and 15 nm).

An alternative to the use of a slip length for fitting the data shown in Fig. 3.4 is to subtract an arbitrary value from the abscissa, as it was done in last section. The result can be seen in Fig. 3.25, where the no-slip BC curve had to be displaced by 18 nm to achieve a partial agreement. As before, this value is not realistic, because it is much bigger than the Z_{PV} of the particle. As with the slip, one can see that a single simulated curve cannot explain the data. Although the curve has a good agreement close to the surface when a value of 18 nm is subtracted from the abscissa, the values at around $h = 50$ nm are still not fitted. A second curve is shown where 25 nm have been subtracted, showing that at each position a different value in this range would be needed.

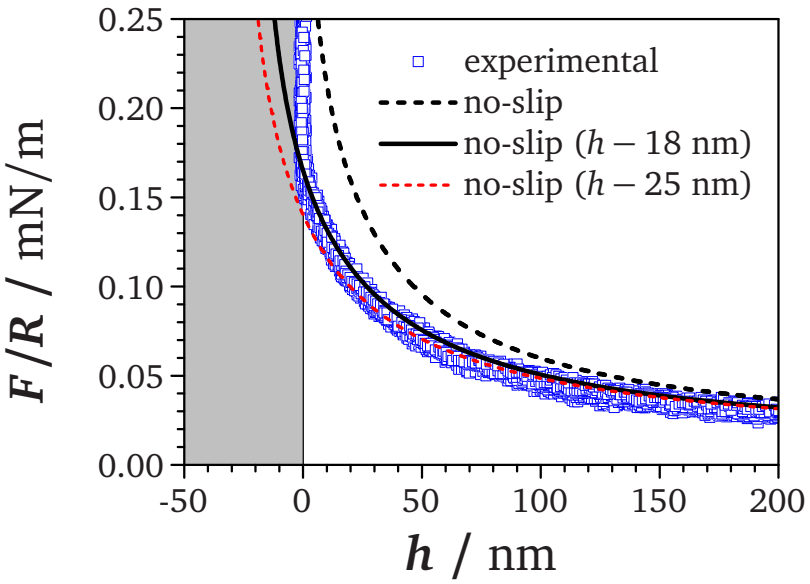

Fig. 3.25.: Approach F-D curves from Fig. 3.3 (blue squares, soft ($k = 0.04$ N/m, rectangular cantilever). The surface of glass sphere attached to the cantilever is shown in Fig. A.5. The black dashed line is a simulated curve assuming the no-slip BC. The other lines correspond to different values subtracted from the h axis of the no-slip BC curve: 18 nm (continuous line) and 25 nm (red, dashed line).

Guriyanova et al. [118] showed results for the case of soft cantilever with rough colloidal probes. The conclusion was that even taking into account the roughness of the particle, a residual slip still was observed, as seen in the experiments for soft cantilevers in that work.

3.1.9. Large Slip Length Caused by Artifacts

Fig. 3.26a and b show F-D curves for a soft ($k = (0.04\,\mathrm{Nm}$) rectangular cantilever, acquired at the maximum speed of the instrument (nominal $v_p = 600\,\mu\mathrm{m/s}$) with a KCl 0.2 mol/L solution with added sucrose (40% weight concentration, $\eta = 6\,\mu\mathrm{Pas}$) on a SiO_2 surface. As discussed in the previous sections, this combination of parameters would be more prone to the measurement of an apparent slippage. The result of simulating Eq. 1.20 using the nominal v_p and assuming the drag on the cantilever constant is shown in Fig. 3.26a. The obtained apparent slip lengths are in the order of 100 nm. Fig. 3.26b shows the simulation curves after correction v_p as described in Section 3.1.4.1 and assuming a variable drag on the cantilever. The difference is clear, with the fit being qualitatively better. However, a slip length of 15 nm, similar to the one obtained when the cantilever was run at 40 μm/s still was needed to fit the data. This result stresses the effect that artifacts have on the measurement of slip lengths using CPT.

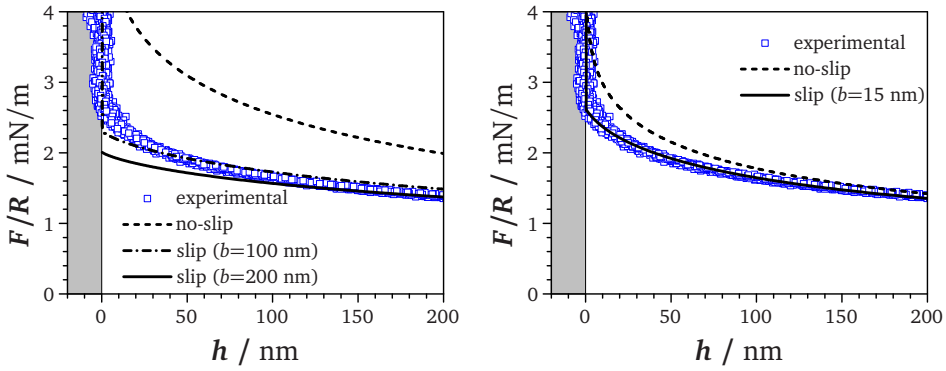

(a) before corrections **(b)** after corrections

Fig. 3.26.: F-D curves for a soft ($k = 0.04$ N/m), rectangular cantilever in a KCl 0.2 mol/L solution with added sucrose ($\eta = 6$ μPas) on a SiO_2 surface driven at the maximum speed of the instrument. (a) Simulations assuming the nominal $v_p = 600$ μm/s and constant drag. b values in the range of 100 nm have to be used to fit the data. (b) Simulations with the correct speed ($v_p = 347$ μm/s) and variable drag (Eq. 1.16). Even after corrections being applied, a $b = 15$ nm has to be used to fit the data.

3.1.10. Mapping the Results Together with the Literature Values

The results for the drainage of aqueous solutions over SiO_2 surface obtained here (Table 3.2) are summarized in Fig. 3.27, together with the data reported in the literature (Table 1.1). The degree of apparent slippage is represented by a color scale, with the spring constant in the abscissa, and ηv_p in the ordinate axis. The dimensionless number $\eta v_p/k$ represents a balance between the hydrodynamic forces acting on the probe divided by the restoring force of the cantilever.

The dimensionless number spans more than 4 orders of magnitude in the analysed experiments. Setting an arbitrary linear curve, $\eta v_p = 0.7k + 0.016$, a choice that was only dictated by the scattered points in the graph, it is possible to divide the data into two groups, those finding evidence for slip and those confirming the no-slip BC. Only two outlier experiments (Table 1.1 B and Table 3.2 L1) are present, out of more than 30 experiments. Fig. 3.27 can be used as a reference value when planning future experiments, allowing the experimenter to stay in the safe side when choosing the properties of the cantilever and of the liquid. The boundary condition to be applied when analyzing the force measurements does not seem

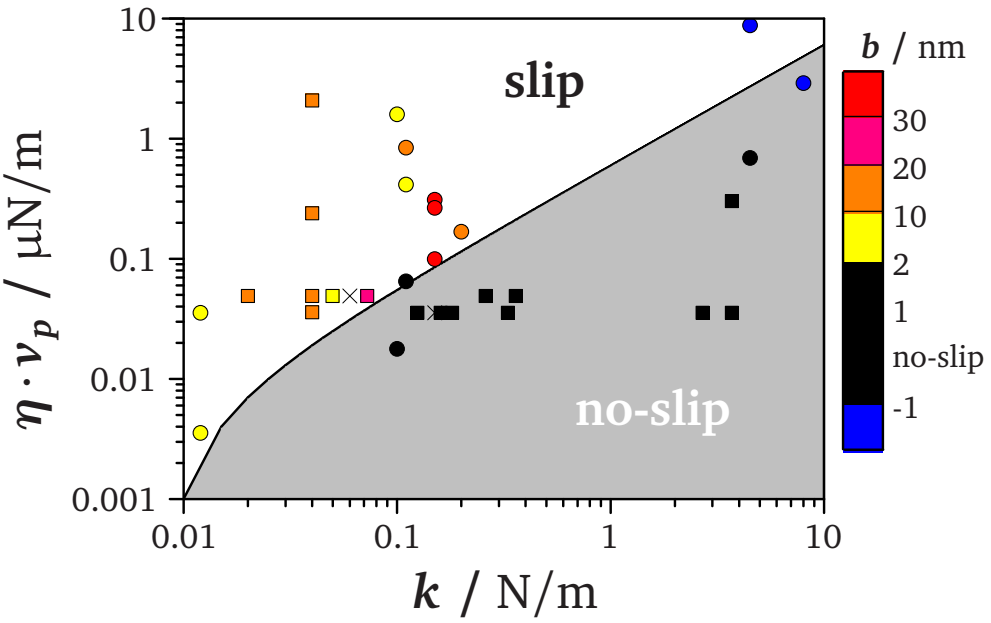

Fig. 3.27.: Measured slip lengths versus ηv_p and versus k. The slip length is given by the color bar on the right. The continuous line is a linear equation, $\eta v_p = 0.7 \cdot k - 0.016$ (ηv_p in μN/m). The circles represent the data from previous articles (Table 1.1) and the squares are the data from this study (Table 3.2). Superposed points have been displaced and a cross put in the original position of the points.

to be defined close to the threshold. A suggestion to avoid the cases where slippage is seen is to use a combination of parameters yielding a value lower than $\eta \cdot v_p/k = 10^{-7}$.

A parameter P that could separate the data from this work and the literature in two groups, one presenting slip BC and other no-slip BC, is helpful to avoid controvert values. It would be even more helpful if the measured b values were a function of this parameter. The parameter $\eta v_p/k$ yields a good result on separating the values in two groups, but there is a linear coefficient in the equation that is needed to separate the results. The linear coefficient of the obtained expression is small, but necessary for the separation, and suggests an extra dependence on the spring constant.

Apart from $\eta v_p/k$, many other combinations of the main parameters involved in the experiments (Eq. 1.20) were investigated to test if measured slip lengths were dependent on any of them. The idea remained the same as with the previous parameter: equating the forces contributing to the deflection of the cantilever (ηv_p) with the restoring force of the

Table 3.2.: Measured slip lengths as a function of experimental parameters, similarly tabulated as Table 1.1.

	b / nm	k / N/m	v_p / μm	R / μm	η / mPa·s	L	w / μm	Medium	Shape	$\eta v_p/k/1\times10^{-6}$
A1	0	0.15	40	9	0.89	350	35	Rectangular	KCl 0.2 mol/L (aqueous)	0.24
B1	10	0.02	55	8	0.89	350	35	Rectangular	KCl 0.2 mol/L (aqueous)	2.45
C1	10	0.04	55	11	0.89	350	35	Rectangular	KCl 0.2 mol/L (aqueous)	1.22
D1	0	0.16	40	10	0.89	350	35	Rectangular	KCl 0.2 mol/L (aqueous)	0.22
E1	0	0.33	40	9.5	0.89	350	35	Rectangular	KCl 0.2 mol/L (aqueous)	0.22
F1	0	2.7	40	10.2	0.89	110	35	Rectangular	KCl 0.2 mol/L (aqueous)	0.22
G1	20	0.06	55	11	0.89	350	35	Rectangular	KCl 0.2 mol/L (aqueous)	0.82
H1	0	0.15	40	4	0.89	350	35	Rectangular	KCl 0.2 mol/L (aqueous)	0.24
I1	0	0.26	55	10	0.89	350	35	Rectangular	KCl 0.2 mol/L (aqueous)	0.19
J1	0	0.36	55	10	0.89	100	13	V-shaped	KCl 0.2 mol/L (aqueous)	0.14
K1	5	0.06	55	8	0.89	196	23	V-shaped	KCl 0.2 mol/L (aqueous)	0.82
L1	0	3.7	40	10	0.89	200	52	Rectangular	KCl 0.2 mol/L (aqueous)	0.01
M1	10	0.04	40.4	8	0.89	350	35	Rectangular	KCl 0.2 mol/L (aqueous)	0.9
N1	10	3.7	600	10	0.89	200	52	Rectangular	KCl 0.2 mol/L (aqueous)	0.14
O1	15	0.04	40	10	6	350	35	Rectangular	KCl 0.2 mol/L (aqueous)+ sucrose 40%	6
P1	200	0.04	600	10	6	350	35	Rectangular	KCl 0.2 mol/L (aqueous)+ sucrose 40%	90

cantilever (k). No combination provided a quantitative relation describing the reported slip lengths. This can be a clue that an artifact is causing the reported slip lengths, because the measured b is independent of individual parameters of the experiment and the reported values are not congruent.

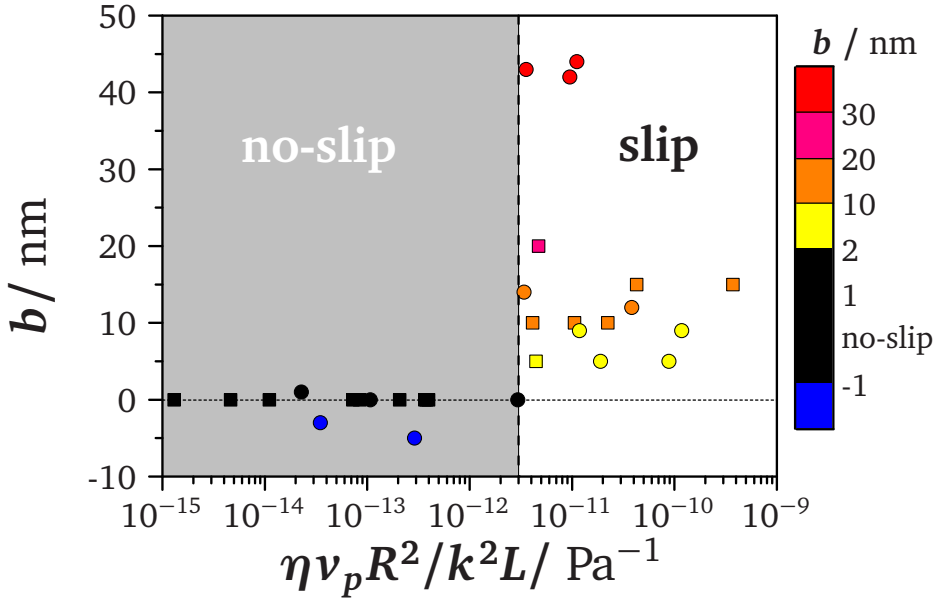

Fig. 3.28.: Measured apparent slip lengths versus $\eta v_p R^2/k^2 L$. The slip length is also organized in color ranges (color scale on the right). The vertical line was arbitrarily set at 3×10^{-12} Pa^{-1}

It was possible to find a parameter that could separate the available data in two groups, with a more clear boundary between then. This result was found for a value of P, as given in Eq. 3.4, and different from the previous parameter, it is not adimensional, having units of Pa^{-1}.

$$P = \frac{\eta v_p R^2}{k^2 L} \tag{3.4}$$

The result of plotting b versus P is found in Fig. 3.28. In the graph it is observed that after a value of 3×10^{-12} Pa^{-1} on, the experiments start to show slippage behavior, while before that threshold the no-slip BC can explain the results. No correlation between slip length b and the value of the parameter can be found, as it could not be found in the previous graph using ηv_p. Here, the data are separate in patterns, as evidenced by the color code

separating further the data in ranges. There are three points coming from one article [64], showing b values around 40 nm, that are outside the range of the rest of the published results. In that article, a different model was applied: it was assumed the no-slip BC for the solid surface, and the fitted slippage was assumed to arise from the sphere. All the other values are close to $b = 10$ nm.

It is hard, however, to correlated this parameter to some physical effect. One may see this parameter as a balance between the forces causing deflection of the cantilever ($\eta v_p R^2$) to the forces resisting the deformation, given by k and L. It is a simplification, especially because this expression is related to the drag on the sphere, whereas the drag on the cantilever plays a role on the deflection magnitude, and the relations are not completely straightforward. Moreover, after the discussion of the number of parameters that could cause artifacts, it is difficult that one single parameter could explain the effects, but it may show that a dominant process is responsible for the obtained results.

Both parameters relate slippage to a ratio between applied force on the cantilever to the restoring force of the cantilever. They are, therefore, related to the deflection of the cantilever, though not in a direct relationship. An alternative is to plot the measured slip lengths as a function of deflection, but the comparison is difficult since the employed model assumes a constant slip length for the entire F-D curve. For a comparison purpose, F-D curves were simulated and the deflection at a single distance was chosen and the slip lengths plotted as a function of it. Fig. 3.29 shows the slip lengths from Table 1.1 and Table 3.2 as a function of the expected deflection at $h = 5$ nm. The expected deflections were obtained by simulating Eq. 1.20 assuming the no-slip BC, and the drag coefficient of the cantilever as that of a cylinder (Eq. 3.2). The DLVO forces were included for a 0.2 mol/L solution and $A_H = 0.3 \times 10^{-20}$ J. Here, after a certain deflection threshold (27.5 nm), apparent slippage starts to be measured. For the results of this work no outlier to this trend is found; Most of the previous results from the literature follow the trend, with few outliers.

It is worth a note that the slip length has been used in the literature as a fitting parameter to explain the reduced deflections measured by CPT. The technique, being indirect, does

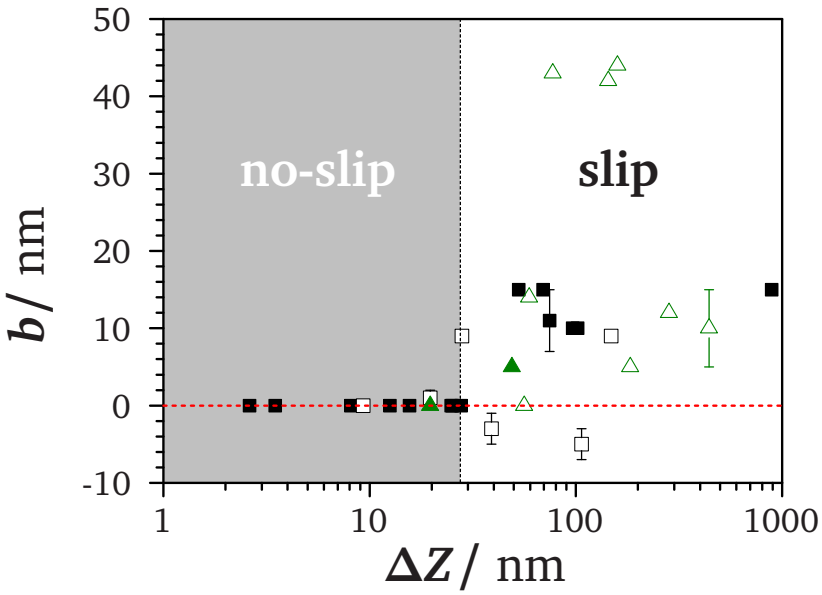

Fig. 3.29.: Measured apparent slip lengths versus simulated no-slip BC values of deflection at $h = 5$ nm. Squares represent results obtained with rectangular cantilevers, whereas triangles represent those obtained with V-shaped ones. Filled symbols are results from this work (Table 1.1), and empty ones are those from the literature (Table 3.2). The vertical line was arbitrarily set at 27.5 nm.

not measure strictly slippage, that can only be inferred from the effect on the cantilever. However, the patterns observed here, for the deflection and for the parameters, are not compatible with slippage. None of the described options, either real or apparent slippage follow a trend that the more the cantilever deflects, higher slip lengths are measured.

One of the hypothesis in favor of slippage is that after a certain shear rate threshold, the liquid start to slip over the surface. However, stiffer cantilevers attain higher shear rates than soft cantilevers (Fig. 3.14). Moreover, it has been speculated that stiffer cantilever may not be sensitive enough to measure slippage. Although sensitivity may be compromised for very stiff cantilevers at low speeds and low viscosities (Fig. 3.2), stiff cantilevers under the 27.5 nm-threshold were used to measure DLVO forces, smaller than the hydrodynamic ones, and the fit yielded the expected results.

It has been discussed that higher deflections lead to signal outside the linearity range of the detector [116]. Here, a set of experiments have been devoted to shown that this is not the case for the instrument employed here, though it can be the case for other instru-

ments (Section 3.1.6). Discarding problems of linearity on the detector, the residual slip length observed after the model refinements and artifact subtraction, is in agreement with some kind of stiffening process. One such process is the twisting of the cantilever while deflecting (Fig. 3.30).

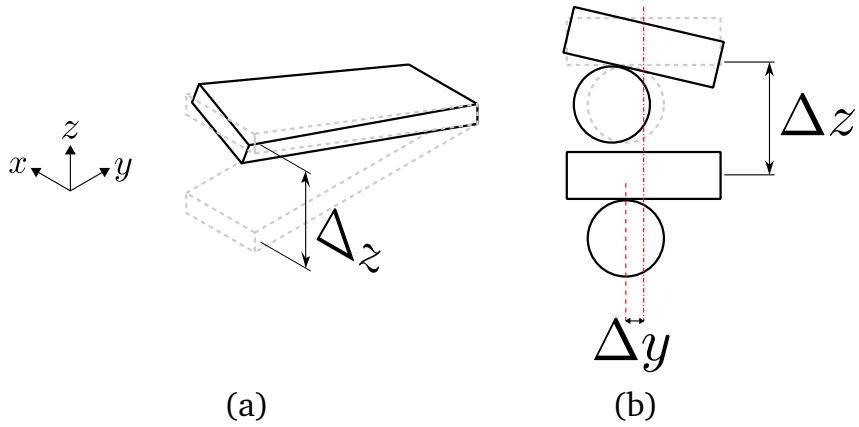

Fig. 3.30.: Illustration of the twisting of the cantilever combined to the deflection. (a) Schematics of the cantilever, showing that a twist of the cantilever may be combined to the deflection process. (b) A lateral offset of the sphere leads to a twist of the cantilever.

Cantilever twisting may be caused by a lateral offset of the sphere, or in the case of V-shaped cantilevers, by different properties of each of the arms. This argument has been proposed to explain the differences between rectangular and V-shaped cantilevers [123]. This hypothesis can generally explain the differences obtained in the literature. The soft, rectangular cantilevers are more affected because of positioning of the sphere. The V-shaped, in its turn, makes it easier to positioned the particle symmetrically due to its narrow shape; If, however, the arms do not have exactly the same measures, a twisting occurs. This also explains why a V-shaped cantilever needed a slightly smaller slip length than those needed for rectangular ones (Fig. 3.21). Small deviations occur as well for stiffer cantilevers, that yield slip lengths smaller than 1 nm (Fig. 3.22), which can have the origin on cantilever twisting.

3.1.11. Which Boundary Condition Should Be Applied?

The obtained results are in agreement with the physical justifications stating that the no-slip BC is the appropriate boundary condition to describe CPT drainage measurements of aqueous solutions over hydrophilic surfaces. It is in agreement also with recent results that propose the no-slip BC as adequate. Results with an improved FCS instrument yield slip lengths of less than 5 nm for the flow of water over a hydrophilic surface, within the experimental error of the technique [153]. CPT measurements in oscillatory mode [154], performed with the same colloidal probe and less prone to the effects describe in this work, show that the hypothesis that the interaction between the liquid and the surface dictate the transition from a no-slip BC regime to a slip BC regime, and showing that the no-slip BC is valid for water flow over hydrophilic surfaces. Also, recent simulations have also indicated that the relationship to wetability is valid [155]. Here, two different empirical thresholds could be fixed, based on variables of the experiment (Eq. 1.20). With those, it is possible to identify the parameters needed for the measured F-D curves to be described with the no-slip BC.

The presented results confirm that the stiffness of cantilevers affects the hydrodynamic force curves acquired with CPT: the softer the cantilever, the larger the slip length. It was observed a correlation between cantilever stiffness and slip length also within data published previously in the literature, showing that a too small value of k resulted in measuring an apparent slip length. However, as shown here, using stiff cantilevers alone does not ensure that the no-slip is the appropriated BC. Increasing the scanning velocity of the colloidal probe or increasing liquid viscosity leads as well to force curves with slip, even when a cantilever with a spring constant as high as 3.7 N/m is used. Although part of this dependence could be explained by artifacts and corrected by improved simulations, still soft cantilevers presented results yielding an apparent slippage afterward.

Real slippage is not expected for the flow of water over a SiO_2 surface according to the physical justifications presented in Section 1.2. Regarding molecular slippage, estimations are that the shear stresses applied on colloidal probe measurements are not enough to

surpass the binding energy of the solvent to the substrate, and that a speed as big as 1 m/s would be necessary to produce a hydrodynamic work bigger than the binding energy, and therefore liquid slippage [116]. The binding energy can be, however, much higher than the work required to shift a liquid molecule laterally on a surface. The analysis is further complicated because in CPT the shear rate is not constant along the plane.

Apparent slippage is also not expected; Such processes arise, for instance, with the accumulation of gas bubbles at the solid-liquid interface, or with viscosity changes at the interface [108]. The spontaneous formation of nanobubbles has not been observed in aqueous solutions over silicon substrates and the hypothesis of change in viscosity close to surface is not expected on a Newtonian liquid as water.

The lack of reproducibility on the slip length results among those using soft cantilevers suggests that some artifact is causing the apparent slippage measured by CPT on hydrophilic surfaces. Furthermore, the observed trends are not compatible with the available physical justifications for slippage (Section 1.2). The results shown here support this hypothesis, showing that a considerable part of the discrepant results can be reproduced as instrumental artifacts. It can be speculated that the residual slip observed is related to additional artifacts not studied here, such as the twisting of the cantilever due to misplacement of the sphere. Further studies are needed to identify this source of disagreement. The results presented here, though, indicate that a stiffening process of cantilever during deflection is the most probable option.

3.2. Drainage Measurements on Graphite Substrates

3.2.1. Comparing Substrates with Different Surface Energies

The results shown in Section 3.1 show that the use of CPT for dynamic drainage measurements should be done respecting a range of parameters to avoid controversial results. The origin of the observed differences show correlation to cantilever properties. The safest

approach to study drainage at surfaces is the comparison between surfaces, keeping the same probe.

During the analysis in Section 3.1, surface forces acting on the particle arose from similar surfaces. Here, the goal is to compare results obtained on different substrates, namely SiO_2 and HOPG surfaces. As before, the van der Waals and the electrostatic forces were calculated at low speed, where the hydrodynamic contribution is small. HOPG has been used previously as a substrate for CPT drainage measurements, with slip behavior being reported [37, 156].

HOPG surfaces are considered hydrophobic, but the reported contact angle measurements results for these surfaces vary considerably [37, 145, 157–167]. According to certain authors graphitic surfaces can be considered hydrophobic (contact angle $> 90°$), whereas for others the surface is hydrophilic, reaching contact angles of 42° [157]. One characteristic of HOPG surfaces is its smoothness, which makes it an excellent sample for AFM measurements. This smoothness is restricted to a few micrometers of length, and in a macroscopic scale steps are present, coming from breakups when the layers are peeled off. This steps have been reported to be hydrophilic [168], and a nucleation site for nanobubbles [169]. Another factor of error may be just the distortion of the contact line by several of these steps, giving a macroscopic impression of a different contact angle. This can also be a factor leading to an apparent slippage.

Independent of contact angles, the interaction between the silica particle with each of these surfaces is supposed to be different. The calculated Hamaker constant A_H for the interaction of two SiO_2 surfaces across water is in the range of $0.16 - 1.51 \times 10^{-20}$ J [97]. The A_H for the interaction of a SiO_2 particle with a graphitic surface across water is expected to be in the range of $1.26 - 3.88 \times 10^{-20}$ J as calculated [97] from the values above for the interaction of two SiO_2 across water and those of two graphite ones interacting in water [57]. The structure of the electric double layer may also be different. The glass surface has charges coming from the ionization of the silanol groups of the surface, and although at the pH = 6 from the solution most of the groups are protonated (pKa = 6.8, [125]), the

few deprotonated sites should be equally distributed. On the HOPG, however, the charges should be residual, due to the cleavage process, and are probably not uniformly distributed.

3.2.1.1. Approach curves

Two different sets of approach F-D curvesFig. (3.31): one for the interaction with a HOPG substrate and the other for the SiO_2 surface. Both were performed under the same conditions, using the same probe, same aqueous solution of KCl 0.5 mol/L, and same driving speed $v_p = 40$ μm/s. The HOPG curves (blue squares) have a profile similar to the curves obtained on a silicon surface (magenta crosses). The graph is presented in logarithmic scale to emphasize the differences between surfaces. The simulated curves are different for each surface because the surface forces measured at low speed were added to them. The fitted values of A_H were 0.6×10^{-20} J for the SiO_2 surface and 3×10^{-20} J for the HOPG surface for this specific experiment. If the surface forces were considered, the no-slip BC was sufficient to explain the results until $h = 10$ nm, for both surfaces. For $h < 10$ nm, a b value of 1 nm was needed to describe the data for both surfaces. The observed difference between SiO_2 e HOPG surfaces being only due to the DLVO forces.

The HOPG F-D curves at low speed have been fitted with a Hamaker constant similar to the expected value, what means that non-DLVO long–range interactions are not present. One explanation for results with non-DLVO interactions are nanobubbles attached to the surface, but recent results show that they do not spontaneously form in HOPG [170].

Published drainage experiments of a glass particle interacting with an HOPG surface yield lower force values when compared to a more hydrophilic surface [145]. Here the same is observed, with the F-D curves for HOPG having lower values than for SiO_2 surface. The difference, though, can be explained by adding the surface forces obtained from the slow curves. The hydrophilic surface used in that experiments was mica, a hydroxyl covered surface similar to the SiO_2 surface from the Silicon wafers. Mica ion exchange properties can, however, complicate evaluation of force data [171].

A simulated curve assuming the no-slip BC is sufficient to describe the experimental

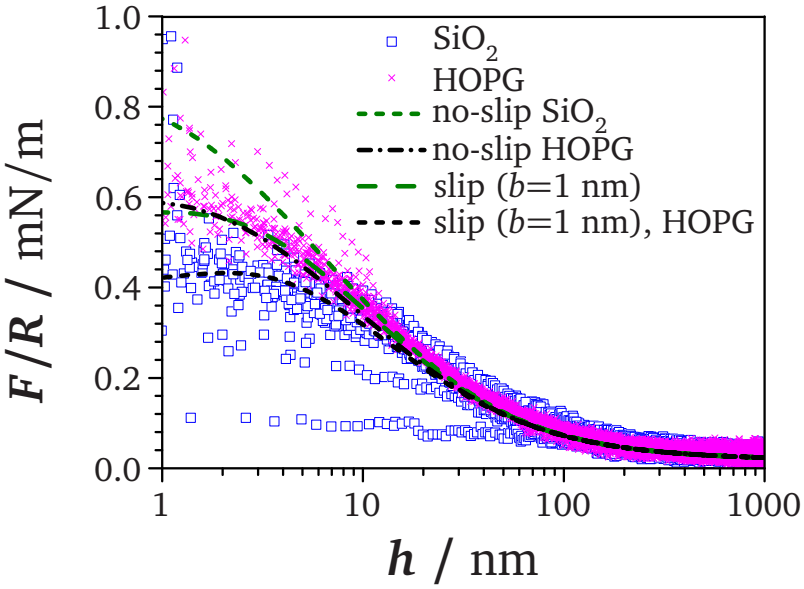

Fig. 3.31.: Approach F-D curves acquired at $v_p = 40$ µm/s in a KCl solution (0.5 mol/L) with the same cantilever for two different surfaces: SiO_2 (magenta crosses) and HOPG (blue squares). The graph is presented in logarithmic scale to emphasize the differences between surfaces. The simulated curves are different for each surface because the surface forces measured at low speed were added to them. $b = 1$ nm was enough to describe the data in both surfaces. $R = 8.5$ µm

F-D curves for a glass particle interacting with an HOPG surface, as it was the case for a SiO_2 surface. This is in disagreement to previously published results for oscillatory AFM measurements using a silicon cantilever with a 600 nm-radius tip and a HOPG surface [37]. In that study, a mica surface was also employed, and a slip length of 8 nm was found for the HOPG surface. They employed only water as separating medium, without addition of any salt. In pure water, the Debye length may reach hundreds of nanometers because of water dissociation and CO_2 absorption [97], and the authors did not include the surface forces in their simulation. This can explain the difference seen here. EDL and van der Waals forces should be included in the simulation, because of the extra forces reduces alters the result of differential Eq. 1.20.

3.2.1.2. Retract curves

The experimental retract curves (Fig. 3.32) for HOPG show force values surpassing those expected for a simulated curve using the no-slip BC. This can be attributed to adhesion between the particle and the substrate, as seen in the slow measurements. In experiments using Kelvin probe force microscopy [172], it has been shown that HOPG surfaces from samples peeled off in air present a contact potential lower than those prepared under ultra-high vacuum, what has been attributed to contamination of the surface [173]. This could explain the big variation on adhesion found for measurements on the HOPG substrate. Another point is that HOPG surface has steps because of its layered structure, and some of the map positions could have been acquired atop some of these steps, leading to a reduced contact area between particle and substrate.

The shape and roughness of the particle could also play a role in the observed difference in the retract curves, especially because the particle used does not fit a perfect spherical profile (Fig. A.3b, Appendix). However this did not affect significantly the hydrodynamics results for the SiO_2 surface, the reference substrate. The slip length needed to explain the results once the surface force have been subtracted was of only 1 nm, inferior to the measured Z_{PV} value. It is possible to assume that it did not affect the HOPG measurements as well.

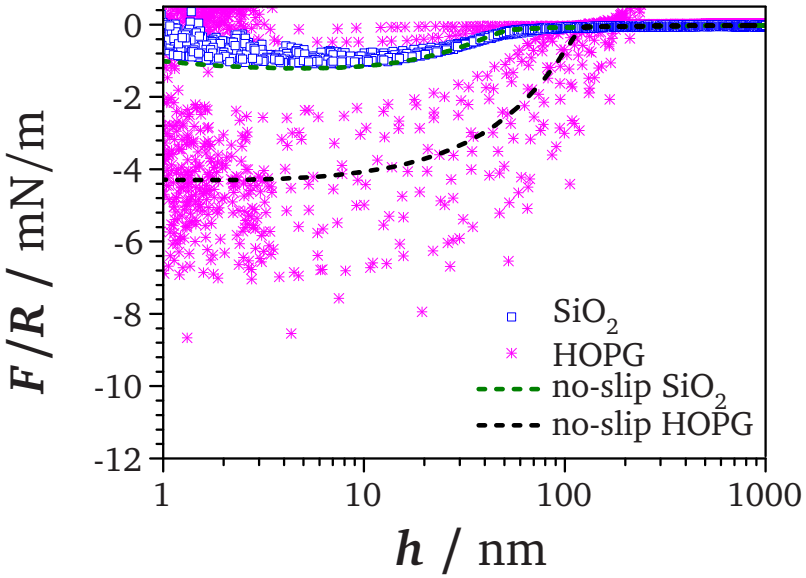

Fig. 3.32.: Retract curves obtained against two different surfaces: SiO_2 surface (blue squares) and HOPG (magenta stars). The curves were acquired at $v_p = 40$ µm/s in a KCl solution (0.5 mol/L) with the same cantilever.

3.2.2. Varying Solution Concentrations and Salt Cations

Fig. 3.33 shows the value of F/R at $h = 15$ nm for different aqueous, salt solutions of alkaline chlorides for the approach against a HOPG surface. The graph shows that no specific effect is seen because of the addition of salt nor its concentration or the cation. As seen in Section 3.1, the differences for an apparent slippage are larger away from the surface, with those related to the surface roughness appearing at $h < 10$ nm. Choosing the values at distance of 15 nm still gives a good signal-to-noise ratio, and it keeps the data away from variations related to surface roughness. It also lowers the influence of surfaces forces, although on the diluted solutions there is a strong electrostatic component at this distance. Results in the literature suggest that different cations may result in different friction properties, for example between SiO_2 surfaces [174]. Previous results did not show any special effects on CPT drainage measurements for different anions and cations [175].

No trend can be seen for the four different cations and for the different concentrations used. The same was observed on the retract curves (Fig. 3.34). There, the value of the minimum of adhesion for different salt solutions measured on the retract of the same can-

tilever from a HOPG surface is shown, and no trend can be seen as well. For slow curves in LiCl 0.0005 mol/L it can be seen that the values for both approach and retract are lower than expected if compared to the other salts, but this was not seen in other experiments with LiCl, and it can be seen that the impact on the fast curves is not pronounced. This has been seen in other experiments as well with other cations, and it is not reproducible. The data are kept for comparison, since all points corresponds to experiments performed with a single cantilever and particle, performed in the same day. This task was important to avoid differences coming from artifacts shown before. Also, the order show in the graph was not the one that the experiments were performed. Although they were performed from the more diluted solution to the more concentrated one, the salt was alternated in the order LiCl, RbCl, NaCl, and KCl. The graphite was peeled after salt exchange, and no trend was observed regarding experiment order.

Further studies are needed to understand the behavior of the double layer, where the processes regarding the combination of electrostatic and van der Waals forces are predominant and the continuous nature of the models are prone to fail. Technical drawbacks have to be surpassed though, for example the noise present in the measurements. Smooth surfaces at a large scale are desired as well, avoiding problems such the steps in the HOPG surface.

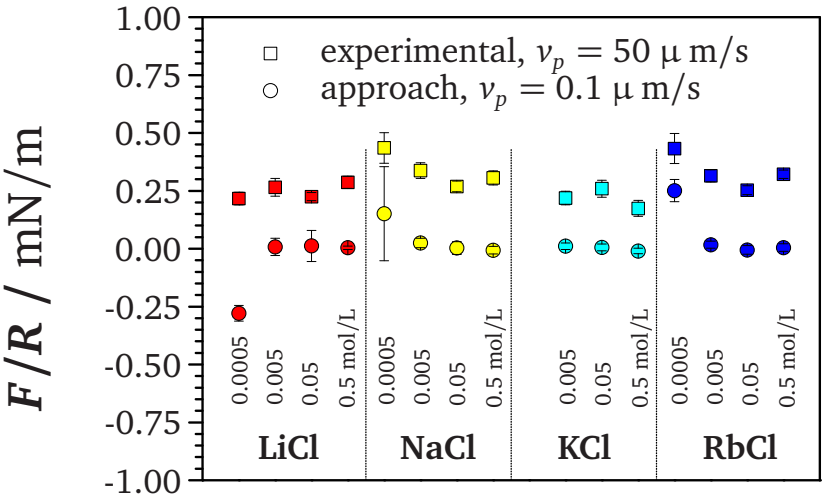

Fig. 3.33.: F/R measured from approach F-D curves at $h = 15$ nm with aqueous solutions of different alkaline chlorides, ordered according to the cation ionic radius. The squares represent the data at $v_p = 50$ μm/s, where the hydrodynamic force is more pronounced, and the circles the data at $v_p = 0.1$ μm/s, where surface forces are predominant. Each of the salts corresponds to a different color, and within each salt organized by concentration, from the more diluted to the more concentrated.

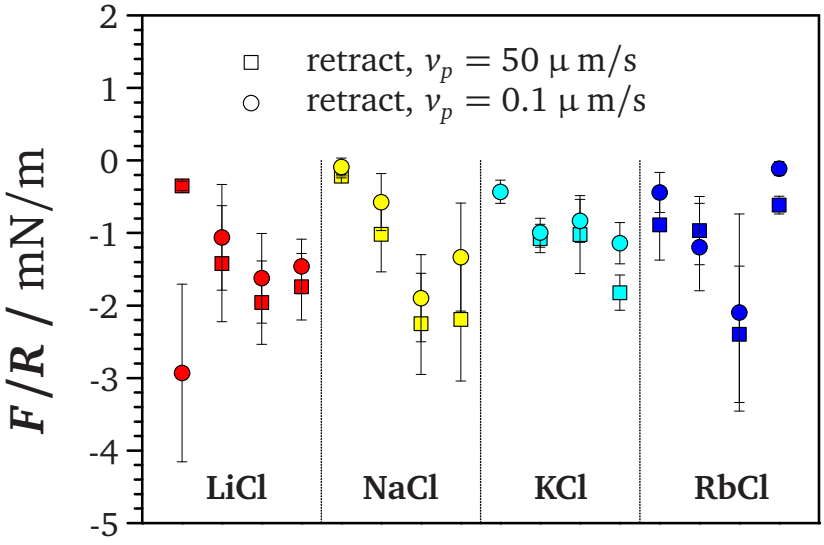

Fig. 3.34.: F/R measured from retract F-D curves at the minimum of the curve, with aqueous solutions of different alkaline chlorides, ordered according to the cation ionic radius. The pattern is the same as in Fig. 3.33: The squares represent the data at $v_p = 50$ μm/s, where the hydrodynamic force is more pronounced, and the circles the data at $v_p = 0.1$ μm/s, where surface forces are predominant. Each of the salts corresponds to a different color, and within each salt organized by concentration, from the more diluted to the more concentrated.

4. Conclusions and Outlook

The obtained results are in agreement with the physical justifications stating that the no-slip BC is the appropriate boundary condition to describe CPT drainage measurements of aqueous solutions over hydrophilic surfaces. It is in agreement also with recent results confirming that proposition [153–155]. Two different empirical thresholds could be fixed, based on variables of the experiment (Eq. 1.20). With those, it is possible to identify the parameters needed for the measured F-D curves to be described with the no-slip BC.

By the results shown here, the controversy over the applicability of the slip or no-slip BC on the drainage of aqueous solutions over hydrophilic substrates can be narrowed down to experimental parameters, especially the cantilever spring constant k. No trend on the measured slip lengths as a function of one variable present in the equation describing the experiments has been observed. Notwithstanding, the difference was clear when plotting the measured slip lengths against two different parameters calculated from a combination of variables, such as the spring constant, the speed of the piezo scanner and the liquid viscosity. Gathering results previously reported in the literature with new experiments made possible to distinguish results presenting apparent slippage from those obeying the no-slip BC.

The physical effect causing an apparent slip in CPT experiments with soft cantilevers depending on $\eta v_p/k$ or $\eta v_p R^2/k^2 L$ is still not completely clear. However, the observed trends are not compatible with the available physical justifications for the existence of liquid slippage (Section 1.2). The results shown here support this hypothesis, showing that a considerable part of the discrepant results can be reproduced as instrumental artifacts.

It can be speculated that the residual slip observed is related to additional artifacts not studied here, such as the twisting of the cantilever due to misplacement of the sphere. Further studies are needed to identify this source of disagreement. The results presented here, though, indicate that a stiffening process of cantilever during deflection is the most probable option.

It was possible to reproduce all the previous published results using CPT to probe drainage of aqueous solutions between hydrophilic surfaces. This was an important step for the discussion, since results of other groups have not been verified, for that often had their validity contested. Some of the trends could be explained by instrumental artifacts that are independent of a particular device. This shows that the whole CPT community has to observe the instrument behavior in order to avoid controvert results. Moreover, a combination of other factors contribute to the appearance of an apparent slip length, such as roughness or hydrodynamic drag on the cantilever. Contrary to suggested in the literature, a single factor could not be pointed as the source of the discrepancy; Many factors, though with small contribution, have to be controlled and included in the model to avoid the appearance of an apparent slippage.

Despite of CPT being an indirect technique and presenting artifacts that could compromise the results, most of them described in this work, it should not be disregarded as a tool for studying flow at surfaces. Other techniques suffer from lack of resolution and are not free from artifacts as well. The results, in fact, show that a thorough examination of possible experimental artifacts is recommended for other techniques described in Section 1.3.

An approach to minimize the effect of artifacts is to perform comparative measurements. With this approach it was possible to infer that for surfaces with different surface energy, namely SiO_2 and HOPG, curves agreed with each other if the DLVO forces were taken into account, having the same degree of discrepancy to the curve assuming the no-slip BC. The experiments on a HOPG surface showed also that, for alkaline chloride salts, there is no major influence on the magnitude of the fast curves for distances higher than the Debye length. This gives another useful approach to concentrate efforts in search for differences

at small separations.

Despite a number of papers on the colloidal probe drainage measurements, there is not a full description of the hydrodynamic drag distributed along the cantilever, and whether it may alter the deflection of the cantilever. A comparison of the experimental results with simulations using fluid-structure interaction using finite-element method software is needed in the field. The factors cited here, such as cantilever stiffness, medium viscosity and speed of piezo scanner should be considered. Some simulations related to cantilevers are available in the literature, but they normally focus on vibrating cantilevers [176].

Additionaly, a proper modeling of how roughness alters the fluid is needed. The models used so far are helpful for setting some conditions, but do not contribute significantly for an understanding of how the molecules behave at the vicinity of the surface. Many groups have been working on molecular dynamics simulations to understand how the flow behaves both in smooth and rough surfaces, but the number of molecules are still limited for an extrapolation to bigger fluid volumes, what explains why these results are also controvert [14]. The computational techniques have been advancing in a fast pace. It can then be extrapolated that in some years, molecular simulations with dimensions compared to those of real devices will be possible.

In terms of experiments, a study with a series of patterns is needed. In the case of the CPT, patterns taking into account the circular flow profile of the colloidal probe should be considered. The roughness of the borosilicate particles attached to the cantilevers is also a factor difficult to control. Recent research show the possibility of fabricating silicon microspheres [177], that in preliminary tests showed to be less rough than the borosilicate ones. If the trend is confirmed, this may be an option for future drainage measurements.

The effect of the arrangement of ions close to interfaces has seen progress in the last years [178]. Inspecting the results in Section 3.2, it seams that the direction is to study more complex di- and trivalent ions, and concentrate the experiments to distances smaller than the Debye length. One option, is to employ oscillatory AFM force measurements [37, 156, 179, 180]. Care should be taken, because this method operates at higher oscilla-

tions frequencies, and inertial terms have to be taken into account. The dynamics of the cantilever has to be also well understood.

In this work, HOPG has been used for experiments comparing different surface energies. However, the hydrophobicity of HOPG is contested. In order to observe some of the effects cited in the literature, such as nanobubbles, superhydrophobic surfaces [181] should be used instead.

A. Reverse AFM Images of Particles Cited in This Work

This appendix presents reverse AFM images of the particles cited in this work. In the captions are listed the figures which reported the experiments in which they were used. A note regarding all profiles shown in this appendix: the particles have a spherical shape and not a paraboloid one, as it may appear as first impression from the plotted profiles. This happens because the ordinate and the abscissa axes are not in a 1:1 proportion. Care should be taken when interpreting the relative size of the features compared to the size of the particle.

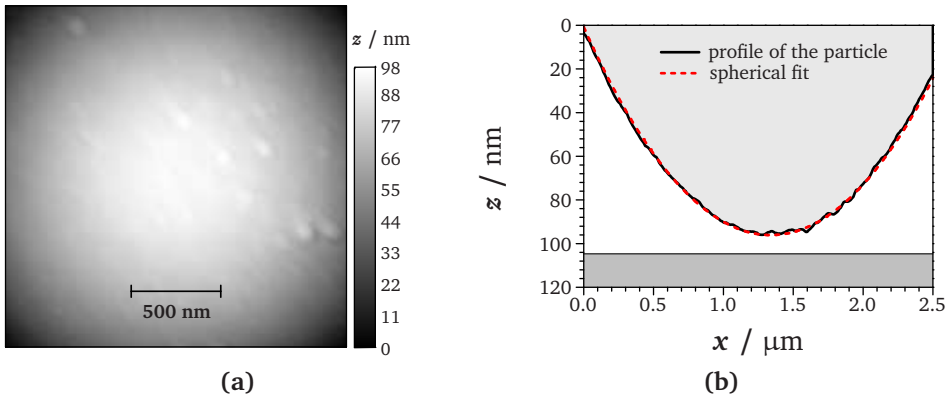

Fig. A.1.: Colloidal probe used on experiments from **Fig. 3.1** and **Fig. 3.5:** (a) Reverse flattened AFM height image revealing the local roughness. $Z_{RMS} = 0.5$ nm and $Z_{PV} = 7.5$ nm. (b) Profile of a transversal cut on the same image: the thick line corresponds to a section crossing the particle apex and the red dashed line is a sphere fit.

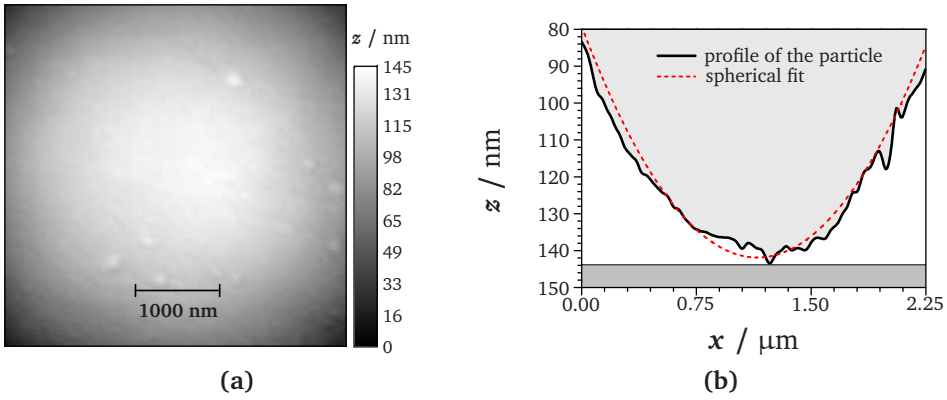

Fig. A.2.: Colloidal probe used on experiments from **Fig. 3.4**: (a) Reverse flattened AFM height image revealing the local roughness. $Z_{RMS} = 0.6\,\text{nm}$ and $Z_{PV} = 5.3\,\text{nm}$. (b) Profile of a transversal cut on the same image: the thick line corresponds to a section crossing the particle apex and the red dashed line is a sphere fit.

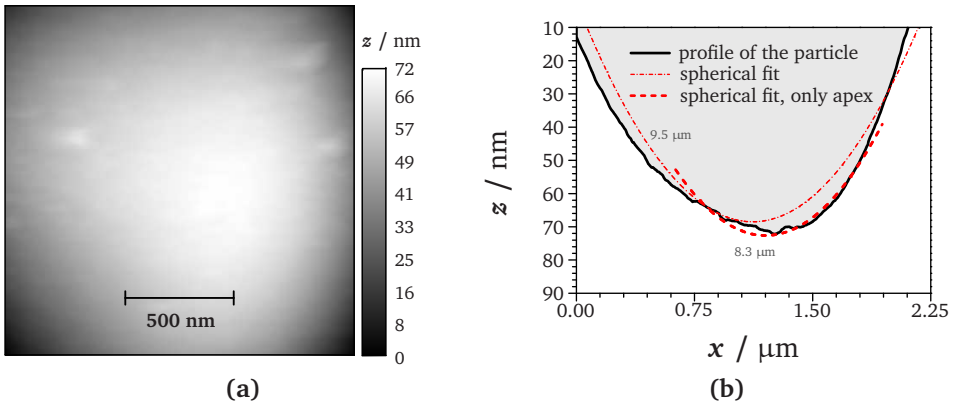

Fig. A.3.: Colloidal probe used on experiments from **Fig. 3.31**: (a) Reverse flattened AFM height image revealing the local roughness. $Z_{RMS} = 0.7\,\text{nm}$ and $Z_{PV} = 2.5\,\text{nm}$. (b) Profile of a transversal cut on the same image: the thick line corresponds to a section crossing the particle apex and the red dashed line is a sphere fit.

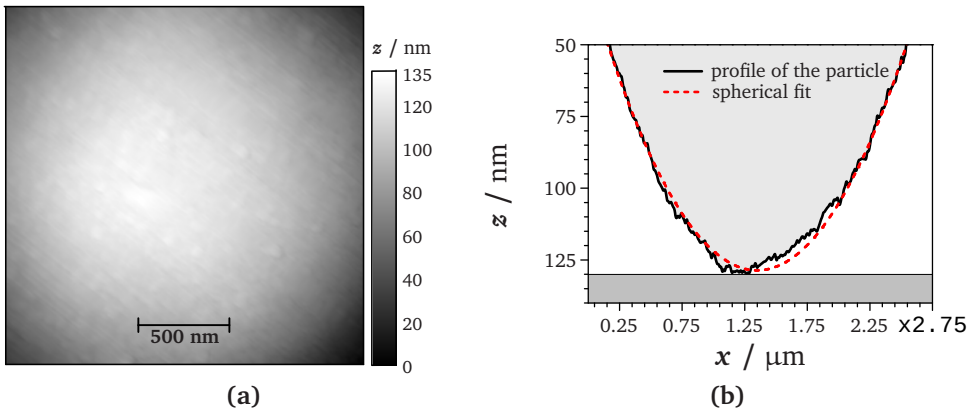

Fig. A.4.: Colloidal probe used on experiments from **Section 3.1.8.1**: (a) Reverse flattened AFM height image revealing the local roughness. $Z_{RMS} = 1$ nm and $Z_{PV} = 1.5$ nm. (b) Profile of the colloidal probe image shown the thick line corresponds to a section crossing the particle apex and the red dashed line is a sphere fit.

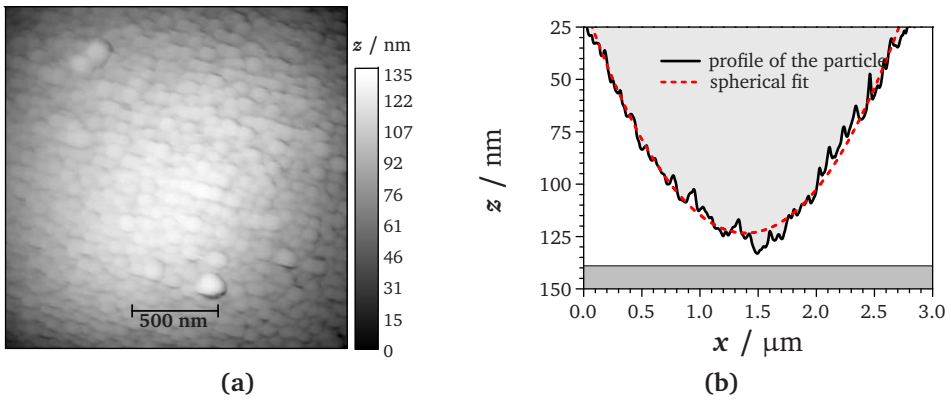

Fig. A.5.: Colloidal probe used on experiments from **Section 3.1.8.2**: (a) Reverse flattened AFM height image revealing the local roughness. $Z_{RMS} = 2$ nm and $Z_{PV} = 3$ nm. (b) Profile of the colloidal probe image shown the thick line corresponds to a section crossing the particle apex and the red dashed line is a sphere fit.

B. AFM Images of the Patterned Substrates Used in This Work

AFM images of the patterned substrates used in Roughness experiments (Section 3.1.8.1)

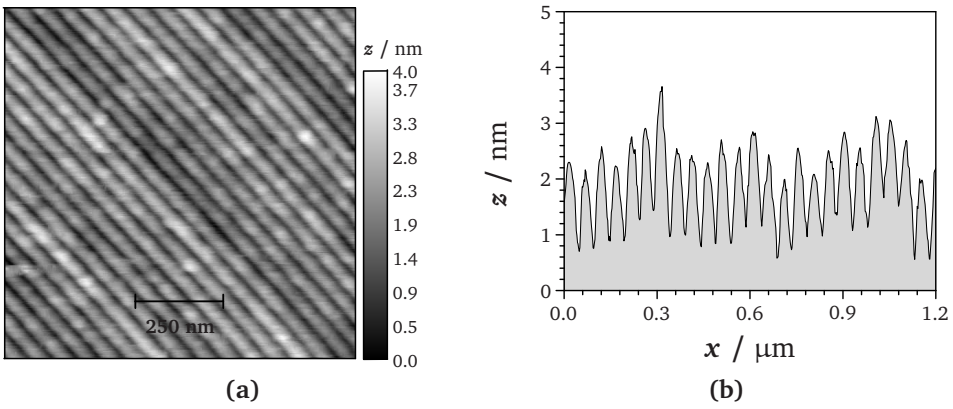

Fig. B.1.: Pattern on a silicon substrate with a sinusoidal profile used for curves shown on Fig. 3.22. $Z_{PV} = 4$ nm

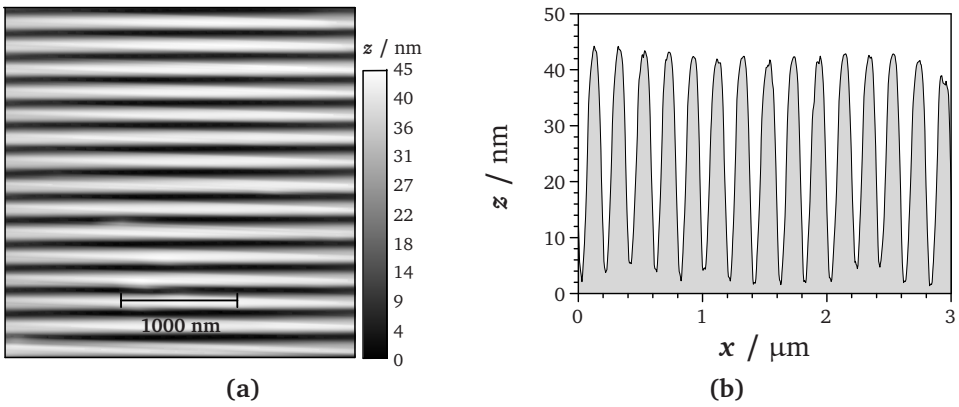

Fig. B.2.: Pattern on a silicon substrate with a sinusoidal profile used for curves shown on Fig. 3.24. $Z_{PV} = 45$ nm

C. Cantilever Calibration after Particle Attachment

CPT measurements require extensive preparation because of the need of attaching a particle to the end of a cantilever. Finding a particle with a determined spherical shape and with low roughness is time costing, especially because the particle needs to be characterized after attachment. The results of Section 3.1 show that the safest approach when performing force measurements, particularly at large values of the relation $\eta v_p/k$, is to employ the same probe on all runs of the experiment. For series with many samples and fluid exchange this poses a challenge because the cantilever is an easy target to be broken in the middle of an experiment because of its fragility.

Cantilevers are normally calibrated before the attachment of the particle, as described in section 2.2.2. After calibration, the particle is glued and then characterized, either by scanning electron microscopy or by AFM imaging as done here. Both the gluing of the particle and the imaging processes can result in a broken cantilever, and only after the imaging it is possible to know whether the particle has the desired roughness and shape. Taking into account that most of the particles are rejected, the user spend most of the time calibrating cantilevers that will never be used. Therefore, calibrating the cantilever after the characterization of the particle saves time and manipulation of the cantilever. The question is whether the calibration procedure is affected by using a colloidal probe with the probe already attached.

Fig. C.1 shows the difference between k values for 37 cantilevers plotted against their

lengths. In the upper part of the figure the difference $(k_{sph}/k_0) - 1$ is plotted and in the lower part the same relation is plotted, but k_{sph} is corrected for the positioning of the sphere, with the corrected $k_{sph} = k_0 \cot(L/L_{sph})^3$ [129]. For these experiments, the true position of the sphere was not measured, so it was assumed that the particle was one radius away from the free end of the cantilever. The results show that using the thermal noise method, the spring constant values obtained after the particle attachment were, in average, 15% higher than the value obtained for the bare cantilever, but the difference can be accounted by the correction for the position of the sphere.

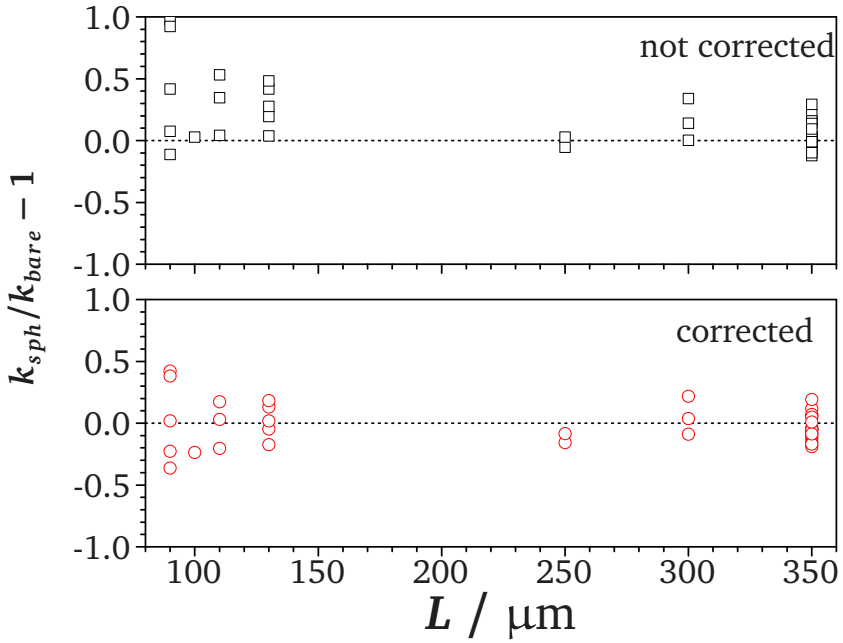

Fig. C.1.: Plot of the relative difference between k_{sph} and k_{bare} (non corrected), and the same relation using the effective k. $k_{sph} = k_0 \cdot (L/L_{sph})^3$ [129].

The use of a correction is used only to bring both values to same reference and does not imply any choice of the right value. The positioning of the laser leads to changes in the measured k values, what requires caution when comparing experiments performed for different alignments [182]. The laser position changes every time the cantilever is mounted on the support, being the effect more pronounced the shorter the cantilever gets.

This correction has been recently ignored in two publications where the thermal noise method has been used as comparison to proposed calibration methods. Chung et al. [183]

results show that thermal noise calibrated cantilevers have a measured k higher than those obtained via their non-contact electrostatic method. Inspecting the colloidal probe image shown in their article, it is possible to see that the particle is positioned away from cantilever edge. Assuming that the observed difference is only due to off-load positioning, it is possible to calculated that their probe was approximately 11 μm away from the edge, what seems reasonable when compared to the colloidal probe image. This could be an alternative explanation for their difference between methods instead of the correction factor proposed.

In another article [184], although the corrections are also ignored, the difference is the opposite: the thermal noise of the cantilever is lower than the one measured by their hydrodynamic method. Here the comparison is further complicated because they performed the thermal noise calibration inside water, without any correction for the hydrodynamic drag on the oscillation of the cantilever. Although it is known to be possible to perform thermal noise calibrations in liquids, it is not known whether the addition of a sphere requires an additional correction when calibrated inside liquids.

It is therefore possible to conclude that the calibration by the thermal noise method can be performed after the attachment of the particle, without any additional error beyond the known limitations of the technique, provided that the value is corrected for the position of the sphere. This result has the potential to decrease the time needed in the preparation of a colloidal probe, especially in cases where the surface of the particle has features that normally cannot be inferred before its characterization. The calibration can be performed together with the surface characterization of the tip by the inverse AFM method. Use of the calibration grid as substrate reduces the adhesion of the tip to the substrate, because of the reduced surface provided by the grid. Different from normal AFM tips, particles tend to condensate more water because of its larger surface area, leading to higher adhesion and distortion of the CCR for sensitivity calibration. Calibrating and characterizing the particle in the same step also optimizes the procedure, allowing the user to calibrate only those particles selected in the imaging procedure.

References

1. Batchelor, G. K. *An Introduction to Fluid Dynamics*; Cambridge University Press, 1967.
2. Eckert, M. *The Dawn of Fluid Dynamics: A Discipline between Science and Technology*; Wiley-VCH Verlag, 2006.
3. Bushnell, D. M.; Moore, K. J. *Annual Reviews of Fluid Mechanics* **1991**, *23*, 65–79.
4. Brostow, W. *Journal of Industrial and Engineering Chemistry* **2008**, *14*, 409–416.
5. Virk, P. S. *AIChE Journal* **1975**, *21*, 625–656.
6. Dujmovich, T.; Gallegos, A. *Offshore* **2005**, *65*, 55–58.
7. Hughes, W. F.; Brighton, J. A. *Schaum's Outline of Theory and Problems of Fluid Dynamics*; Schaum's outline series; McGraw Hill, 1999.
8. Zhang, C. *Tribology International* **2005**, *38*, 443–448.
9. Warszynski, P. *Advances in Colloid and Interface Science* **2000**, *84*, 47–142.
10. Stone, H. A.; Stroock, A. D.; Ajdari, A. *Annual Review of Fluid Mechanics* **2004**, *36*, 381–411.
11. Lesne, A. *Mathematical Structures in Computer Science* **2007**, *17*, 185.
12. Holt, J. K.; Park, H. G.; Wang, Y.; Stadermann, M.; Artyukhin, A. B.; Grigoropoulos, C. P.; Noy, A.; Bakajin, O. *Science (New York, N.Y.)* **2006**, *312*, 1034–7.
13. Goldstein, S. *Annual Review of Fluid Mechanics* **1969**, *1*, 1–29.
14. Neto, C.; Evans, D. R.; Bonaccurso, E.; Butt, H.-J.; Craig, V. S. J. *Reports on Progress in Physics* **2005**, *68*, 2859–2897.
15. Lauga, E.; Brenner, M.; Stone, H. In *Handbook of Experimental Fluid Dynamics*; Tropea, C., Yarin, A., Foss, J. F., Eds.; Springer, 2007; Chapter 19, pp 1219–1240.
16. Matthews, M. T.; Hill, J. M. *International Journal of Nanotechnology* **2008**, *5*, 218.
17. Einzel, D.; Parpia, J. *Journal of Low Temperature Physics* **1997**, *109*, 1–105.
18. Denn, M. M. *Annual Review of Fluid Mechanics* **2001**, *33*, 265–287.
19. Dussan V., E. B. *Journal of Fluid Mechanics* **1976**, *77*, 665–684.
20. Chan, D. Y.; Horn, R. G. *The Journal of Chemical Physics* **1985**, *83*, 5311.

21. Bonaccurso, E.; Kappl, M.; Butt, H.-J. *Physical Review Letters* **2002**, *88*, 076103+.
22. Craig, V. S. J.; Neto, C.; Williams, D. R. *Physical Review Letters* **2001**, *87*, 054504+.
23. Sun, G.; Bonaccurso, E.; Franz, V.; Butt, H.-J. *The Journal of Chemical Physics* **2002**, *117*, 10311.
24. Neto, C.; Craig, V. S. J.; Williams, D. R. M. *The European Physical Journal E: Soft Matter and Biological Physics* **2003**, *12*, 71–74.
25. Honig, C. D. F.; Ducker, W. A. *Journal of Physical Chemistry C* **2008**, *112*, 17324–17330.
26. Honig, C. D. F.; Ducker, W. A. *Physical Review Letters* **2007**, *98*, 16300–16312.
27. Vinogradova, O. I.; Yakubov, G. E. *Phys. Rev. E* **2006**, *73*, 45302.
28. Acheson, D. J. *Elementary Fluid Dynamics*; Oxford Applied Mathematics and Computing Series; Clarendon Press: Oxford, 1990.
29. Vinogradova, O. I. *Langmuir* **1995**, *11*, 2213–2220.
30. Granick, S.; Zhu, Y.; Lee, H. *Nature materials* **2003**, *2*, 221–7.
31. Khurana, A. *Physics Today* **1988**, *41*, 17.
32. Churaev, N. V.; Sobolev, V. D.; Somov, A. N. *Journal of Colloid and Interface Science* **1984**, *97*, 574–581.
33. Blake, T. D. *Colloids and Surfaces* **1990**, *47*, 135–145.
34. Baudry, J.; Charlaix, E.; Tonck, A.; Mazuyer, D. *Langmuir* **2001**, *17*, 5232–5236.
35. Tretheway, D. C.; Meinhart, C. D. *Physics of Fluids* **2002**, *14*, L9.
36. Cottin-Bizonne, C.; Steinberger, A.; Cross, B.; Raccurt, O.; Charlaix, E. *Langmuir* **2008**, *24*, 1165–72.
37. Maali, A.; Cohen-Bouhacina, T.; Kellay, H. *Applied Physics Letters* **2008**, *92*, 053101.
38. Bhushan, B.; Wang, Y.; Maali, A.; Wang, Y.; Bhushan, B.; Wang, Y.; Maali, A. *Langmuir* **2009**, *25*, 8117–21.
39. Pit, R.; Hervet, H.; Leger, L. *Physical review letters* **2000**, *85*, 980–3.
40. Craig, V. S. J.; Neto, C. *Langmuir* **2001**, *17*, 6018–6022.
41. Zhu, Y.; Granick, S. *Physical Review Letters* **2004**, *93*, 096101.
42. Joseph, P.; Tabeling, P. *Physical Review E* **2005**, *71*, 035303(R).
43. Willmott, G.; Tallon, J. *Physical Review E* **2007**, *76*, 066306.
44. Willmott, G.; Tallon, J. *Current Applied Physics* **2008**, *8*, 433–435.

45. Cho, J.-H. J.; Law, B. M.; Rieutord, F. *Physical Review Letters* **2004**, *92*, 166102+.

46. Thompson, P. A.; Troian, S. M. *Nature* **1997**, *389*, 360–362.

47. Brochard, F.; De Gennes, P. G. *Langmuir* **1992**, *8*, 3033–3037.

48. Zhu, Y.; Granick, S. *Physical review letters* **2001**, *87*, 96105.

49. Cottin-Bizonne, C.; Barentin, C.; Charlaix, E.; Bocquet, L.; Barrat, J.-L. *The European physical journal. E, Soft matter* **2004**, *15*, 427–38.

50. de Gennes, P. G. *Langmuir* **2002**, *18*, 3413–3414.

51. Lauga, E.; Brenner, M. *Physical Review E* **2004**, *70*, 1–7.

52. Craig, V. S. J. *Soft Matter* **2011**, *7*, 40.

53. Mezger, M.; Schöder, S.; Reichert, H.; Schröder, H.; Okasinski, J.; Honkimäki, V.; Ralston, J.; Bilgram, J.; Roth, R.; Dosch, H. *The Journal of chemical physics* **2008**, *128*, 244705.

54. Bonaccurso, E.; Kappl, M.; Butt, H.-J. *Current Opinion in Colloid & Interface Science* **2008**, *13*, 107–119.

55. Kim, H. I.; Kushmerick, J. G.; Houston, J. E.; Bunker, B. C. *Langmuir* **2003**, *19*, 9271–9275.

56. Guriyanova, S.; Mairanovsky, V. G.; Bonaccurso, E. *Journal of colloid and interface science* **2011**, *360*, 800–4.

57. Li, Y.; Kanda, Y.; Shinto, H.; Vakarelski, I.; Higashitani, K. *Colloids and Surfaces A: Physicochemical and Engineering Aspects* **2005**, *260*, 39–43.

58. Hocking, L. M. *Journal of Fluid Mechanics* **1976**, *76*, 801.

59. Baldoni, F. *Journal of Engineering Mathematics* **1996**, *30*, 647–659.

60. Richardson, S. *Journal of Fluid Mechanics Digital Archive* **1973**, *59*, 707–719.

61. Jabbarzadeh, A.; Atkinson, J. D.; Tanner, R. I. *Physical Review E* **2000**, *61*, 690–699.

62. Ponomarev, I. V.; Meyerovich, A. E. *Phys. Rev. E* **2003**, *67*, 26302.

63. Zhu, Y.; Granick, S. *Physical Review Letters* **2002**, *88*, 106102+.

64. Bonaccurso, E.; Butt, H.-J.; Craig, V. S. J. *Physical Review Letters* **2003**, *90*, 144501+.

65. Schmatko, T.; Hervet, H.; Léger, L. *Langmuir* **2006**, *22*, 6843–50.

66. Truesdell, R.; Mammoli, A.; Vorobieff, P.; van Swol, F.; Brinker, C. J. *Phys. Rev. Lett.* **2006**, *97*, 44504.

67. Day, M. A. *Erkenntnis* **1990**, *33*, 285–296.

68. Jackson, M. J. *Micro and Nanomanufacturing*; Springer US, 2007.

69. Huang, P.; Guasto, J. S.; Breuer, K. S. *Journal of Fluid Mechanics* **2006**, *566*, 447.

70. Pit, R.; Hervet, H.; Léger, L. *Tribology Letters* **1999**, *7*, 147–152.

71. Gösch, M.; Blom, H.; Holm, J.; Heino, T.; Rigler, R. *Analytical Chemistry* **2000**, *72*, 3260–3265.

72. Yordanov, S.; Best, A.; Butt, H.-J.; Koynov, K. *Optics Express* **2009**, *17*, 21149.

73. Joly, L.; Ybert, C.; Bocquet, L. *Physical Review Letters* **2006**, *96*, 046101.

74. Lumma, D.; Best, A.; Gansen, A.; Feuillebois, F.; Rädler, J.; Vinogradova, O. I. *Physical Review E* **2003**, *67*, 056313.

75. Choi, C.-H.; Westin, K. J. A.; Breuer, K. S. *Physics of Fluids* **2003**, *15*, 2897.

76. Ellis, J. S.; Hayward, G. L. *Journal of Applied Physics* **2003**, *94*, 7856.

77. Platikanov, D. *The Journal of Physical Chemistry* **1964**, *68*, 3619–3624.

78. Burrill, K. A.; Woods, D. R. *Journal of Colloid and Interface Science* **1973**, *42*, 15–34.

79. Horn, R. G.; Asadullah, M.; Connor, J. N. *Langmuir* **2006**, *22*, 2610–2619.

80. Israelachvili, J. N.; Adams, G. E. *Nature* **1976**, *262*, 774–776.

81. Israelachvili, J. N. *Journal of Colloid and Interface Science* **1986**, *110*, 263–271.

82. Horn, R. G.; Smith, D.; Haller, W. *Chemical Physics Letters* **1989**, *162*, 404–408.

83. Cottin-Bizonne, C.; Jurine, S.; Baudry, J.; Crassous, J.; Restagno, F.; Charlaix, E. *The European physical journal. E, Soft matter* **2002**, *9*, 47–53.

84. Cottin-Bizonne, C.; Cross, B.; Steinberger, A.; Charlaix, E. *Physical Review Letters* **2005**, *94*, 1–4.

85. Zhu, Y.; Granick, S. *Langmuir* **2002**, *18*, 10058–10063.

86. Binnig, G.; Quate, C. F.; Gerber, C. *Physical Review Letters* **1986**, *56*, 930–933.

87. Nanosensors Product Overview. `http://www.nanosensors.com/products\_overview.html`.

88. Avila, A.; Bhushan, B. *Critical Reviews in Solid State and Materials Sciences* **2010**, *35*, 38–51.

89. Meyer, E. *Progress in Surface Science* **1992**, *41*, 3–49.

90. Jones, R. V. *Journal of Scientific Instruments* **1961**, *38*, 37–45.

91. Dufrene, Y. F.; Dufrêne, Y. F. *Nat Rev Micro* **2008**, *6*, 674–680.

92. Butt, H.-J.; Cappella, B.; Kappl, M. *Surface Science Reports* **2005**, *59*, 1–152.

93. Ducker, W. A.; Senden, T. J.; Pashley, R. M. *Nature* **1991**, *353*, 239–241.

94. Butt, H.-J. *Biophysical Journal* **1991**, *60*, 1438–1444.

95. Neto, C.; Craig, V. S. J. *Langmuir* **2001**, *17*, 2097–2099.

96. Israelachvili, J. N. *Intermolecular and Surface Forces*, 2nd ed.; Academic Press London, 1992.

97. Butt, H.-J.; Graf, K.; Kappl, M. *Physics and Chemistry of Interfaces*, 2nd ed.; Wiley-VCH Verlag, 2006.

98. Lyklema, J. *Pure Applied Chemistry* **1991**, *63*, 895–906.

99. Bockris, J. O.; Reddy, A. K. N.; Gamboa-Aldeco, M. *Modern Electrochemistry*, 2nd ed.; Kluwer Academic / Plenum Publishers, 2000; Vol. 2A.

100. Delgado, A. V.; González-Caballero, F.; Hunter, R. J.; Koopal, L. K.; Lyklema, J. *Pure and Applied Chemistry* **2005**, *77*, 1753–1805.

101. Atkins, P. W. *Physical chemistry*, 6th ed.; Oxford University Press, 1998.

102. Bergström, L. *Advances in Colloid and Interface Science* **1997**, *70*, 125–169.

103. Attard, P.; Parker, J. *Physical Review A* **1992**, *46*, 7959–7971.

104. Vinogradova, O. I.; Butt, H.-J.; Yakubov, G. E.; Feuillebois, F. *Review of Scientific Instruments* **2001**, *72*, 2330.

105. Horn, R. G.; Vinogradova, O. I.; Mackay, M. E.; Phan-Thien, N. *The Journal of Chemical Physics* **2000**, *112*, 6424.

106. Wilkening, J. *SIAM Journal on Mathematical Analysis* **2009**, *41*, 588.

107. Brenner, H. *Chemical Engineering Science* **1961**, *16*, 242–251.

108. Vinogradova, O. I. *International Journal of Mineral Processing* **1999**, *56*, 31–60.

109. Alcaraz, J.; Buscemi, L.; Puig-de Morales, M.; Colchero, J.; Baró, A.; Navajas, D. *Langmuir* **2002**, *18*, 716–721.

110. Janovjak, H.; Struckmeier, J.; Müller, D. J. *European Biophysics Journal* **2005**, *34*, 91–96.

111. Jones, R. E.; Hart, D. P. *Tribology International* **2005**, *38*, 355–361.

112. Jana, A.; Raman, A.; Dhayal, B.; Tripp, S. L.; Reifenberger, R. G. *Applied Physics Letters* **2007**, *90*, 114110.

113. Ezkerra, A.; Wilson, P. A.; Mayora, K.; Ruano-López, J. M. *Journal of Micromechanics and Microengineering* **2008**, *18*, 95011.

114. Liu, R.; Roman, M.; Yang, G. *Review of Scientific Instruments* **2010**, *81*, 63703.

115. Zhu, L.; Attard, P.; Neto, C. *Langmuir* **2011**, *27*, 6701–11.

116. Honig, C. D. F.; Ducker, W. A. *Journal of Physical Chemistry C* **2007**, *111*, 16300–16312.

117. Stark, R.; Bonaccurso, E.; Kappl, M.; Butt, H.-J. *Polymer* **2006**, *47*, 7259–7270.

118. Guriyanova, S.; Semin, B.; Rodrigues, T.; Butt, H.-J.; Bonaccurso, E. *Microfluidics and Nanofluidics* **2010**, *8*, 653–663.

119. Honig, C. D. F. Validation of the No Slip Boundary Condition at Solid-Liquid Interfaces. PhD, University of Melbourne, 2008.

120. Easterbrook, P.; Gopalan, R.; Berlin, J.; Matthews, D. *The Lancet* **1991**, *337*, 867–872.

121. Vinogradova, O. I.; Yakubov, G. E. *Langmuir* **2003**, *19*, 1227–1234.

122. Henry, C. L.; Neto, C.; Evans, D. R.; Biggs, S.; Craig, V. S. J. *Physica A: Statistical Mechanics and its Applications* **2004**, *339*, 60–65.

123. Henry, C. L.; Craig, V. S. J. *Physical Chemistry Chemical Physics* **2009**, *11*, 9514–21.

124. Morita, M.; Ohmi, T.; Hasegawa, E.; Kawakami, M.; Suma, K. *Applied Physics Letters* **1989**, *55*, 562.

125. Somasundaran, P., Ed. *Encyclopedia of Surface and Colloid Science*, 2nd ed.; Encyclopedia of Surface and Colloid Science; Taylor & Francis, 2006.

126. van Zwol, P. J.; Palasantzas, G.; van de Schootbrugge, M.; de Hosson, J. T. M.; Craig, V. S. J. *Langmuir* **2008**, *24*, 7528–31.

127. Preuss, M.; Butt, H.-J. *Langmuir* **1998**, *14*, 3164–3174.

128. Butt, H.-J.; Siedle, P.; Fendler, K.; Seeger, T.; Bamberg, E.; Weisenhorn, A. L.; Goldie, K.; Engel, A. *Journal of microscopy* **1993**, *169*, 75–84.

129. Sader, J. E.; Larson, I.; Mulvaney, P.; White, L. R. *Review of Scientific Instruments* **1995**, *66*, 3789–3798.

130. Cleveland, J. P.; Manne, S.; Bocek, D.; Hansma, P. K. *Review of Scientific Instruments* **1993**, *64*, 403–405.

131. Torii, A.; Sasaki, M.; Hane, K.; Okuma, S. *Measurement Science and Technology* **1996**, *7*, 179–184.

132. Holbery, J. D.; Eden, V. L. *Journal of Micromechanics and Microengineering* **2000**, *10*, 85–92.

133. Hutter, J. L.; Bechhoefer, J. *Review of Scientific Instruments* **1993**, *64*, 6748–6748.

134. Feynman, R. P. *Feynman Lectures on Physics*; Addison-Wesley, 1964.

135. Butt, H.-J.; Jaschke, M. *Nanotechnology* **1995**, *6*, 1–7.

136. Walters, D. A.; Cleveland, J. P.; Thomson, N. H.; Hansma, P. K.; Wendman, M. A.; Gurley, G.; Elings, V. *Review of Scientific Instruments* **1996**, *67*, 3583.

137. Cappella, B.; Dietler, G. *Surface Science Reports* **1999**, *34*, 1–104.

138. Klapetek, P.; Nečas, D.; Anderson, C. Gwyddion User Guide. http://gwyddion.net/, `http://gwyddion.net/`.

139. Clark, S. C.; Walz, J. Y.; Ducker, W. A. *Langmuir* **2004**, *20*, 7616–22.

140. Das, S.; Sreeram, P. a.; Raychaudhuri, a. K. *Nanotechnology* **2007**, *18*, 035501.

141. Zhu, L.; Attard, P.; Neto, C. *Langmuir* **2011**, *27*, 6712–9.

142. Francis, B. A.; Horn, R. G. *Journal of Applied Physics* **2001**, *89*, 4167.

143. National Instruments Tutorial 10342: Do I Need a Real-Time System? 2010; `http://zone.ni.com/devzone/cda/tut/p/id/10342`.

144. Semin, B.; Guriyanova, S.; Bonaccurso, E. *Review of Scientific Instruments* **2006**, *77*, 116107.

145. Guriyanova, S.; Bonaccurso, E. *Physical chemistry chemical physics : PCCP* **2008**, *10*, 4871–8.

146. Happel, J.; Brenner, H. *Low Reynolds Number Hydrodynamics: with Special Applications to Particulate Media*; Mechanics of fluids and transport processes; Kluwer Academic, 1991.

147. Bonaccurso, E.; Schönfeld, F.; Butt, H.-J. *Physical Review B (Condensed Matter and Materials Physics)* **2006**, *74*, 085413.

148. Albrecht, T. R.; Akamine, S.; Carver, T. E.; Quate, C. F. *Journal of Vacuum* **1990**, *8*, 3386–3396.

149. Sader, J. E. *Review of Scientific Instruments* **2003**, *74*, 2438.

150. Sader, J. E.; Sader, R. C. *Review of Scientific Instruments* **2003**, *83*, 3195–3197.

151. Kunert, C.; Harting, J.; Vinogradova, O. I. *Physical Review Letters* **2010**, *105*, 2–5.

152. Asmolov, E. S.; Belyaev, A. V.; Vinogradova, O. I. *Physical Review E* **2011**, *84*, 1–8.

153. Yordanov, S. Total Internal Reflection Fluorescence Cross-Correlation Spectroscopy : Theory and Application for Studying Boundary Slip Phenomenon. Ph.D. thesis, Johannes Gutenberg University Mainz, 2011.

154. Maali, A.; Wang, Y.; Bhushan, B. *Langmuir* **2009**, *25*, 12002–12005.

155. Huang, D. M.; Sendner, C.; Horinek, D.; Netz, R. R.; Bocquet, L. *Physical Review Letters* **2008**, *101*, 1–4.

156. Maali, A.; Bhushan, B. *Journal of Physics: Condensed Matter* **2008**, *20*, 315201.

157. Schrader, M. E. *The Journal of Physical Chemistry* **1980**, *84*, 2774–2779.

158. Tadros, M. E.; Hu, P.; Adamson, A. W. *Journal of Colloid and Interface Science* **1974**, *49*, 184–195.

159. Fowkes, F. M.; Harkins, W. D. *Journal of the American Chemical Society* **1940**, *62*, 3377–3386.

160. Morcos, I. *Journal of Colloid and Interface Science* **1970**, *34*, 469–471.

161. Wang, S.; Zhang, Y.; Abidi, N.; Cabrales, L. *Langmuir* **2009**, *25*, 11078–81.

162. Zhou, Y.; Pasquarelli, R.; Holme, T.; Berry, J.; Ginley, D.; O'Hayre, R. *Journal of Materials Chemistry* **2009**, *19*, 7830.

163. Wang, R.; Sakai, N.; Fujishima, A.; Watanabe, T.; Hashimoto, K. *The Journal of Physical Chemistry B* **1999**, *103*, 2188–2194.

164. Shin, Y. J.; Wang, Y.; Huang, H.; Kalon, G.; Wee, A. T. S.; Shen, Z.; Bhatia, C. S.; Yang, H. *Langmuir* **2010**, *26*, 3798–802.

165. Rafiee, J.; Rafiee, M. a.; Yu, Z.-Z.; Koratkar, N. *Advanced Materials* **2010**, *22*, 2151–2154.

166. Miao, X.; Gao, A.; Hiroto, S.; Shinokubo, H.; Osuka, A.; Xin, H.; Deng, W. *Surface and Interface Analysis* **2009**, *41*, 225–230.

167. Döppenschmidt, A.; Butt, H.-J. *Colloids and Surfaces A: Physicochemical and Engineering Aspects* **1999**, *149*, 145–150.

168. Zach, M. P.; Newberg, J. T.; Sierra, L.; Hemminger, J. C.; Penner, R. M. *The Journal of Physical Chemistry B* **2003**, *107*, 5393–5397.

169. Yang, S.; Kooij, E. S.; Poelsema, B.; Lohse, D.; Zandvliet, H. J. W. *EPL (Europhysics Letters)* **2008**, *81*, 64006.

170. Hampton, M. a.; Nguyen, A. V. *Minerals Engineering* **2009**, *22*, 786–792.

171. Raviv, U.; Laurat, P.; Klein, J. *The Journal of Chemical Physics* **2002**, *116*, 5167.

172. Berger, R.; Butt, H.-J.; Retschke, M. B.; Weber, S. A. L. *Macromolecular Rapid Communications* **2009**, *30*, 1167–1178.

173. Sommerhalter, C.; Matthes, T. W.; Glatzel, T.; Jäger-Waldau, A.; Lux-Steiner, M. C. *Applied Physics Letters* **1999**, *75*, 286.

174. Donose, B. C.; Vakarelski, I. U.; Higashitani, K. *Langmuir* **2005**, *21*, 1834–9.

175. Bonaccurso, E. Investigation of Electrokinetic Forces on Single Particles. PhD, Univesität-Gesamthochschule-Siegen, 2001.

176. Cole, D. G.; Clark, R. L. *Journal of Applied Physics* **2007**, *101*, 34303.

177. Fenollosa, R.; Meseguer, F.; Tymczenko, M. *Advanced Materials* **2008**, *20*, 95–98.

178. Kunz, W. *Pure and Applied Chemistry* **2006**, *78*, 1611–1617.

179. Benmouna, F.; Johannsmann, D. *Journal of Physics: Condensed Matter* **2003**, *15*, 3003–3012.

180. Maali, A.; Cohen-Bouhacina, T.; Couturier, G.; Aimé, J.-P. *Physical Review Letters* **2006**, *96*, 2–5.

181. Li, X.-M.; Reinhoudt, D.; Crego-Calama, M. *Chemical Society reviews* **2007**, *36*, 1350–68.

182. Proksch, R.; Schäffer, T. E.; Cleveland, J. P.; Callahan, R. C.; Viani, M. B. *Nanotechnology* **2004**, *15*, 1344–1350.

183. Chung, K.-H.; Shaw, G. A.; Pratt, J. R. *Review of Scientific Instruments* **2009**, *80*, 065107.

184. McBride, S. P.; Law, B. M. *Review of Scientific Instruments* **2010**, *81*, 113703.

Symbols and Acronyms

A_H . . . . . .Hamaker constant
E . . . . . .Young's modulus
F_{clv} . . . . . .drag force on the cantilever
I . . . . . .moment of inertia
L . . . . . .length of a cantilever
P . . . . . .positional noise power
R . . . . . .radius of a sphere
T . . . . . .temperature
Z_{PV} . . . . . .peak-to-valley roughness
Z_{RMS} . . . . . .root mean square roughness
α . . . . . .angle between the cantilever and the surface
η . . . . . .liquid viscosity
b . . . . . .slip length
h . . . . . .distance sphere-edge–substrate
$h_{0,ret}$ . . . . . .initial separation (retract)
k . . . . . .spring constant of a cantilever
k_B . . . . . .Boltzmann constant
k_{bare} . . . . . .spring constant of a cantilever without any attachment
k_{sph} . . . . . .spring constant of a cantilever with an attached sphere
t_c . . . . . .thickness of a cantilever
v_p . . . . . .piezo speed
w . . . . . .width of a cantilever
KCl . . . . . .potassium chloride
SiO_2 . . . . . .silicon dioxide

AFM . . . . . .atomic force microscope

BC . . . . . .boundary condition

CCR . . . . . .constant-compliance region
CPT . . . . . .colloidal probe technique

DLVO . . . . . .Derjaguin and Landau, Vervwey and Overbeek theory

EDL . . . . . .electrical double layer

F-D curve . . . . .force versus distance curve

HOPG . . . . . .highly ordered pyrolytic graphite

InvOLS . . . . . .inverse optical lever sensitivity

OPS . . . . . .optical position sensor

PSD . . . . . .power spectral density
PZT . . . . . .piezoelectric transducer

RMS . . . . . .root mean square

SFA . . . . . .surface force apparatus

ZFR . . . . . .zero-force region

Acknowledgments

[removed for privacy reasons]

Many thanks to those who financially supported this work: the European Union (Marie Curie Host Fellowship, EST-ADMIST), the Max Planck Society and IMPRS.